The Dissertation Committee for Furun Wang Certifies that this is the approved version of the following dissertation:

Study on Center of Mass Calibration and K-band Ranging System Calibration of the GRACE Mission

Committee:

Byron D. Tapley, Supervisor

Wallace T. Fowler

Bob E. Schutz

Srinivas V. Bettadpur

Michael M. Watkins

Study on Center of Mass Calibration and K-band Ranging System Calibration of the GRACE Mission

by

Furun Wang, B.S., M.S.

Dissertation

Presented to the Faculty of the Graduate School of

The University of Texas at Austin

in Partial Fulfillment

of the Requirements

for the Degree of

DOCTOR OF PHILOSOPHY

The University of Texas at Austin

December, 2003

This dissertation is dedicated to my parents,

Yaoshan Wang and Fang Lu

who have given me love and support

through my life

Acknowledgements

It is with great pleasure that I acknowledge the efforts of the many people who have contributed to my research. First and foremost, I would like to thank my advisor Prof. Byron Tapley for all of his kindness, enthusiasm, patience, and valuable input in helping me to finish this dissertation. Special thanks to my research supervisor Dr. Srinivas Bettadpur who has guided my research in an excellent way and given me so much help. They have stood by me offering encouragement and helped out in ways no other could do. I also wish to thank people in the Jet Propulsion Laboratory, Ab Davis, Gerard Kruizinga, Joseph Beerer, Larry Romans, Mike Watkins, Sien Wu, who made great efforts to this research topic. My heartfelt gratitude also goes to Bob Schutz, Craig Dupree, Hyung Rim, Ileene Pickett, Jianli Chen, John Ries, John Schutz, Karen Burns, Minkang Cheng, Nikki Goodfellow, Nita Pollard, Peter Nagel, Rick Pastor, Shauna Pendleton, Steve Williams, Sungkoo Bae, Wallace Fowler, Zhigui Kang, who gave me valuable information for the research and supported lots of things. Also, thanks to all CSR staff who make such a wonderful working place.

Last but not least, I want to thank my wife Yanqing Liu and my daughter Guanglu (Emily) Wang for their love and support and happiness to me.

<div style="text-align: right">Furun Wang</div>

The University of Texas at Austin
December, 2003

Study on Center of Mass Calibration and K-band Ranging System Calibration of the GRACE Mission

Publication No._____

Furun Wang, Ph.D.

The University of Texas at Austin, 2003

Supervisor: Byron D. Tapley

The twin Gravity Recovery and Climate Experiment (GRACE) satellites were successfully launched on March 17, 2002. The mission goal is to make significant improvement in current measurements of the Earth's gravity field. The satellites are linked by a K-band ranging system, which measures the range change due to the gravitational and non-gravitational accelerations. The non-gravitational accelerations can be obtained by transforming the accelerometer measurements into the inertial frame of reference based on the star camera observations, and will be used to separate gravitational effects in the range changes. However, the accelerometer's proof mass offset from the center of mass of the spacecraft must be minimized and the misalignment between star camera frame and accelerometer frame must be known accurately in order to reduce the accelerometer data error. In addition, the phase center of the K-

band horn must be known to make antenna offset corrections to the range and range change data.

The objective of the center of mass calibration is to determine the proof mass offset, and then, to use the center of mass trim assembly mechanism to eliminate this offset. The main purpose of the K-band ranging system calibration is to determine the phase center of the K-band antenna, which will be used to adjust the satellite attitude orientations and make the antenna offset corrections to the K-band ranging system phase measurements. Furthermore, this calibration allows the misalignment between star camera frame and accelerometer frame to be determined.

The calibration maneuvers have been designed for the real mission. Estimation algorithms have been developed and complete simulations have been performed. Finally, the real calibration data have been processed. Analysis shows that the proof mass offset has been determined better than the requirement value of 0.1 mm and trimmed well below this value. The boresight error of the K-band horn's phase center has been determined better than 0.3 mrad and the resultant antenna offset correction error of range and range rate will be much less than the system resolution $(10\mu m, 1\mu m/s)$ and the frame misalignment parameters have been determined better than $(0.04°, 1\sigma)$. Overall, the goal of calibrations has been successfully achieved.

Table of Contents

List of Tables

List of Figures

Chapter 1: Introduction

1.1 BACKGROUND

Efforts to determine the Earth's gravity field and improve the accuracy via spacecraft have been made for several decades since the launch of Sputnik 1 in 1957 (Vetter, et al., 1993). Tracking data from the orbits of a single satellite and high-low satellite-to-satellite tracking with Global Positioning System (GPS) have already provided valuable knowledge of the Earth's gravity field. However, due to the attenuation of the gravity signal with height above the surface of the Earth, these conventional methods do not provide enough information on the short wavelength gravity signals and the improvement is limited to the long and medium wavelength signals (Kim, 2000, Committee on Earth Gravity from Space, 1997). To obtain a significant improvement in the short wavelength accuracy as well as the long wavelength accuracy, the Gravity Recovery And Climate Experiment (GRACE) mission using a low-low satellite-to-satellite tracking concept was proposed in 1997 (Tapley, et al., 1997).

In the same year, the GRACE mission was selected as one of the first two missions to be implemented under the NASA (National Aeronautics and Space Administration) Earth System Science Pathfinder (ESSP) Program. A component of NASA's Earth Science Enterprise (ESE), ESSP missions are intended to address unique, specific, highly focused scientific issues and provide measurements required to support Earth science research. The ESSP missions are an integral part of a dynamic and versatile program consisting of multiple Earth

system science satellites. The ESSP program is characterized by relatively low to moderate cost, small- to medium-sized missions that are capable of being built, tested and launched in short-time intervals. These missions are capable of supporting a variety of scientific objectives related to Earth science, including studies of the atmosphere, oceans, land surface, polar ice regions and solid Earth (NASA Facts, 2002).

GRACE is a joint project between the US National Aeronautics and Space Administration and the Deutsches Zentrum Fur Luft und Raumfahrt (DLR) (GRACE Meeting, 1999). The NASA Jet Propulsion Laboratory (JPL) leads the development of the science instrument and satellite system in partnership with Space System/Loral (SS/L) and Dornier Satellitensysteme (DSS). The German Space Operation Center (GSOC) performs telemetry and telecommand activities at the Mission Control Center in Oberpfaffenhofen, Germany. The observation data collected by GSOC are analyzed, processed and distributed cooperatively to JPL, University of Texas at Austin, Center for Space Research (UTCSR), and GeoForschungsZentrum (GFZ) in Germany (GRACE Meeting, 1999, Kim, 2000).

The GRACE mission is intended to make at least a 100-fold improvement in current measurements of the Earth's gravity field. This highly detailed map of Earth's gravitational field will relate minute fluctuations of gravity to the planet's physical features. A new map of Earth's gravity, which changes in time as well as by location, will be generated for every month during the mission's expected five-year lifetime (GRACE Mission Briefing, 2002). The gravity variations that GRACE will study include: changes due to surface and deep currents in the

ocean; runoff and ground water storage on land masses; exchanges between ice sheets or glaciers and the oceans; and variations of mass within the Earth. The GRACE mission will provide critical inputs to many scientific models used in oceanography, hydrology, geology and related disciplines. The improvement in the knowledge of the Earth's gravity will allow scientists to better trace the transport of water and heat between the oceans, atmosphere and land, information vital to the study of global climate change (GRACE Mission Briefing, 2002). Another goal of the mission is to create a better profile of the Earth's atmosphere. The accurate determination of the Earth's gravity field provided by GRACE mission will dramatically improve the above Earth science fields. It is expected that the results from GRACE mission will make a huge contribution to the goals of NASA's Earth Science Enterprise, Earth Observation System (EOS) and global climate change studies.

A significant mission configuration change from the previous Earth gravity field determination missions is that the GRACE mission utilizes two identical satellites flying in coplanar orbits and linked by a K-band ranging system. As the gravitational field changes beneath the satellites, the orbital motion of each satellite is changed. This change in orbital motion causes the distance between the satellites to change infinitesimally and the K-band measurement system can detect these changes, with a resolution better than 10 micrometers. Two different frequency signals of 24 GHz (K band) and 32 GHz (Ka band) are transmitted and received between the satellites. The received signals are sent to

ground stations and then combined to yield ionosphere-free range observations for recovery of the Earth's gravity field.

The orbits of both satellites are dependent on not only the globally integrated effect of the mass distributions and movements in the Earth system, but also on the non-gravitational accelerations, such as atmosphere drag and radiation pressure. The non-gravitational accelerations must be measured accurately in order to separate gravitational effects from non-gravitational effects in the range changes. For this purpose, a SuperSTAR accelerometer is mounted at the center of mass of each satellite.

The GPS signals for navigation and occultation applications are received using four antennas and the JPL Turbo-Rogue Space Receiver (TRSR-2). The main zenith patch antenna is used to collect the navigation data. In addition, a backup patch antenna and two helix bowl antennas on the aft side are used for back-up navigation and atmospheric occultation data collection, respectively. This system is capable of simultaneously tracking up to 12 GPS satellites at both L1 and L2 frequencies (GRACE Meeting, 1999).

The orientation of each GRACE satellite is sensed using two star cameras, rigidly attached to the accelerometer and viewing the sky, on the port and starboard sides, at 55 degrees angle with respect to the zenith.

The Laser corner reflector assembly is mounted on the underside of the spacecraft to permit the orbit verification activities from terrestrial laser tracking networks (GRACE Meeting, 1999).

The satellites fly in a three-axis stabilized Earth pointing mode, with the attitude being controlled by a cold gas propulsion system and magnetic torquers. In addition, each satellite has magnetometer on board to probe the Earth magnetic field vector.

Launched on March 17, 2002, the two GRACE spacecraft will orbit in coplanar orbits between 300 and 500 km above the surface at an inclination between 89 and 90 degrees. They are separated along track by 100 and 500 km. The separation distance varies over the 5-year lifetime of the mission. Orbit maneuvers are required every 30-60 days in order to maintain the separation between the satellites in addition to occasional center of mass calibration and K-band ranging system calibration and altitude "make-up" maneuvers (NASA Facts, 2002).

The GRACE satellites themselves become the experiment, allowing a precise 'snapshot' of the Earth's gravity field to be measured.

1.2 RESEARCH MOTIVATION

The SuperSTAR accelerometer is one of the most important instruments on board each GRACE satellite and serves to measure all non-gravitational accelerations. These accelerations are due to the forces of air drag, solar radiation pressure, Earth radiation pressure, and attitude control activator operation. In combination with the position measurements of the GPS receiver assembly, purely gravitational orbit perturbations can be derived for use in gravity field modeling. A by-product of the accelerometer measurements is the determination of upper atmospheric densities (Grunwaldt, et al., 1996).

The accelerometer uses the basic principle of all electrostatic micro-accelerometers: a proof mass is free floating inside a cage supported by an electrostatic suspension. The cavity walls are equipped with electrodes thus controlling the motion (both translational and rotation) of the proof mass by electrostatic forces. Electric signals proportional to the accelerations acting on the proof mass are picked up by these electrodes and fed to the experiment electronics. By applying a closed loop feedback inside the sensor unit, the proof mass is kept motionless in the center of the cage. Knowing the mass of the proof mass, the acceleration vector can be derived (Grunwaldt, et al., 1996). The acceleration detected during the spaceflight is a measure of the non-gravitational forces acting on the satellite body.

However, the proof mass of the accelerometer must be positioned precisely at the Center Of Mass (COM) of the GRACE satellite. Otherwise, it measures not only non-gravitational accelerations, but also disturbance accelerations, such as angular motion related acceleration and acceleration due to gravity gradient. Unfortunately, before satellite launching, the satellite's COM cannot be perfectly balanced to the position of the proof mass of the accelerometer. Even so, it still keeps moving during the in flight phase mainly due to cold gas consumption. Based on the satellite distortion analysis (Riede, et al., 1999), the pre-launch error of GRACE's COM resulting from various sources is shown in Table 1.1, and the in-flight stability of GRACE's COM is shown in Table 1.2.

Table 1.1   Ground Error of GRACE's COM

Effect	Ground Error		
	Roll	Pitch	Yaw in mm
COM measurement uncertainties	0.2	0.2	0.2
Remaining unbalanced	0.067	0.042	0.021
Accuracy of Tank Mounting	0.076	0.076	0.076
Difference in Tank volume	0.01	---	---
1g/0g effects-gravity	0.105	0.042	0.049
1g/0g effect-temperature	0.083	0.004	0.027
Moisture release CFRP / shrink	0.053	0.021	0.011
Moisture release CFRP / mass decrease	---	---	0.038
Moisture release foam / mass decrease	---	---	0.078
Shrink due to moisture release of foam	---	---	0.008
Uncertainty of boom position	0.007	---	---
Impact of buoyancy	0.053	0.053	0.053
RMS-Value of Error	0.27	0.23	0.24
Requirement	0.5	0.5	0.5

Table 1.2   In-Flight Stability of GRACE's COM

Effect	In-Flight Stability		
	Roll	Pitch	Yaw in mm
Impact of cold gas piping	0.0003	0.0001	0
Gas consumption	0.0462	---	---
Total mass decrease	0.0007	0.0007	0.0007
RMS-Value of Error	0.0462	0.0007	0.0007
Requirement (mm/0.5yrs)	± 0.1	± 0.1	± 0.1

Note: --- means irrelevant.

Later, the vector pointing to the proof mass from the COM is called the proof mass offset, which is sometimes referred to as Center of Gravity (CG) offset, because the difference between the CG and COM of GRACE satellite during the nominal phase is very small compared to the offset requirement of 0.1 mm (Wang, 2000a, Rimrott, 1989). In reality, the proof mass offset always exits. From the above two tables, it can be seen that the proof mass offset may be as large as 0.5 mm along each axis due to ground positioning error and with a change of as much as 0.1 mm each half year during the flight phase. It is expected the offset can be less than 2 mm along each axis under the worst conditions which occur just after the launch of the satellites. However, this value is much larger than the proof mass offset requirement, which is less than 0.1 mm along each axis and is the safe boundary for using the accelerometer measurements to map the Earth's gravity field. In order to meet this requirement for proof mass offset, a center of mass calibration (COM Calibration) will be executed on each satellite to determine this offset during the commissioning phase of the satellites. This calibration is intended to determine the proof mass offset with an accuracy of better than 0.1 mm along each axis. Then the center of Mass Trim assembly Mechanism (MTM) on board each GRACE satellite is used to move mass elements inside the satellite so that the center of mass of satellite is positioned at the proof mass of the accelerometer within the tolerance of requirement (GRACE Team, 1998a). From the flight stability of GRACE's COM analysis, it is expected that COM calibration will be required roughly every 6 months. The specific calibration timeline is subject to change for the real mission.

8

An approach for GRACE proof mass offset determination with the MagneTorQuer (MTQ) has been proposed in pre-mission investigations (Romans, 1997, GRACE Team, 1999c). The principle of this approach is to disturb the satellite's attitude with a slight oscillation driven by a periodic magnetic torque at some fixed frequency for a specified time interval. From the accelerometer measurements during the calibration time span, it is expected to separate the periodic accelerations induced by proof mass offset from the relatively flat non-gravitational accelerations, thus allowing the proof mass offset to be determined. Starting with this conceptual calibration approach, a careful design of the calibration maneuver, including optimal choice of the maneuver parameters, specification of the optimal timing, development of the estimation algorithms, demonstration of the concept by complete simulations and processing the real mission data are topics covered in the scope of this research.

Besides the accelerometer, another important instrument on board the GRACE satellite is the dual one-way K-Band Ranging system (KBR), which is designed for precise inter-satellite phase measurements. This system combines the phase measurements from each of the two satellites to obtain a very accurate measurement of distance between the COMs of the twin satellites. The post-processing of the KBR measurements yields a biased value of the low-low range, which is the most important observable of the GRACE mission. A block diagram of the microwave ranging system and the GPS receivers is shown in Figure 1.1 (Thomas, 1999).
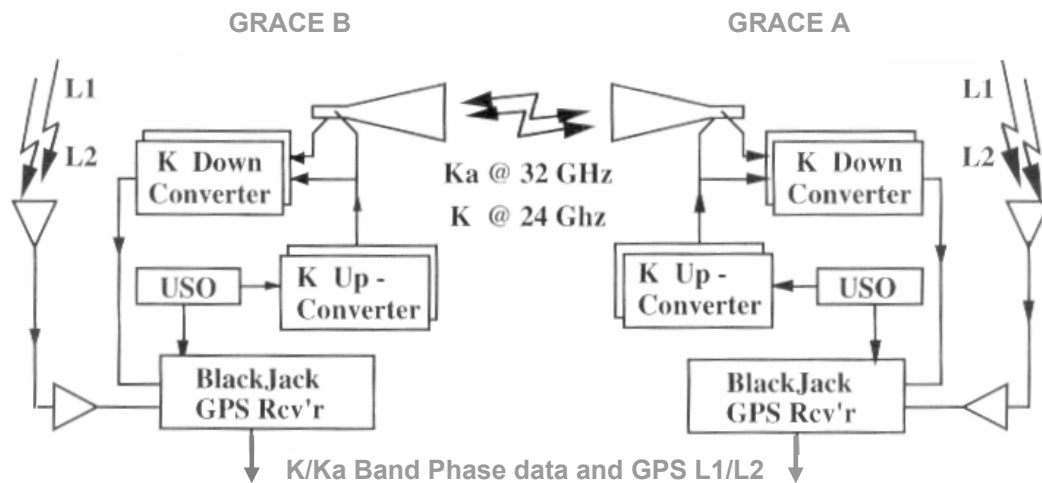
Figure 1.1   Integrated Microwave Link and GPS Receivers

The low-low range observable derived from KBR phase measurements, indeed, is a measure of biased distance between the phase centers of two K-band horns. The bias is an integer ambiguity when first starting the K-band ranging system and changes with possible cycle slips, which corresponds to the integer ambiguity of the GPS receiver's observation. However, the low-low range observable is used to describe the distance between COMs of twin satellites in the Earth's gravity field mapping. The satellite attitudes are set so that phase centers of K-band horns and COMs of two satellites are in the same straight line in the ideal situation. Before the launch of the GRACE satellites, the phase center of the K-band horn on each satellite is pre-determined. However, during the in flight phase, the K-band ranging system calibration (KBR Calibration) is required to determine the phase centers of both horns in case the phase centers change in the space environment. The phase centers may remain unchanged compared to the pre-launching positions or they may be changed due to the different environment.

10

In any event, the calibration information is indeed used for attitude control such that the phase centers of two K-band horns and COMs of two GRACE satellites are nearly along a straight line, that is also used for the alignment corrections (also referred as antenna offset corrections) during the post-processing of the KBR phase measurements. Therefore, the low-low range observable could precisely reflect the relative COMs' movements of the GRACE satellites as well as a bias.

In a manner similar to the COM calibration, a KBR calibration approach was proposed in 1998 (Romans, 1998). The scheme of this proposal is to periodically rotate one GRACE satellite through a certain range of angles along a certain sweeping plane to determine the phase center of the antenna on the rotating satellite. Based on this proposal, two calibration approaches, calibration using a periodic oscillation maneuver and calibration using a linearly drifting maneuver, are proposed and investigated in this research. The calibration maneuver of each calibration approach is carefully designed, and its corresponding estimation algorithms are developed. Complete simulations of each approach show that the phase center of each satellite's horn can be determined such that the direction pointing to phase center from COM, referred as the boresight direction, can be determined to better than 3 mrad under the worst conditions. If the largest error sources can be removed, the boresight can be determined to be better than 0.3 mrad.

Before more information about KBR calibration are presented, it is appropriate that some knowledge about phase center determination in electrical

engineering be introduced. The KBR calibration design in this research is nothing but a three dimensional and more complicated version of the following introduction.

1.3 PHASE CENTER OF ANTENNA

In a (R,θ,ϕ) antenna coordinate, shown in Figure 1.2 (Balanis, 1997), with the origin being the geometric center of the antenna and θ being the polar angle and ϕ being the azimuth angle starting from the main beam, a specified component of the far field energy radiated by an antenna can be written (IEEE, 1979), in general, as

$$E_u(R,\theta,\phi) = \hat{u}E(\theta,\phi)e^{j\psi(\theta,\phi)}\frac{e^{-jkR}}{R} \qquad (1.1)$$

where $E(\theta,\phi)$ and $\psi(\theta,\phi)$ represent the (θ,ϕ) dependence of the magnitude and phase, respectively, of the specified component, and (R,θ,ϕ) are spherical coordinates of the observation point. The vector $\hat{u}$ is a vector of magnitude unity, which indicates the polarization of the specified component. k is the phase constant obtained by 2π divided by signal wavelength λ, and j is the conventional complex number $\sqrt{-1}$ (Milligan, 1985, Lee, 1984).
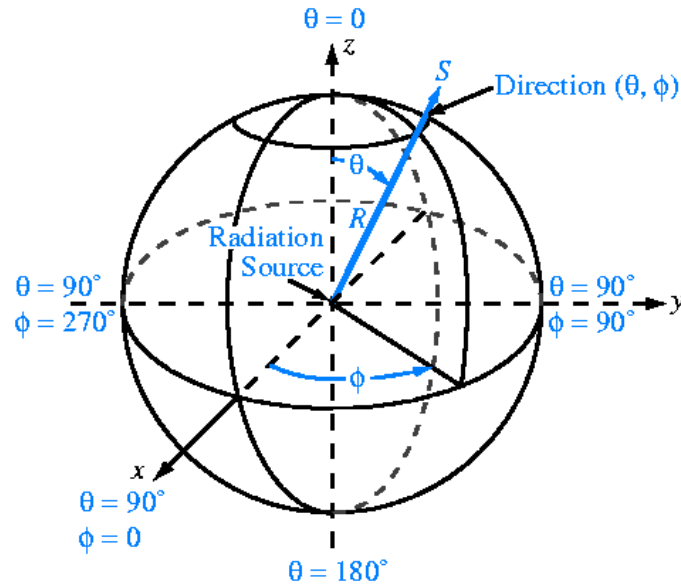
Figure 1.2   Antenna Spherical Coordinate System

In navigation, tracking, homing, landing, and other aircraft and aerospace systems, it is usually desirable to assign to the antenna a reference point such that for a given frequency, $\psi(\theta,\phi)$ is independent of θ and ϕ (i.e., $\psi(\theta,\phi) = $ constant). The reference point that makes $\psi(\theta,\phi)$ independent of θ and ϕ is known as the phase center of the antenna. When referenced as the phase center, the fields radiated by the antenna are spherical waves with ideal spherical wavefronts or equiphase surfaces (Balanis, 1997).

For most antennas such as arrays, reflectors, horns, a "true" phase center valid for all directions does not exist. However, in many antenna systems a reference point can be found such that $\psi(\theta,\phi)$ becomes constant over a range of directions of interest, for instance, over the portion of the main beam of the antenna.

13

The analytical formulations for locating the phase center of an antenna are usually very laborious and exist only for a limited number of configurations. Usually, experimental techniques are used to locate the phase center of an antenna. The arrangement of Figure 1.3 can be used to measure the phase center of antenna under test experimentally (IEEE, 1979, Evans, 1990). In the experiment, the antenna under test is rotated through a certain range of angles and the phase pattern is recorded. From the phase measurements and rotation angles, the phase center of antenna under test can be determined.
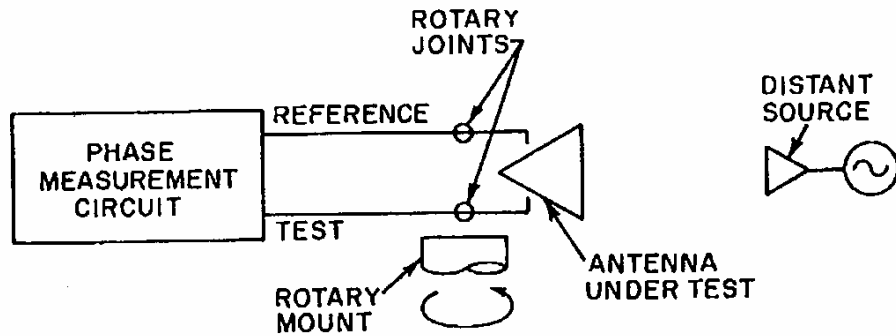
Figure 1.3   Phase Center Measurement Setup

Let us assume that the antenna under test has a phase center on the axis of the structure and that the antenna is positioned in the (R, θ, ϕ) coordinate system with $\theta = 0°$ as the antenna axis. If a phase pattern is recorded for this antenna about some origin, or center of rotation, which coincides with the phase center, this pattern over the main beam will, by definition, be a constant. If a phase pattern is recorded as this antenna is rotated about some origin along the axis of the structure, but displaced a distance r' from the phase center, the phase of the

field of the antenna will be modified by a cosinusoidal function of θ. When r' is very small compared to the distance to the point of observation, the resultant phase pattern will be given by

$$\psi \approx kr'(1 - \cos\theta) \tag{1.2}$$

In theory, the position of the phase center can be calculated from one such phase pattern. If a change in phase ψ is measured as the antenna is rotated from $\theta = 0°$ to $\theta = \theta_1$, the phase center is displaced from the center of rotation by the distance

$$r' = \frac{\lambda}{2\pi}\left(\frac{\psi}{1 - \cos\theta_1}\right) \tag{1.3}$$

In practice, it may be necessary to record several patterns to determine the phase center offset r'.

In a more complicated and general case, the phase center is displaced from the axis of the antenna by d besides the offset r' along the rotation axis, the phase change with the rotation will be

$$\psi \approx k\sqrt{r'^2 + d^2}\,(1 - \cos(\theta + \tan^{-1}(\frac{d}{r'}))) \tag{1.4}$$

Given adequate phase observations and corresponding rotation angles, the phase center offset r' and d can be determined. In fact, the principle used in the GRACE KBR calibration design is exactly the same as the above two examples. What is different is that for the GRACE KBR calibration both phase centers of antennas need to be determined, and the relative range between the antennas is

15

changed due to different orbit perturbations. The former problem can be solved using multiple maneuvers, and the later one can be tackled by precise orbit determination of both satellites.

As pointed out before, the phase center of an antenna is angular variation and it is frequency dependent. The phase center of antenna on board GRACE satellite is fixed along the nominal flight direction within $3°$ angular variation. Also, the GRACE antenna team has calibrated the phase center fixed with respect to different rotation directions, which implies that if the satellite is rotated about the yaw axis and pitch axis, the phase center of antenna is the same. This is critically important because the calibration maneuver designed in this research involves sub-maneuvers with different sweep planes. Furthermore, the phase center of each K-band horn is different with respect to K band and Ka band signals. In the post-processing of the KBR phase measurements, these different frequency signals are combined to eliminate the ionosphere effects. Therefore, the phase center of the GRACE K-band horn is a combination of two phase centers with respect to the K and Ka band frequencies.

1.4 OUTLINE OF RESEARCH

The background and motivation discussed in the previous sections set out this research work. The objective of this research is to thoroughly study the center of mass calibration and K-band ranging system calibration for GRACE mission. In this study, the maneuvers and parameters for these two calibrations will be carefully designed. The corresponding algorithms to process data will be developed. Complete simulations will be performed, which provide some crucial

information for the real calibrations. Finally, real data will be processed using the algorithms proposed in this research.

Chapter 2 describes the spacecraft orbit and attitude dynamics. In Chapter 3, the maneuver design and necessary observation data set for the COM calibration and KBR calibration are discussed. In addition, the way in which active torques are employed for these calibrations is fully investigated. Furthermore, the performance characteristics of the measurement instruments involved in these two calibrations are presented and their measurement models are established, from which the simulation data are generated.

Chapter 4 is an important part of this research. It derives and develops the estimation algorithms for COM calibration and KBR calibration in detail. In addition, the covariance analysis for center of mass calibration is performed, from which the optimal calibration location criterion is found. This criterion provides a theoretical guideline for realizing the real calibration maneuver. The noise analysis for K-band ranging system calibration is also carried out. Based on the estimated phase centers and the attitude observations, the alignment correction of the KBR range observable is derived. Moreover, an approach to determine the star camera's misalignment is proposed.

In Chapter 5, complete simulations for COM calibration, KBR calibration and star camera's misalignment determination are performed. The simulations verified the assumptions used in developing the estimation algorithms, tested the estimation algorithms, provided the bases for selection of the maneuver

parameters, determined the optimal timing of the calibrations and confirmed that the calibration accuracy can satisfy the system requirement.

In Chapter 6, the real data processing is presented. It is always a challenge to process the real data. Along with the determination of the proof mass offset and K-band horn phase center on each GRACE satellite, the misalignment of the star camera with respect to the satellite body fixed frame is also calculated. Estimation algorithms used in simulations are applied to process real calibration data. It has been found that the real calibration data behaves consistently with the simulation data, which indicates that the determination accuracy for the real mission can be achieved to the simulation lever.

The summary and conclusions from this research are discussed in Chapter 7, and also some recommendations for future work are presented.

Finally, three appendices are presented. Appendix A is to specify the CRN digital filter, and Appendix B is to outline some properties of quaternion operations. These two appendices contain some important information used frequently in this research. Furthermore, the final appendix summarizes the operators which appear in this research.

Chapter 2: Spacecraft Dynamics

2.1 INTRODUCTION

In reality, orbit dynamics and attitude dynamics of near Earth spacecraft are mutually coupled. Different orbits lead to different environmental torques, such as aerodynamic torque and radiation torque, and different attitude orientations result in different orbit perturbations. Thus orbit dynamics affects attitude dynamics, and vice versa.

Both orbit dynamics and attitude dynamics are involved in the GRACE center of mass and K-band ranging system calibration. In the simulation, data generation requires an accurate description of these dynamics interactions. For example, the accelerometer measures orbit-related non-gravitational accelerations, and the star cameras measures attitude data. Since the attitude of the GRACE satellite may deviate from the nominal flight orientation and the attitude information may play an important role in both calibrations, the traditional simulation method of integrating the orbit dynamics with a nominal spacecraft orientation may be not adequate. Therefore, the mutually coupled orbit and attitude dynamics are integrated together in the data simulation. When the calibration data are processed, both orbit and attitude information are required in most of estimation algorithms proposed in the following chapters. However, in this phase, the orbit dynamics and attitude dynamics can be integrated separately because the star camera observations can be used directly in the equations of the orbit dynamics, and the dominant torques are available for those of the attitude.

Many formulations of orbit dynamics and attitude dynamics exist. The orbit dynamics models used in this research are extracted from MSODP (Multi-Satellite Orbit Determination Program), a sophisticated orbit determination software developed at UTCSR. In addition, an elegant program developed specially for GRACE satellites at AMA/LaRC (Analytic Mechanics Associates/ Langley Research Center) (Bettadpur, 1999) can compute the torques due to atmosphere and solar radiation. This program is used to model the environmental torques in the attitude dynamics propagation.

As usual, the spacecraft orbit and attitude equations of motion are written with respect to the COM of spacecraft.

2.2 COORDINATE SYSTEM

The reference system $O_I - XYZ$ adopted in this research for the dynamics model is the J2000 geocentric inertial coordinate system, which is defined by the mean equator and vernal equinox at Julian epoch 2000.0. The Earth's body-fixed coordinate system $O_E - x'y'z'$ is defined by a simple rotation with respect to the $O_I - XYZ$ reference system, which implies that the effects of Earth's precession, nutation, polar motion and the true sideal time correction, small enough indeed for a short time interval, are ignored in this research. The rotation angle of these two frames, denoted by α_G, is the right ascension of Greenwich meridian. The spacecraft body-fixed coordinate systems $O_b - x_1 y_1 z_1$, $O_b - x_2 y_2 z_2$ are defined with origins at the center of mass of the spacecraft. The axes directions of these systems are defined as: for GRACE A, $-\hat{x}_1$ is along track by pitching up $\sim 1^o$, $\hat{y}_1$ is normal to the x_1-z_1 plane, and $\hat{z}_1$ is radial downward; for GRACE B, $\hat{x}_2$ is

20

along track by pitching down $\sim 1^o$, $\hat{y}_2$ is normal to the x_2-z_2 plane, and $\hat{z}_2$ is radial downward. The roll axes ($\hat{x}_1$ and $\hat{x}_2$) of these two systems are intended to point at each other. Furthermore, the Satellite Frame (SF) $O_p - x_1' y_1' z_1'$, $O_p - x_2' y_2' z_2'$ are defined with origins at proof mass of accelerometer of GRACE A and GRACE B and axes parallel to $O_b - x_1 y_1 z_1$, $O_b - x_2 y_2 z_2$, respectively (GRACE Team, 2002). These coordinate systems are shown in Figure 2.1.

Each GRACE satellite carries two star camera assemblies. The origin of each star camera frame is at the intersection of the optical axis with the mounting plane for the star camera head. The axes, relative to the Satellite Frame, are directed as follows: Star camera 1 has its optical axis ($\hat{z}_{SCF1}$) in the $+\hat{y}_i / -\hat{z}_i$ quadrant, pointed nominally at $45°$ from the $-\hat{z}_i$ direction. The $\hat{x}_{SCF1}$ is parallel to the satellite $\hat{x}_i$ axis. Star camera 2 has its optical axis ($\hat{z}_{SCF2}$) in the $-\hat{y}_i / -\hat{z}_i$ quadrant, pointed nominally at $45°$ from the $-\hat{z}_i$ direction. The $\hat{x}_{SCF2}$ is parallel to the satellite $\hat{x}_i$ axis (GRACE Team, 2002). Where i is a satellite index, SCF1 is star camera 1 index, and SCF2 is star camera 2 index.

Later, the subscript and superscript 1 and 2 of the variables represent GRACE A and GRACE B, respectively. The variable without any script usually is for either of the GRACE satellites.

The legends in Figure 2.1 PMC_1, PMC_2 represent the center of mass of the proof mass of accelerometer, and d_1, d_2 represent proof mass offset from the satellite mass center. These legends are for center of mass calibration. Legends PC_1, PC_2 represent phase center of K-band horn, and d_{pc1}, d_{pc2} are boresight vectors of each K-band horn. These are for the K-band ranging system calibration.
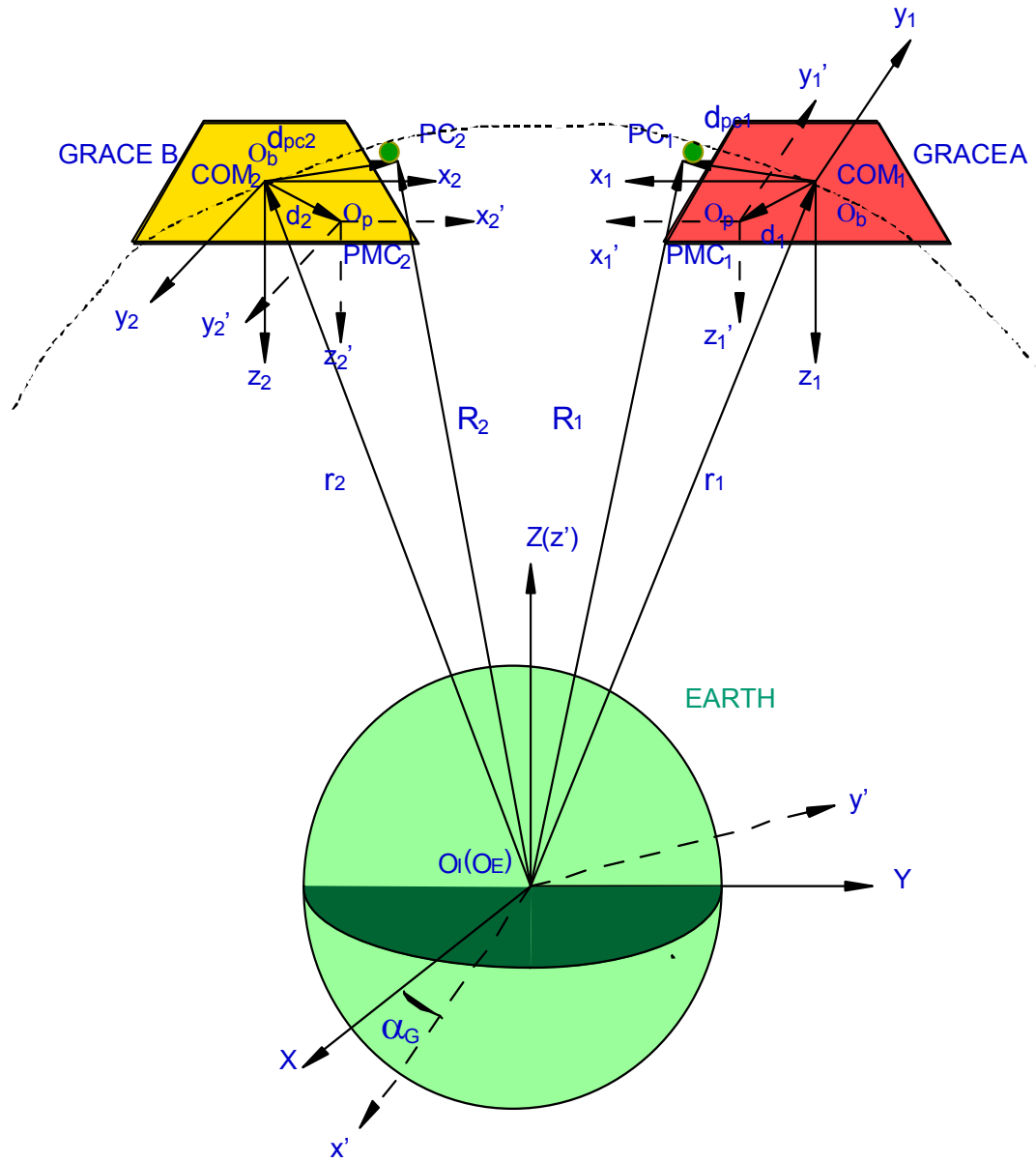
Figure 2.1   Coordinate Systems

2.3 SPACECRAFT ORBIT DYNAMICS MODEL

The spacecraft orbit equations of motion can be described in J2000.0 geocentric non-rotating reference system as follows (Whittaker, 1961)

$$\ddot{\vec{r}} = \vec{f}_g + \vec{f}_{ng} \qquad (2.1)$$

where $\vec{r}$ is the position vector of the COM of the satellite, $\vec{f}_g$ is the sum of the gravitational perturbations acting upon the satellite and $\vec{f}_{ng}$ is the sum of the non-gravitational perturbations acting upon the surfaces of the spacecraft.

2.3.1 Geopotential Gravitational Perturbation

In this research, the gravitational perturbation due to geopotential is only considered for term $\vec{f}_g$. Perturbations due to the solid Earth tides, the ocean tides, rotational deformations, the planets including Sun and Moon and general relativity are ignored. These effects are formulated in detail in Rim, H.J. (Rim, 1992). Neglecting these effects would not affect the simulated center of mass calibration accuracy because they are gravitational perturbations and the accelerometer does not sense gravitational accelerations. As far as the simulated K-band ranging system calibration is concerned, this neglect is reasonable because both satellites are subject to this simplification and only the relative position is measured. Further, the calibration span of both calibrations is short enough that these effects will be small.

The spherical harmonic representation of the Earth gravitational field is given by (Kaula, 1966, Heiskanen and Moritz, 1967)

$$U = \frac{\mu}{r} \sum_{l=0}^{\infty} \left(\frac{a_e}{r}\right)^l \sum_{m=0}^{l} P_{lm}(\sin(\varphi))[C_{lm}\cos(m\lambda) + S_{lm}\sin(m\lambda)] \qquad (2.2)$$

where a_e is the semi-major axis of the Earth's reference ellipsoid, μ is the Earth gravitational constant, r, φ, λ are the radius, latitude, and longitude of the satellite in Earth's body-fixed coordinate system, C_{lm}, S_{lm} are the geopotential harmonic coefficients of degree l and order m, and P_{lm} is the Legendre associate function.

The gravitational perturbation of the satellite due to the attraction of the Earth can be expressed in an Earth centered non-rotating coordinate system as a transformation of the gradient of the potential U. More specifically, $\vec{f}_g$ can be obtained as

$$\vec{f}_g = M_{x'y'z'}^{XYZ} M_{r\varphi\lambda}^{x'y'z'} \nabla U \qquad (2.3)$$

where $M_{x'y'z'}^{XYZ}$ is the rotation matrix from Earth's body-fixed coordinate system to inertial system, $M_{r\varphi\lambda}^{x'y'z'}$ is the rotation matrix from spherical coordinate $(\hat{u}_r, \hat{u}_\varphi, \hat{u}_\lambda)$ to Earth's body-fixed frame, ∇U is the gradient of the geo-potential.

The rotation matrix $M_{r\varphi\lambda}^{x'y'z'}$ can be obtained as follows

$$M_{r\varphi\lambda}^{x'y'z'} = \begin{bmatrix} \cos\varphi\cos\lambda & -\sin\varphi\cos\lambda & -\sin\lambda \\ \cos\varphi\sin\lambda & -\sin\varphi\sin\lambda & \cos\lambda \\ \sin\varphi & \cos\varphi & 0 \end{bmatrix} \qquad (2.4)$$

And the simplified rotation matrix $M_{x'y'z'}^{XYZ}$ is given by

$$M_{x'y'z'}^{XYZ} = \begin{bmatrix} \cos\alpha_G & -\sin\alpha_G & 0 \\ \sin\alpha_G & \cos\alpha_G & 0 \\ 0 & 0 & 1 \end{bmatrix} \qquad (2.5)$$

where, again, α_G is the right ascension of the Greenwich meridian.

2.3.2 Non-gravitational Perturbations

The accelerometer on board the GRACE satellite measures all non-gravitational accelerations. It is intended to separate the non-gravitational accelerations from the periodic proof-mass offset induced accelerations in center of mass calibration. Modeling the non-gravitational accelerations accurately allows the best and most realistic strategy for the separation to be established. Therefore, it is very important to model all non-gravitational accelerations. In this research, atmospheric drag, solar radiation pressure and the Earth radiation pressure are taken into account.

2.3.2.1 Atmospheric Drag

In general, any near-Earth satellite moving with a velocity $\vec{v}$ in an atmosphere of density ρ will experience both lift and drag forces. The lift forces are small compared to the drag forces. The drag force per unit satellite mass can be modeled as follows (Schutz, et al., 1980)

$$\vec{f}_{drag} = -\frac{1}{2}\rho(\frac{C_d A_d}{m})v_r\vec{v}_r \qquad (2.6)$$

where ρ is the atmospheric density, $\vec{v}_r$ is the satellite velocity with respect to the atmosphere, v_r is the magnitude of $\vec{v}_r$, m is the mass of the satellite, C_d is the

drag coefficient for the satellite and A_d is the cross-sectional area of the main body perpendicular to $\vec{v}_r$.

For the trapezoid-shaped GRACE with size of length l, as viewed along pitch axis, and height h, top width tw and bottom width bw, as viewed from the front, the cross-sectional area A_d can be obtained as

$$A_d = \sum_{i=1}^{6} S_i \hat{n}_i \cdot \vec{v}_r / v_r H(\hat{n}_i \cdot \vec{v}_r / v_r) \tag{2.7}$$

where $H(x) = -1$, if $x < 0$, otherwise $H(x) = 0$, $\hat{n}_1 = (1,0,0)^T$, $\hat{n}_2 = (-1,0,0)^T$, $\hat{n}_3 = (0, \sin a, -\cos a)^T$, $\hat{n}_4 = (0, -\sin a, -\cos a)^T$, $\hat{n}_5 = (0,0,1)^T$, $\hat{n}_6 = (0,0,-1)^T$, $S_1 = S_2 = (bw + tw) \cdot h / 2$, $S_3 = S_4 = l \cdot h / \sin a$, $S_5 = bw \cdot l$, $S_6 = tw \cdot l$, $\sin a = \sin(h / \sqrt{c^2 + h^2})$, $\cos a = \cos(c / \sqrt{c^2 + h^2})$ and $c = (bw - tw) / 2$.

The relative velocity $\vec{v}_r$ can be related to the rotation of the atmosphere and the horizontal winds over the Earth as follows (Kim, 2000)

$$\vec{v}_r = \vec{v} - \omega_e \times \vec{r} - \vec{v}_w \tag{2.8}$$

where $\vec{v}$ is the velocity of the satellite in inertial system, ω_e is the rotation rate of the Earth, and $\vec{v}_w$ is the velocity vector of the horizontal winds in the Earth body-fixed system.

The atmosphere subject to short period perturbations can be modeled as follows (Bettadpur, 2000)

$$\rho = \rho_c (1 + \sum_{i=1}^{7} C_i \cos(\frac{t}{T_i} + \phi_i)) \tag{2.9}$$

26

where ρ_c is the nominal computed values of atmosphere density, C_i, T_i and ϕ_i represent the perturbation amplitude, period and phase, respectively.

There are a number of empirical density models used for computing the atmospheric density, such as Jacchia77 (Jacchia, 1977), Drag Temperature Model (DTM) (Barlier, et al., 1977) and Exponential Density Model. In this study, the DTM model is used for simulating the true atmosphere density. The wind model from AMSIS and short period atmospheric density perturbations are taken into account in the atmospheric drag simulation.

2.3.2.2 Solar Radiation Pressure

Compared to the atmospheric drag, the solar radiation pressure has less effect upon the GRACE satellite since the satellite altitude is relatively low. However, unlike the fixed transverse-directed drag acceleration, the perturbation direction of solar radiation pressure is changing with the configuration of the satellite relative to the Sun. This may affect the strategy of filtering the non-gravitational accelerations and derives careful modeling.

The direct solar radiation pressure from the Sun on a satellite can be modeled as (Tapley, et al., 1990)

$$\vec{f}_{solar} = -P(1+\eta)(\frac{A_s}{m})v\hat{u}_{sun} \qquad (2.10)$$

where P is the momentum flux due to the Sun, η is the reflectivity coefficient of the satellite, A_s is the cross-sectional area of the satellite normal to the Sun, v is the eclipse factor ($v=0$ if the satellite is in full shadow, $v=1$ if the satellite is in

27

full Sun, and $0<v<1$ if the satellite is in partial shadow) and $\hat{u}_{sun}$ is the unit vector pointing from the satellite to the Sun.

The cross-sectional area A_s can be obtained by substituting a unit vector of $\vec{v}_r$ with $\hat{u}_{sun}$ in Equation (2.7). The fixed reflectivity coefficient used in the simulation is specified in Table 5.1.

2.3.2.3 Earth Radiation Pressure

Like the direct solar radiation pressure, the radiation imparted by the energy flux of the Earth can induce direction-changed Earth radiation pressure to the satellite. The Earth radiation pressure can be modeled as follows (Knocke, et al., 1987)

$$\vec{f}_{erp} = (1+\eta_e)A'(\frac{A_e}{m \cdot c})\sum_{j=1}^{N}[(\tau a E_s \cos\theta_s + eM_B)\hat{r}_e]_j \qquad (2.11)$$

where η_e is the satellite reflectivity for the Earth radiation pressure, A' is the projected, attenuated area of a surface element of the Earth, A_e is the cross sectional area of the satellite, c is the speed of light, τ is 0 if the center of the element j is in darkness and 1 if the center of the element j is in daylight, a,e are the albedo and emissivity of the element j, E_s is the solar momentum flux density at 1 A.U. (Astronomical Unit), θ_s is the solar zenith angle, M_B is the exitance of the Earth, $\hat{r}_e$ is the unit vector from the center of the element j to the satellite and N is the total number of segments.

The nominal albedo and emissivity models can be represented as

$$a = a_0 + a_1 P_{10}(\sin\phi) + a_2 P_{20}(\sin\phi) \qquad (2.12)$$
$$e = e_0 + e_1 P_{10}(\sin\phi) + e_2 P_{20}(\sin\phi) \qquad (2.13)$$

28

where

$$a_1 = c_0 + c_1 \cos \omega(t - t_0) + c_2 \sin \omega(t - t_0) \qquad (2.14)$$
$$e_1 = k_0 + k_1 \cos \omega(t - t_0) + k_2 \sin \omega(t - t_0) \qquad (2.15)$$

where P_{10}, P_{20} are the first and second degree Legendre polynomial, ϕ is the latitude of the center of the element on the Earth's surface, ω is the frequency of the periodic terms (period=365.25 days) and $t - t_0$ is time from the epoch of the period term.

This model is based on analyses of Earth radiation budgets. It characterizes both the latitudinal variation in Earth radiation and the seasonally dependent latitudinal asymmetry (Rim, 1992).

Likewise, the cross-sectional area A_e can be obtained by substituting $\vec{v}_r$ with $\vec{r}$ in Equation (2.7). The albedo and emissivity parameters used in the simulation are specified in Table 5.1.

2.4 SPACECRAFT ATTITUDE DYNAMICS MODEL

The equations of motion of attitude dynamics can be divided into two sets: the dynamic equations of motion and kinematic equations of motion. Kinematics is the study of motion irrespective of the forces that bring about that motion, while dynamics relate the time dependence of instantaneous angular acceleration to the external forces.

If it is assumed that the mass distribution is constant, the equations of motion for the attitude dynamics can be written in the spacecraft body-fixed coordinate system as follows

$$J \frac{d\omega}{dt} = T - \omega \times (J\omega) \qquad (2.16)$$

where J is the moment of inertia tensor with respect to COM of the spacecraft, ω is the spacecraft's instantaneous angular velocity with respect to the inertial system, T represents the total external torque acting upon the spacecraft.

The moment of inertia tensor J is defined by

$$J = \begin{bmatrix} I_{xx} & I_{xy} & I_{xz} \\ I_{yx} & I_{yy} & I_{yz} \\ I_{zx} & I_{zy} & I_{zz} \end{bmatrix} = \begin{bmatrix} \int(y^2 + z^2)dm & -\int xydm & -\int xzdm \\ -\int xydm & \int(x^2 + z^2)dm & -\int yzdm \\ -\int xzdm & -\int yzdm & \int(x^2 + y^2)dm \end{bmatrix} \qquad (2.17)$$

where x, y, z are the coordinates of the satellite mass elements, dm, in the spacecraft body-fixed system, and the integrals are carried out over the whole spacecraft.

The attitude of any satellite in space can be described by a rotation matrix which transforms the three unit orthogonal axes of the inertial frame to the axes of the satellite body-fixed system. Traditionally, the rotation matrix is called direction cosine matrix or attitude matrix.

Since the rotation motion of the satellite has three degrees of freedom, three angles, widely used as Euler angles, may rigidly describe the rotation matrix. The reference frame can be related to the satellite body-fixed system by three sequential rotations about axes with rotation angles of Euler angles. Any two sequential rotation axes should be different, of course. Therefore, there are totally twelve possible sets of Euler angles between any two coordinate systems, such as 3-2-1 Euler angles, 3-1-3 Euler angles, etc.

When deriving the kinematic equations of motion based on Euler angles, there are always some triangular functions of an Euler angle which appear in the denominator of the transformation equations. This can result in lack of uniqueness in the specification of the other two Euler angles when this Euler angle is a multiple of 180 degrees, thus a singularity in the kinematic equations of motion happens. It is a serious disadvantage associated with using the Euler angle formulation for numerical integration of the equations of motion (Wertz, 1978).

In order to avoid the singularity problem, the attitude quaternion representation is used in this research and has been adopted for the flight software implemented on the GRACE satellites. The definition of the quaternion is based on the Euler's rotation theorem, which states that the most general displacement of a rigid body with one point fixed is equivalent to a single rotation about some axis through that point (Greenwood, 1988). Suppose the rotation axis is $a(a_x, a_y, a_z)^T$ and rotation angle is ϕ, then the attitude quaternion can be defined as follows (Hamilton, 1969)

$$q(t) = \begin{bmatrix} q_1 & q_2 & q_3 & q_4 \end{bmatrix}^T = \begin{bmatrix} a\sin(\phi/2) \\ \cos(\phi/2) \end{bmatrix} \qquad (2.18)$$

An operator, $\Re()$, which maps the attitude quaternion $q(t)$ to the rotation matrix, is defined as follows

$$\Re(q) = \begin{bmatrix} 1-2(q_2^2 + q_3^2) & 2(q_1q_2 + q_3q_4) & 2(q_1q_3 - q_2q_4) \\ 2(q_1q_2 - q_3q_4) & 1-2(q_1^2 + q_3^2) & 2(q_3q_2 + q_1q_4) \\ 2(q_1q_3 + q_2q_4) & 2(q_2q_3 - q_1q_4) & 1-2(q_2^2 + q_1^2) \end{bmatrix} \qquad (2.19)$$

The attitude kinematic equations of motion in terms of attitude quaternion representation is governed by

$$\dot{q}(t) = \frac{1}{2}\Omega(\omega)q(t) \tag{2.20}$$

where

$$\Omega(\omega) = \begin{bmatrix} 0 & \omega_z & -\omega_y & \omega_x \\ -\omega_z & 0 & \omega_x & \omega_y \\ \omega_y & -\omega_x & 0 & \omega_z \\ -\omega_x & -\omega_y & -\omega_z & 0 \end{bmatrix} \tag{2.21}$$

For the integration of the dynamic equations of motion and kinematic equations of motion, the external torque of T must be modeled as a function of time as well as of the position and attitude of the spacecraft. The dominant sources of torques will be modeled in the following sections.

2.4.1 Spacecraft Torques

The external torques can be produced by various sources. For the near-Earth satellites, the main sources of disturbance torques include the Earth's gravitational torque, solar radiation torque, aerodynamic torque and magnetic torque. During the center of mass calibration, the dominating active torque is magnetic torque produced by the magnetorquer system, and during the K-band ranging system calibration, the active torque is the combination of magnetic torque and thruster torque.

2.4.1.1 Gravitational Torque

Because the Earth's gravitational force acting on the spacecraft mass element varies with the distance to the center of the Earth, any satellite is subject to a gravitational torque (Hultquist, 1961). General expressions for the gravity gradient torque on a satellite of arbitrary shape have been calculated for both spherical (Nidey, 1960) and nonspherical (Roberson, 1958, Roberson, 1961) Earth models. In this calibration simulation study, it is sufficient to assume a spherical mass distribution for the Earth to derive the gravitational torque. Based on this assumption, the gravitational torque can be obtained as follows

$$
T_g = 3\left(\frac{\mu}{r^3}\right)\begin{bmatrix} (I_{zz}-I_{yy})c_2c_3 + I_{yz}(c_2^2 - c_3^2) + I_{zx}c_1c_3 - I_{xy}c_3c_1 \\ (I_{xx}-I_{zz})c_3c_1 + I_{zx}(c_3^2 - c_1^2) + I_{xy}c_2c_3 - I_{yz}c_2c_1 \\ (I_{yy}-I_{xx})c_2c_1 + I_{xy}(c_1^2 - c_2^2) + I_{yz}c_1c_3 - I_{zx}c_2c_3 \end{bmatrix} \quad (2.22)
$$

where r is the magnitude of $\vec{r}$, and $[c_1,c_2,c_3]^T$ is the unit vector $\hat{u}$ along $\vec{r}$ expressed in the spacecraft body-fixed system. Therefore

$$
\begin{bmatrix} c_1 \\ c_2 \\ c_3 \end{bmatrix} = \begin{bmatrix} \hat{x}\cdot\hat{u} \\ \hat{y}\cdot\hat{u} \\ \hat{z}\cdot\hat{u} \end{bmatrix} \quad (2.23)
$$

where $\hat{x}, \hat{y}, \hat{z}$ are unit satellite boy-fixed system axes and $\hat{u} = \vec{r}/r$.

2.4.1.2 Spacecraft Aerodynamic and Solar Radiation Torque

The interaction of the upper atmosphere with a satellite's surface produces an aerodynamic torque. The force due to the impact of atmosphere molecules on the spacecraft surface can be modeled as an elastic impact without reflection. The

incident particle's energy is generally completely absorbed. The particle escapes after reaching thermal equilibrium with the surface with a thermal velocity equal to that of the surface molecules. Because this velocity is substantially less than that of the incident molecules, the impact can be modeled as if the incident particles lose their entire energy on collision. The aerodynamic torque T_A acting on the spacecraft is written as (Wertz, 1978)

$$T_A = \int R \times df_{aero} \tag{2.24}$$

where R is the vector from the COM of the spacecraft to surface element dA, and df_{aero} represents the aerodynamic perturbation acting upon this element.

In addition, solar radiation incident on a spacecraft's surface can produce a radiation torque. The solar radiation torque acting upon the spacecraft can be written in the general form as (Wertz, 1978)

$$T_S = \int R \times df_{solar} \tag{2.25}$$

where df_{solar} represent the solar radiation pressure perturbation acting upon this element.

The above two torques are evaluated using a program developed at AMA/LaRC (Bettadpur, 1999).

2.4.1.3 Spacecraft Magnetic Torque

The interaction between the spacecraft's residual magnetic field and the Earth's magnetic field results in a magnetic torque. The primary source of magnetic torque of GRACE satellite is the magnetic moment. Besides this active

torque, which is used for attitude control, there exist some magnetic disturbance torques due to eddy currents and hysteresis. The disturbance torques are simulated by slightly offsetting the nominal magnetic moment in this study.

The instantaneous magnetic torque T_M due to the spacecraft effective magnetic moment m_m (in $A \cdot m^2$) is given by

$$T_M = m_m \times B \tag{2.26}$$

where B is the geocentric magnetic flux density, and m_m is the magnetic dipole moment. During the center of mass calibration, the magnetic torque rods are used to generate a harmonic time dependence magnetic dipole moment at some fixed frequency f_0 to produce the magnetic torque, which will dominate over all other disturbance torques.

The predominant portion of the Earth's magnetic flux density $B(B_r, B_\theta, B_\phi)$ at any point in space can be calculated as follows (Wertz, 1978)

$$\begin{bmatrix} B_r \\ B_\theta \\ B_\phi \end{bmatrix} = \begin{bmatrix} \sum_{n=1}^{k} \left(\frac{a}{r}\right)^{n+2} (n+1) \sum_{m=0}^{n} (g^{n,m} \cos(m\phi) + h^{n,m} \sin(m\phi)) P^{n,m}(\theta) \\ -\sum_{n=1}^{k} \left(\frac{a}{r}\right)^{n+2} \sum_{m=0}^{n} (g^{n,m} \cos(m\phi) + h^{n,m} \sin(m\phi)) \frac{\partial P^{n,m}(\theta)}{\partial \theta} \\ -\frac{1}{\sin\theta} \sum_{n=1}^{k} \left(\frac{a}{r}\right)^{n+2} \sum_{m=0}^{n} m(-g^{n,m} \sin(m\phi) + h^{n,m} \cos(m\phi)) P^{n,m}(\theta) \end{bmatrix} \tag{2.27}$$

where B_r, B_θ, B_ϕ are the Earth's magnetic flux density component along vertically upward, local south direction, and local east direction, respectively, a is the equatorial radius of the Earth (6371.2 km adopted for the International Geomagnetic Field, IGRF), r, θ, ϕ are the geocentric distance, coelevation, and

35

east longitude from Greenwich which define any point in space, $g^{n,m}, h^{n,m}$ are coefficients derived from Gaussian coefficients and $P^{n,m}(\theta)$ is the Gauss function related to Schmidt functions by some factors. Compared to the spherical coordinate defined in Section 2.3.1, θ is equal to $90^o - \varphi$, and ϕ is equal to λ. Equation (2.27) can be carried out if r, θ, ϕ and the IGRF Gaussian coefficients are given. In this research, the Earth's magnetic flux density is obtained from above spherical harmonic model by taking the IGRF 95 Gaussian coefficients.

The geocentric inertial components (B_X, B_Y, B_Z) can be obtained from (B_r, B_θ, B_ϕ) by the rotation matrix $M_{r\theta\phi}^{XYZ}$, which is given by

$$M_{r\theta\phi}^{XYZ} = \begin{bmatrix} \cos\delta\cos\beta & \sin\delta\cos\beta & -\sin\beta \\ \cos\delta\sin\beta & \sin\delta\sin\beta & \cos\beta \\ \sin\delta & -\cos\delta & 0 \end{bmatrix} \qquad (2.28)$$

where β is the right ascension and δ is the declination of the spacecraft. δ is equal to latitude φ and β is related to longitude ϕ by $\beta = \phi + \alpha_G$.

Given the attitude quaternion of the satellite $q(t)$, the magnetic flux density B expressed in satellite body-fixed system can be obtained by

$$B = \begin{bmatrix} B_x \\ B_y \\ B_z \end{bmatrix} = M_{XYZ}^{xyz} M_{r\theta\phi}^{XYZ} \begin{bmatrix} B_r \\ B_\theta \\ B_\phi \end{bmatrix} \qquad (2.29)$$

where the rotation matrix M_{XYZ}^{xyz}, rotating from the geocentric inertial system to satellite body-fixed system, can be known as $\Re(q)$.

36

2.4.1.4 Thruster Torque

The GRACE cold gas system uses Nitrogen as medium, which is stored in two tanks at an initial pressure of 350 bars. This upstream pressure is reduced to the thruster valves working pressure of approximately 1.5 bars by a pressure regulator (Schelkle, 1999). For redundancy reasons, the two branches can be operated individually. Attitude control around the roll, pitch and yaw axis is performed by three sets of four thrusters with a nominal thruster force of 10 mN. The attitude control thrusters are nominally operated in pairs which are accommodated such that force free reaction control is achieved. For orbit maintenance, two 40 mN thruster are mounted on the anti-flight direction side with the force vector pointing through the COM of satellite (GRACE Team, 1998c). The resulting thruster torque which controls the yaw and pitch axis is $\pm 0.015 N \cdot m$ and controls the roll axis is $\pm 0.003 N \cdot m$ (GRACE Team, 1999a).

So far, all perturbations and external torques considered in this research have been modeled. The spacecraft orbit equations of motion, attitude dynamic equations of motion and attitude kinematic equations of motion can be integrated together to simulate the true orbit and attitude of spacecraft. The integration state is chosen as $X = \begin{bmatrix} \vec{r} & \vec{v} & q & \omega \end{bmatrix}^T$, which is a 13-dimension vector.

As a summary, the dynamics equation is written as

$$\dot{X} = \begin{bmatrix} \vec{v} \\ \vec{f}_g + \vec{f}_{ng} \\ \dfrac{1}{2}\Omega(\omega)q(t) \\ J^{-1}(T - \omega \times (J\omega)) \end{bmatrix} \tag{2.30}$$

37

These equations of motion are numerically integrated using of the Runge-Kutta (7) 8 integrator (Fehlberg, 1968). At any integration step, besides the known state vector, the angular acceleration $\dot{\omega}$, non-gravitational acceleration $\vec{f}_{ng}$ and the Earth's magnetic flux density B will be recorded for later use in the observation data generation.

Chapter 3: Calibration Maneuver Design and Observation Models

3.1 INTRODUCTION

The objective of center of mass calibration is to determine the accelerometer proof mass offset from the satellite mass center experimentally during the in-flight phase and then eliminate or reduce this offset by using the satellite Mass Trim assembly Mechanism. Although the maneuver design and data processing algorithms appear complicated, the scheme for this calibration is straightforward. Simply speaking, the accelerometer observation itself is a function of the proof mass offset and other variables. If all the other variables are known or can be fitted by some functions, the proof mass offset can be easily determined from the accelerometer observations. These variables include non-gravitational accelerations, angular velocity and angular acceleration. The angular velocity and angular acceleration are combined with the proof mass offset to produce the angular motion induced disturbance acceleration. These two variables can be derived from the quaternion observations of the star camera by fitting these observations to the attitude dynamic equations of motion or kinematic equations of motion. The non-gravitational accelerations are smooth compared to the angular motion induced acceleration since the satellite is subject to frequent but infinitesimal variations during this calibration. Therefore, the non-gravitational accelerations can be easily separated from the angular motion related acceleration, from which the proof mass offset can be determined.

The accelerometer, star camera and magnetometer provide the necessary observation data for the GRACE center of mass calibration. The SuperSTAR accelerometer measures all non-gravitational spacecraft accelerations and disturbance accelerations if the proof mass offset exists. The accelerometer measurements directly reflect proof mass offset which can be estimated provided that the fitting non-gravitational accelerations model and angular motion information are available. The non-gravitational accelerations can be filtered by polynomial functions while the angular motion information can be totally determined by observations of the magnetometer and star camera. The magnetometer measures the Earth's magnetic field. Given the magnetic moments activated on board, the dominating magnetic torques can be fully determined.. In addition, the spacecraft attitude orientation with respect to the inertial space can be obtained from the star camera's observations. The dominating active torque and attitude quaternion data can be fitted into the attitude equations of motion to determine the time-varying angular motion information. With this information, the proof mass offset can be determined. After the proof mass offset is known, a satellite command allows the MTM system to perform mass balance within the satellite. Ideally, the proof mass offset can be totally removed so that the accelerometer is free from the disturbance accelerations. In practice, an offset below the requirement of 0.1 mm can be achieved.

The purpose of the K-band ranging system calibration is to determine the phase center of the microwave antenna on board each GRACE satellite. This determination allows the Attitude and Orbit Control System (AOCS) to adjust the

attitude orientations of both satellites such that the phase centers of two K-band horns and COMs of two GRACE satellites are nearly along a straight line, and allows the post-processing of the KBR phase measurements to make alignment corrections to derive the biased range between the COMs of the twin satellites. There are two types of K-band ranging system calibration maneuvers investigated in this study. One is based on a periodic oscillation maneuver, and the other is based on a linearly drifting maneuver. Both maneuvers make use of the nature of the antenna's phase center and experimentally determine the phase center location in the satellite body fixed reference frame. That concept is based on the attempt to rotate the antenna along certain axis to find a reference point which produces minimum variation in the observed phase response. The major difference of these two maneuvers is in how the angular variations are generated. The periodic oscillation maneuver oscillates the satellite about a biased angle. The relative orbit determination errors can be largely removed in this kind of maneuver since they are quite smooth compared to the periodic angular variation. However, the multipath errors of the antenna will be the dominating errors in this case. As an alternate, the linearly drifting maneuver is implemented so as to linearly rotate the satellite. Actually, it is just a half period of a periodic oscillation maneuver that may have several reoccurrences in the whole maneuver. Thus the calibration span is much shorter. However, the relative orbit determination errors are hard to remove in this case, which could have a significant impact on the calibration accuracy. Processing the range rate data instead of range data may improve the calibration results since the angular information helps in this situation.

For the case of K-band ranging system calibration with the periodic oscillation maneuver, the required observation data include K-band ranging system observations, star camera observations and Precise Orbit Determination (POD) from GPS observations. The K-band ranging system measurements can be converted to the biased range and its change between the phase centers of the antennas, which, ideally, are the same as the range and range rate between the COMs of both satellites. The range measurements directly reflect the motion of the phase center, which can be determined provided that the orbit and attitude information of both satellites are available. One major function of the star camera during this maneuver is to provide spacecraft attitude information for the on-board AOCS system to oscillate the satellite in the designed manner. The observations from the star camera are used to describe the satellite's attitude orientations when determining the phase centers from the observed data set. The GPS receiver assembly on board each satellite allows a high accuracy of the orbits of the satellite to be determined. As a matter of fact, only the relative position between two satellites exists in the KBR range measurement. Due to some similar perturbations upon the twin satellites, the relative position may be improved as opposed to orbit determination of one single satellite because of some cancellations. This might be helpful to the estimation system.

On the other hand, in case of the K-band ranging system calibration with the linearly drifting maneuver, the K-band ranging system, star camera, POD by GPS, and magnetometer constitute a complete instrument set for data collection. In this study, the KBR range rate data are processed to reduce the relative position

determination effects. The range rate measurement includes relative position and velocity of two satellites, angular velocity of each satellite and attitude of each satellite. The relative position and velocity can be determined accurately from the GPS observations. The spacecraft attitude can be determined by the star camera observations. Finally, the spacecraft angular velocity can be obtained by fitting the dominating active torques, known by the magnetometer observation data and activated magnetic moment data, and the attitude quaternion data into the attitude equations of motion. The angular velocity and angular acceleration are determined in the same way as in the center of mass calibration. In this study, it is assumed that the active magnetic torque applied to the satellite could be used to improve the angular velocity determination. However, this may not be true if the true magnetic torque is largely different from the calculated torque. In this case, there is no reason to operate the magnetic torque actively, and the angular velocity is determined by fitting zero environmental torque into the attitude equations of motion.

In the following sections, the center of mass calibration and K-band ranging system calibration maneuvers will be designed. The maneuver parameters will be determined based on the simulations in Chapter 5.

In addition, the characteristics of the observation instruments will be presented and their measurement models will be established. Based on these models, the observation data will be simulated.

3.2 COM CALIBRATION MANEUVER DESIGN

The center of mass calibration can be individually carried out by each GRACE satellite since the calibration maneuvers for each satellite are totally independent. The COM calibration maneuver can be designed as follows:

During a time interval T_0, periodic magnetic torques with frequency f_0 are applied to the satellite in the absence of thruster firings. The parameters and factors that must be taken into account in the COM calibration design include: magnetic dipole moment m_m, magnetic moment frequency f_0, calibration time span T_0 and the location over the Earth.

The key point of the GRACE COM calibration is that the magnetic dipole moments m_m are activated with a harmonic time dependence at some fixed frequency f_0, thus creating a dominant fixed frequency over the wide-band frequency noise of the accelerometer data. The accelerometer's observations include both non-gravitational accelerations and disturbance accelerations, which are mainly angular motion related accelerations. During the COM calibration, the angular motion related accelerations will be the dominating disturbance accelerations as the periodic terms in the accelerometer observations and the non-gravitational accelerations are quite smooth and can be linearly filtered, which allows the proof mass offset to be determined with high accuracy. In addition, by applying suitable periodic magnetic torques to the satellite without using the thruster torques, the magnetic torque will dominate over the environmental torques, which include the solar radiation torque and aerodynamic torque. Those disturbance torques are hard to be modeled, but can be ignored since they are

infinitesimal compared to the active magnetic torque. Therefore, a very accurate model of the torques upon the satellites can be developed. The angular velocity and acceleration can be accurately determined from the attitude equations of motion given the accurate calculated torques.

The magnetic torques are realized by the MTQ system, which consists of three magnetic torque rods and pertinent drive electronics. The magnetic torque rods are electromagnets generating a dipole moment m_m which, when interacting with the Earth's magnetic field, produces a torque about an axis given by the mathematical vector product of the rod's longitudinal axis and the field vector of the Earth's magnetic field at the actual orbit position.

An optimal way to implement the magnetic dipole moment m_m is to maximize the magnetic torque on the satellite given the Earth's magnetic field $B(B_x, B_y, B_z)$ experienced by the magnetic rods. However, the resulting angular motion may be not optimal from the proof mass offset determination point of view. The strategy for activating the magnetic moments will be investigated thoroughly in the Section 3.4.

As stated above, the non-gravitational accelerations are approximated by linear functions. In fact, this is valid only for a limited time span. Theoretically, a longer time span, which means more observation data, can improve the COM calibration accuracy, but the non-gravitational accelerations cannot be approximated by linear terms over such an interval. Consequently, the proof mass offset estimation proposed in the following chapters will not yield good results. So it is suggested that there is a tradeoff between more calibration data (longer

time span T_0) and the validity of linearly fitting of the non-gravitational accelerations. For this reason, the time interval of calibration is designed to be 1~10 minutes. In fact, 3~5 minutes is long enough to achieve good estimation accuracy of the proof mass offset. This will be demonstrated later in the simulations. Since repitions have to be performed in order to accurately estimate the proof mass offset, the calibration time span is also constrained by the magnetic moment frequency f_0.

Another important design factor is the satellite's location over the Earth. This is because the resultant magnetic torques depend on the Earth's magnetic field which varies with locations. The angular velocity and angular acceleration will be quite different with respect to different geographic locations even if the same magnetic moments are activated. In fact, as will be shown later, the magnitude of the angular acceleration along each axis can have a direct impact on the calibration accuracy. The optimal calibration timing will be explored in the following chapters.

These maneuver parameters will be settled after complete simulations are done.

3.3 KBR CALIBRATION MANEUVER DESIGN

The phase centers of two GRACE satellite antennas are highly correlated when processing the observation data. Given a maneuver of any kind, the KBR phase measurement depends on both phase centers of K-band horns, but it is only sensitive to the phase center component along the sweep plan of the rotating satellite. Only with multiple maneuvers, can the phase centers of both K-band

horns be determined. In this study, four separate K-band ranging system calibration sub-maneuvers are proposed to overcome such correlation problem. After four sub-maneuvers, all of the observation data are combined to estimate the phase centers of the GRACE satellite antennas. As mentioned in the previous sections, two different calibration maneuvers are investigated in this study.

In the following designs of the KBR calibration, the satellite under test always has a biased attitude angle. The reason why the angular motion is initialized with a biased angle is because the attitude motion induced range change increases with the biased angle. Hence, the KBR observation is more sensitive to the attitude motion. This can be verified by differentiating the phase observation about the angle in Equation (1.2).

First, the periodic oscillation maneuver is presented. The four sub-maneuvers are designed as follows:

Sub-Maneuver A: In this sub-maneuver, a yaw angle $\theta_{\circ}$ with respect to the nominal attitude is performed for GRACE A by applying suitable torques to this satellite. Then activate torques to oscillate the yaw angle θ_{yaw}^{1} about the biased angle as follows

$$\theta_{yaw}^{1} = \theta_{\circ} + A\sin(\omega t) \qquad (3.1)$$

The active torques exerted upon the satellite need to be carefully designed such that the attitude orientations could be in the above form. The attitude control module on board GRACE satellite has been designed to automatically compute the necessary torques, i.e., the combination of thruster torque and magnetic torque, which force the satellite to follow the designed attitude track. During this

sub-maneuver, the roll and pitch angles of GRACE A deviating from the nominal should be kept as small as possible and the GRACE B has to be kept with its nominal attitude. In this case, the phase observation is highly sensitive to phase center of GRACE A's antenna along roll and pitch axes. The schematic illustration of this sub-maneuver is shown in Figure 3.1.
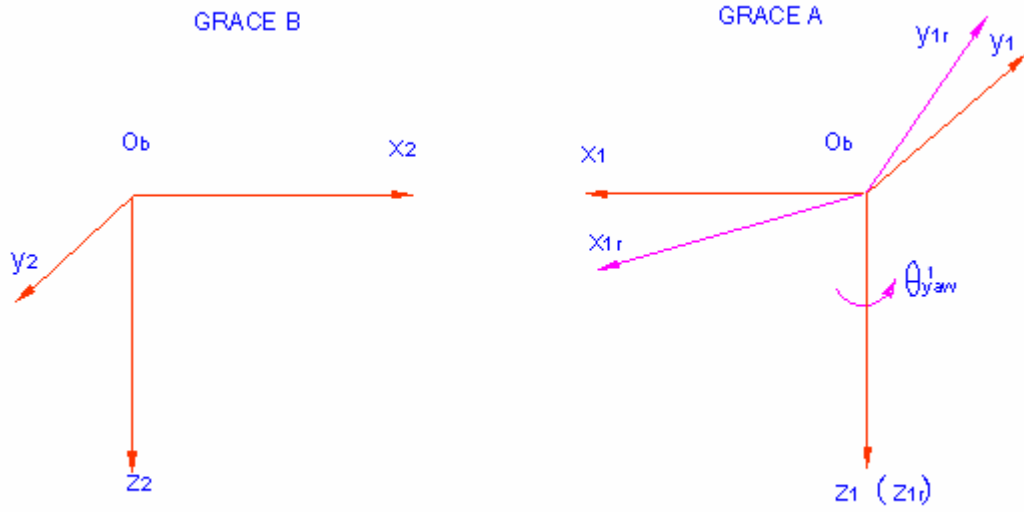
Figure 3.1   The Schematic Illustration of Sub-Maneuver A

Sub-Maneuver B: This sub-maneuver is the same as sub-maneuver A except that a pitch angle variation is driven, instead of yaw angle variation, as

$$\theta^1_{pitch} = \theta_\circ + A\sin(\omega t) \tag{3.2}$$

Likewise, in this sub-maneuver, the phase observation is highly sensitive to phase center of GRACE A's antenna along roll and yaw axes.

48

Sub-Maneuver C: In this sub-maneuver, a yaw angle $\theta_\circ$ with respect to the nominal attitude is initially biased for GRACE B. Then its attitude is driven by automatically computed torques such that the yaw angle variation θ^2_{yaw} varies as follows

$$\theta^2_{yaw} = \theta_\circ + A\sin(\omega t) \qquad (3.3)$$

In this sub-maneuver, the phase observation is highly sensitive to phase center of GRACE B's antenna along roll and pitch axes.

Sub-Maneuver D: This sub-maneuver is the same as sub-maneuver C except that a pitch angle variation is driven as

$$\theta^2_{pitch} = \theta_\circ + A\sin(\omega t) \qquad (3.4)$$

The phase observation is highly sensitive to phase center of GRACE B's antenna along roll and yaw axes in this sub-maneuver.

The sine function in Equations (3.1) through (3.4) can be in any other periodic forms. In fact, being periodic is not required. The variation angle can be oscillated in any manner around the biased angle as long as the maximum amplitude is reached. In practice, the period of the oscillation $2\pi/\omega$ is constrained by the AOCS system since the automatically computed torques have to be long enough to drive the attitude following the designed track. The period depends on the moment of inertia of the satellite and angular variation amplitude A, which are important design parameters. The larger amplitude will produce more sensitive phase change, but it may result in a change of the phase center.

Recall that the phase center can be approximately fixed only within certain range of variation angles.

For simplicity of simulation, in the real orbit and attitude dynamics propagation, the active torque control is bypassed. At each integration step, the objective attitude is assumed to be the real attitude. Based on the designed orbit and this objective attitude, the environmental disturbance torques and orbit perturbations are obtained for numerical integration of the translational and rotational equations of motion while all the observation data are simulated. This may not exactly reflect the reality, but it is the easiest way to simulate this maneuver and the accuracy is adequate to assess the calibration accuracy.

The sub-maneuvers of linearly drifting maneuver are designed as follows:

Sub-Maneuver A: In this sub-maneuver, the yaw thruster torque will be applied to GRACE A for a time span (~18 seconds) while free flight of GRACE B, and then both satellites will orbit without attitude control for a couple of seconds to prepare transition to the next maneuver state. After that, the periodic magnetic torques with frequency f_0 will be applied to both satellites for a time interval T_0 in the absence of thruster firings.

Like the sub-maneuver A in the periodic oscillation maneuver, the K-band ranging system observation in this sub-maneuver is highly sensitive to roll and pitch axes of the K-band horn of GRACE A. Since the thruster torque applied initially is very large, it can produce a large angular velocity and angular acceleration before it stops firing. The magnitude of the magnetic torque applied at the last calibration stage is much smaller than that of the thruster torque applied

50

at the first stage. Therefore, the attitude orientation of GRACE A can be approximated to be linearly drifting at the final stage. The corresponding yaw angle deviation can be approximated as

$$\theta_{yaw}^1 \approx \theta_1 + Bt \qquad (3.5)$$

where θ_1 and B represent the initial angle bias and angle rate of change at the last calibration stage. Unlike the process of computing torques in the periodic oscillation maneuver, the active torques in this calibration are known in the simulations since they will be commanded if it actually tests.

Sub-Maneuver B: In this sub-maneuver, the pitch thruster torque will be applied to GRACE A for a time interval, about 15 seconds, while free flight of GRACE B, and then both satellites will fly freely for 5 seconds. Note that the thruster firing time span is different from sub-maneuver A since the angular velocity is mainly along pitch axis. After that, both satellites are subject to the active magnetic torques for a time interval T_0 without thruster control. In this sub-maneuver, K-band ranging system observation is highly sensitive to the roll and yaw axes of K-band horn of GRACE A. The angle deviation is

$$\theta_{pitch}^1 \approx \theta_1 + Bt \qquad (3.6)$$

Sub-Maneuver C: This sub-maneuver is the same as sub-maneuver A except the thruster torque is applied to GRACE B while GRACE A is in free flight. In this sub-maneuver, the K-band ranging system observation is highly

sensitive to the roll and pitch axes of K-band horn of GRACE B. Likewise, the angle deviation is

$$\theta^2_{yaw} \approx \theta_1 + Bt \qquad (3.7)$$

Sub-Maneuver D: This sub-maneuver is the same as sub-maneuver B except the thruster torque is applied to GRACE B initially, and this sub-maneuver is highly sensitive to roll and yaw axes of K-band horn of GRACE B. The angle deviation can be approximated as

$$\theta^2_{pitch} \approx \theta_1 + Bt \qquad (3.8)$$

As stated above, all of the four sub-maneuvers have three phases. In the first phase, the thruster torque is applied to the KBR calibrated satellite to initialize the angular velocity for the next two phases. Then a transition stage with no active torques follows to allow the satellite system be ready for the attitude control. Finally the magnetic torques are applied to both satellites to dominate the disturbance torques, in a way that the angular velocity can be determined accurately from the attitude dynamic equations of motion. In this stage, the attitude orientation can be approximated to be linearly drifting. In fact, this is the reason that the maneuver is called the linearly drifting maneuver.

In practice, since the maximum thruster firing time span is 10 seconds in the GRACE mission (GRACE Team, 1999b), the thruster firings at the first phase of all sub-maneuvers can be realized by two continuous thruster firings.

Whichever KBR calibration maneuver, the phase center of K-band horn of GRACE A can be determined from sub-maneuver A and B, and phase center of

K-band horn of GRACE B can be determined from sub-maneuver C and D. In the real mission, four mirror sub-maneuvers, which are the same as the above four sub-maneuvers except that the biased angle is $-\theta_\circ$ $(-\theta_1)$ instead of $\theta_\circ$ (θ_1). They are implemented for two purposes, one is to back up the maneuver observations, and the other is to possibly cancel some errors by processing the data in a combined manner. Furthermore, the sub-maneuvers can be executed in any order favorable to realization.

3.4 MAGNETORQUER SYSTEM AND MOMENTS DESIGN

The magnetorquer system employs the induction of a reaction torque vector T on a magnetic dipole moment vector $m_m(m_x, m_y, m_z)^T$ when exposed to the Earth magnetic field vector $B(B_x, B_y, B_z)^T$ according to the vector product formula $T = m_m \times B$, as described before. The magnetic dipole moment m_m is given by vectorial superposition established by the three individual dipole moments. Any direction of m_m can be established using by at least three magnetic rods such that the rods' longitudinal axes mark an orthogonal coordinate frame. The magnetorquer system consists of three magnetic torque rods and pertinent drive electronics (GRACE Team, 1998b). Each of the three rods consists of a cylindrical core and two coils. Both coils are galvanically isolated, and the coils' axis is the same as the cylinder axis of the magnetic core. Each such coil is connected to its individual driver stage, an H-bridge, inside the OBDH (On Board Data Handling). The characteristics of the MTQ system of the GRACE satellite are outlined in Table 3.1 (GRACE Team, 1998b).

Table 3.1 Characteristics of the MTQ System

CHARACTERISTICS OF MAGNETIC TORQUER SYSTEM
Minimum Linear Momentum Range: $-30\,Am^2$ to $+30\,Am^2$
Maximum Saturation Momentum (any current input) $\pm 35 + 10\%\,Am^2$
Maximum Residual Momentum at zero input current $\pm 0.2\,Am^2$
Alignment Error: $0.06°$ any two parallel axes (Roll, Yaw, Pitch)

During the calibration, the active magnetic torques are intended to be periodic and dominating over the environmental torques. The magnetic dipole moment m_m should be activated at least along two axes in order that each of the three components of the resultant torque is dominating over the disturbance torques along that axis.

In this study, three approaches for activating the magnetic moments are investigated. Maximizing the magnetic torques along each axis is used in the linearly drifting KBR calibration. However, this approach may be not feasible for COM calibration since the maximum torque solution may result in badly distributed angular acceleration along each axis. The covariance analysis, derived in Section 4.2.6, tells that the angular acceleration along each axis should be of the same order in order that the proof mass offset along three axes can be determined accurately. The angular accelerations are determined by the magnetic moments and the Earth's magnetic field. Therefore, magnetic dipole moment design for COM calibration must take the profile of the Earth's magnetic field into account such that the derived angular accelerations are evenly distributed

along three axes. This is the second approach to the design of the magnetic moments. In practice, there is another way to generate the magnetic torque. Instead of commanding magnetic moments, the expected torque is tele-commanded. The on board instruments will automatically compute the magnetic moment to be activated. This approach is used for the COM calibration in the GRACE mission and deserves a careful formulation. For realization simplicity, only two axes are activated when commanding the magnetic moment.

Let us discuss commanding the magnetic moment first. In this case, the magnetic moment $m_m(m_x, m_y, m_z)^T$ needs to be defined. Given the designed and tele-commanded moment m_m and the measured or calculated Earth's magnetic field B, the induced magnetic torque is $T = m_m \times B$. Considering the saturation boundary, the magnetic moment is subject to the mathematical set equality $(m_x, m_y, m_z) = (0, \pm30F(t), \pm30F(t))$, where $F(t)$ is a periodic function with unit magnitude, such as a sine function or a waveform function. Although the B field is time-varying, it is nearly constant over the short time span of the calibration maneuver and the solution of magnetic moment m_m can be determined from the B field at the calibration initial epoch.

It is assumed that $|B_i| > |B_j| > |B_k|$, where $\{i, j, k\} = \{x, y, z\}$. Through a simple derivation, it can be found that the maximizing magnetic torque solution is $m_i = 0$, $m_k = \pm30F(t)$, $m_j = \mp1 sign(B_j B_k)30F(t)$, where $sign(s)$ is 1 if $s > 0$, is 0 if $s = 0$, is -1 if $s < 0$.

For COM calibration, considering the profile of the Earth's magnetic field, it has been found that magnetic moment activated along y and z axes can yield

55

magnitude-balanced angular accelerations. Therefore, the magnetic moment solution is $m_x = 0$, $m_y = \pm 30 F(t)$, $m_z = \mp sign(B_y B_z) 30 F(t)$.

In the simulations, the resultant magnetic torque, given the magnetic moments in above expression, can be modeled as follows

$$T = R_{mis}(\varepsilon_1, \varepsilon_2, \varepsilon_3) \Theta(m_m \times B) \qquad (3.9)$$

where Θ is an operator to transform a vector into column matrix form and R_{mis} is the misalignment error matrix.

Suppose that the misalignment error angles are $(\varepsilon_1, \varepsilon_2, \varepsilon_3)$, then by the operator $\Xi()$, which maps the small angles to the rotation matrix, R_{mis} can be written as follows

$$R_{mis} = \Xi(\varepsilon_1, \varepsilon_2, \varepsilon_3) = \begin{bmatrix} 1 & \varepsilon_3 & -\varepsilon_2 \\ -\varepsilon_3 & 1 & \varepsilon_1 \\ \varepsilon_2 & -\varepsilon_1 & 1 \end{bmatrix} \qquad (3.10)$$

In the simulations, the misalignment error angles are assumed to have values of $0.06°$.

When commanding the expected torque, says T_e, the magnetic moment is calculated as follows for the GRACE mission

$$m_m = k M_e F(t) \qquad (3.11)$$

where M_e is equal to $B_c \times T_e$, and k is equal to MM_A / M_{max}, in which B_c is the Earth's magnetic field. B_c can be obtained from a magnetic field model or from direct measurement by the magnetometer, and of course, B_c contains either the

model error or the measurement error. MM_A is the maximum saturation momentum, which is $30 Am^2$ for the GRACE mission. $M_{\max}$ is the maximum of the absolute of each component of M_e.

In practice, the expected magnetic torque is only along one axis and it is always very large in order to assure that the magnetic moment is saturated at least along one axis. For example, T_e is $\begin{bmatrix} 1. & 0 & 0 \end{bmatrix}^T N \cdot m$ is the commanded torque along the roll axis. For this research, the commanded expected torque along the roll, pitch, and yaw axis is called the roll maneuver, pitch maneuver and yaw maneuver, respectively.

In the simulations of the orbit and attitude propagation with the expected torque commanded, the B_c is assumed to be measured by the magnetometer, as modeled in Section 3.7, and the resultant torque is produced by the calculated magnetic moment m_m and real magnetic field B. The calculation formula is given by Equation (3.9). However, in practice, there also exists the magnetic moment residue. In this study, it is simulated by offsetting the magnetic moment by 1~2 $A \cdot m^2$ along each axis.

3.5 ACCELEROMETER INSTRUMENT AND SIMULATION DATA

3.5.1 Instrumentation Design Features

The GRACE Accelerometer (ACC) works by electrostatically controlling the position of a proof mass between capacitor plates that are fixed to the spacecraft. By means of two capacitive sensors on each of the three axes the instantaneous position of the proof mass is derived, and electrical signals picked up from the electrodes are a measure of the forces needed to keep the proof mass

centered motionless in the cage. While gravitation affects both the proof mass and the spacecraft, non-gravitational forces affect only the spacecraft. Knowing the mass of the proof mass, the non-gravitation acceleration vector can be derived.

The GRACE accelerometer is derived from the ASTRE and STAR accelerometers that have been developed by the Office National d'Etudes et de Recherches Aerospatiales (ONERA) for the European Space Agency (ESA) and for the French Space Agency CNES. While the configuration of the sensor head has been adapted to the GRACE environment, the operation and technology are identical.

The STAR accelerometer, which is the French contribution to the German CHAMP (CHAllenging Micro-satellite Payload) mission, has a planned resolution of $10^{-9} ms^{-2}$ integrated over the frequency bandwidth of $2 \times 10^{-4} Hz$ to $0.1 Hz$. Its full-scale range is $10^{-3} ms^{-2}$. The expected resolution is based on accepted error source analysis, and the sensor head geometry is based on results from the ASTRE model.

The GRACE accelerometer model (SuperSTAR) benefits from this development. Because of the GRACE orbit and the low-vibration design of the spacecraft, the full-scale range has been reduced to $5 \times 10^{-5} ms^{-2}$. This, combined with 0.1-K thermal control, allows the sensor core capacitive gaps to be increased from $75 \mu m$ to $175 \mu m$ and the proof mass offset voltage to be reduced from 20V to 10V. This results in a smaller acceleration bias by a factor of 20, and more importantly, bias fluctuations are also reduced by a factor of 20. The combined

effect of these changes is a resolution on the order of $10^{-10} ms^{-2}$ over the frequency bandwidth of $2 \times 10^{-4} Hz$ to $0.1 Hz$ (Davis, et al., 1999).

The accelerometer is intended to measure the non-gravitational accelerations, meanwhile it picks up the disturbance accelerations due to the proof mass offset. The accelerometer observation is the real acceleration, which is experienced by the accelerometer, corrupted by scale, bias, and noise. Transforming the accelerometer output in the satellite body-fixed frame yields

$$A_{out} = R_{AB}(s_1 \cdot a_{out} + s_2 \cdot a_{out}^2 + s_3 \cdot a_{out}^3 + A_b + A_n) \qquad (3.12)$$

where R_{AB} is the rotation matrix from accelerometer frame to satellite body-fixed system. There exist the axis order differences between these two frames. However, for simplicity, in the simulation, the axis orders are assumed to be the same and the rotation matrix is described only by the misalignment error angles. In addition, a_{out} represents the real acceleration, s_1, s_2, s_3 are the scale factor diagonal matrices, A_b is the bias diagonal matrix, and A_n is the measurement noise diagonal matrix. The characteristics of scale factors, bias and noise are specified in Table 3.2 (GRACE Error Budget, 1999).

Table 3.2   Characteristics of the Accelerometer

VALUE SPECIFICATION OF SCALE FACTORS AND BIAS
$s_1 = 1.0 \pm 1\%$ roll, pitch, yaw
$s_1 = 1.0 \pm 0.01\% / yr$ roll; $s_1 = 1.0 \pm 1\% / yr$, pitch; $s_1 = 1.0 \pm 0.2\% / yr$, yaw
$\|s_2\| < 20 m^{-1} \cdot s^2$, roll and yaw; $\|s_2\| < 50 m^{-1} \cdot s^2$, pitch
$\|s_3\| < 10^4 m^{-2} \cdot s^4$, roll and yaw; $\|s_3\| < 10^5 m^{-2} \cdot s^4$, pitch
$\|A_b\| < 2.10^{-6} m \cdot s^{-2}$, roll and yaw; $\|A_b\| < 5.10^{-5} m \cdot s^{-2}$, pitch
NOISE POWER SPECTRUM DENSITY
$PSD(f) < (1 + \dfrac{0.005 Hz}{f}) \times 10^{-20} m^2 s^{-4} Hz^{-1}$ roll, yaw
$PSD(f) < (1 + \dfrac{0.1 Hz}{f}) \times 10^{-18} m^2 s^{-4} Hz^{-1}$ pitch

3.5.2 Accelerometer Data Simulation

The real linear acceleration sensed by the accelerometer is given by

$$a_{out} = \ddot{d} + \dot{\omega} \times d + 2\omega \times \dot{d} + \omega \times (\omega \times d) + gg + a_{ng} \qquad (3.13)$$

where d is the proof mass offset, $\dot{d}$ and $\ddot{d}$ are time derivatives carried out with respect to the satellite body-fixed system, $\dot{\omega}$ is the spacecraft's instantaneous angular acceleration with respect to the inertial system, gg is the acceleration due to gravity gradient and a_{ng} is the non-gravitational accelerations acting upon the satellite. During the nominal mission phase, a_{ng} is the dominating term of the accelerometer output, and all the other terms are considered as disturbance accelerations.

For displaced proof mass off the center of mass, gravity and centrifugal forces are no longer balanced completely, giving rise to an acceleration which is proportional to this displacement. Assumed that the Earth is a spherically symmetrical mass, the acceleration due to the gravity gradient, gg, is given by the difference of the gravitational acceleration at the proof mass location and at center of mass as follows (Carpenter, et al., 1986, Wang, et al., 2002b)

$$gg = \frac{\mu}{((\vec{r}+d)\cdot(\vec{r}+d))^{3/2}}(\vec{r}+d) - \frac{\mu}{(\vec{r}\cdot\vec{r})^{3/2}}\vec{r} \qquad (3.14)$$

Expanding the above equation and ignoring the higher order terms permit a simple expression to be derived as follows

$$gg = \frac{\mu}{(\vec{r}\cdot\vec{r})^{3/2}}(d - 3\frac{(\vec{r}\cdot d)}{(\vec{r}\cdot\vec{r})}\cdot\vec{r}) \qquad (3.15)$$

Rewriting the above equation with notations described in Equation (2.23) gives

$$gg = \frac{\mu}{r^3}\begin{bmatrix} 1-3c_1^2 & -3c_1c_2 & -3c_1c_3 \\ -3c_2c_1 & 1-3c_2^2 & -3c_2c_3 \\ -3c_3c_1 & -3c_3c_2 & 1-3c_3^2 \end{bmatrix}\begin{bmatrix} d_x \\ d_y \\ d_z \end{bmatrix} \qquad (3.16)$$

As in Chapter 2, the sum of the non-gravitational perturbations acting upon the surfaces of the spacecraft in the inertial frame is denoted by $\vec{f}_{ng}$. The non-gravitational accelerations a_{ng} is related to $\vec{f}_{ng}$ by

$$a_{ng} = M^{xyz}_{XYZ}\Theta(\vec{f}_{ng}) \qquad (3.17)$$

61

During the COM calibration, it is assumed that the proof mass offset is constant, thus the terms including proof mass offset variations will vanish. Therefore, the true acceleration can be reduced as

$$a_{out} = \dot{\omega} \times d + \omega \times (\omega \times d) + gg + a_{ng} \qquad (3.18)$$

In the above equation, the first term on the right hand side is referred to as the angular acceleration induced disturbance acceleration, denoted by a_{acc}, and the second term is referred to as angular velocity induced disturbance acceleration, denoted by a_{vel}. These two disturbance accelerations are generally called angular motion related acceleration.

Suppose the accelerometer misalignment error angles are $(\theta_1, \theta_2, \theta_3)$, the rotation matrix R_{AB} is of course

$$R_{AB} = \Xi(\theta_1, \theta_2, \theta_3) \qquad (3.19)$$

In the simulation, all three angles are assigned values of 0.1 mrad.

The accelerometer outputs the observation data every 0.1 second. At any accelerometer observation time in the simulations, the real orbit and attitude information $X(t_k) = \begin{bmatrix} \vec{r} & \vec{v} & q & \omega \end{bmatrix}^T$ are available from the true orbit and attitude dynamics propagation. In addition, the modeled non-gravitational acceleration $\vec{f}_{ng}$ and angular acceleration $\dot{\omega}$ are known. Given the tested proof mass offset d, the accelerometer observation data can be simulated using Equations (3.12) through (3.19) (Wang, et al., 2001).

In a typical COM calibration simulation, roll maneuver over the Earth's equator with magnetic torque frequency of 0.1 Hz, the Power Spectrum Density

(PSD) of accelerometer noise A_n, its nominal PSD model and the accelerometer observations are shown in Figure 3.2, from which it can be seen that there is a strong signal in accelerometer observations corresponding to the active torque frequency.
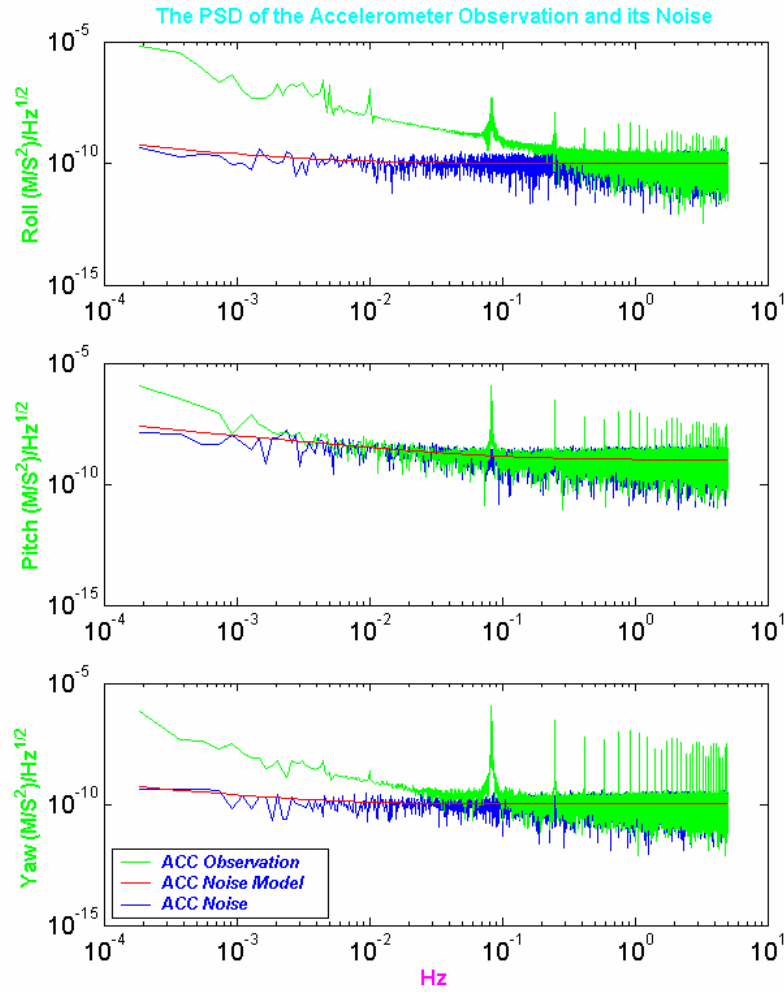
Figure 3.2 PSD of Accelerometer Noise and Observations

3.6 STAR CAMERA INSTRUMENT AND SIMULATION DATA

3.6.1 Instrumentation Design Features

The GRACE Star Camera (SCA) instrument consists of two separate sensor heads and an electronics control and Data Processing Unit (DPU). Each sensor head consists of a optical lens which images a sky portion to a CCD (Charged-Coupled-Device) chip with a $22° \times 16°$ Field Of View (FOV). The sensor head image is integrated for one second, read out, pre-amplified at the sensor head electronics board, and the signals are routed to the DPU, which is responsible for the image observation processing. The on-chip location and, thus, the on-sky projection, of all objects found in the image are determined, the constellation of up to 70 stars are compared with a reference star catalog stored in the DPU and to the best match with the catalog constellation is determined. In essence, the software attempts to identify the measured stars and match the camera picture with a simulated picture using stars from a catalog stored in computer memory. If the match process has been successful, a 3-axis attitude solution can be derived (Fisher, et al., 1989, Junkins, et al., 1977, Strikwerda, et al., 1988). One of the star cameras on board GRACE outputs the observation data very 1 second, while the other one outputs data every 5 seconds. It is required that as the star cameras perform a short integration of the sky image, the satellite movement (rotation about any axis) must not exceed a value of $0.1° / s$ in order to obtain the optimum resolution and accuracy (Grunwaldt, et al., 1996).

The star camera is vital to GRACE. It provides the information to allow accelerometer measurements to be transformed into the inertial frame of reference

and to allow the satellites to be pointed each other. Transforming the accelerometer measurements has the most stringent requirement ~0.3 mrad, with a goal of 0.1 mrad. In addition, because the phase center of the ranging antenna is not collocated with the spacecraft center of mass, range variations due to rotations of the spacecraft about its center of mass must be removed. This correction will be made with a star camera, which is expected to deliver a single-axis accuracy than 0.024 mrad (Davis, et al., 1999).

3.6.2 Star Camera Data Simulation

It is laborious and tedious, even impossible, to simulate the whole procedure performed by the star camera assembly on board the satellite. In order to avoid the strenuous work, but simulate the data close to reality, two simulation approaches are proposed in this research. One is to mimic the simplified internal working mechanism, and the other bypasses this step and just corrupts the quaternion data based on the star camera observation characteristics.

The former approach works in the following way. Based on the true value of the satellite attitude, a group of stars are retrieved from the onboard star catalog. In the real onboard data processing, the measured stars are matched with catalog stars by comparing the angle between each pair of measured stars with the angle between pairs of catalog stars. When a match is found between a measured and catalog pair, a search is made for other catalog stars that lie close to other measured stars when projected. If other matches are found, the probability of an incorrect attitude is essentially zero and the attitude is considered to be uniquely determined. In the simulations, the matching process is ignored and it is assumed

that the match is directly found successfully. Then some position errors are added to the simulated observation data to represent the measurement noises. Finally, an adjustment of the attitude is made using the q-method algorithm (Lerner, 1978) or QUEST algorithm to determine the spacecraft attitude (Shuster, et al., 1981).

In data simulating by this approach, the first step is to generate the observed stars for every observation frame. At each observation data output time, the satellite body-fixed frame can be determined with respect to the inertial space as M_{XYZ}^{xyz} based on the real attitude quaternion q. By multiplying pre-determined fixed rotation matrices R_{BS}^1, R_{BS}^2, rotating from satellite body-fixed system to star camera 1 and 2, and the misalignment error matrices R_{mis}^1, R_{mis}^2, the true star cameras attitude orientations are known. Thus the Boresight Direction (BD) and FOV for each star camera can be determined. Each star with position angles (ϕ_s^r, λ_s^r) in star catalog, corresponding to the unit vector (x_s^r, y_s^r, z_s^r), within the FOV can be transferred into star camera frame by multiplying $R_{mis}^1 R_{BS}^1 M_{XYZ}^{xyz}$ for star camera 1 and $R_{mis}^2 R_{BS}^2 M_{XYZ}^{xyz}$ for star camera 2. The star in star camera frame can be described by new position angles (ϕ_s, λ_s).

The pre-determined rotation matrices R_{BS}^1, R_{BS}^2 are given by

$$R_{BS}^i = \begin{bmatrix} 1 & 0 & 0 \\ 0 & \cos\theta & \sin\theta \\ 0 & -\sin\theta & \cos\theta \end{bmatrix} \qquad \theta = \begin{cases} -135° \ for & i=1 \\ +135° \ for & i=2 \end{cases} \qquad (3.20)$$

where i is the star camera index.

Suppose the star camera misalignment error angles are $(\theta_1, \theta_2, \theta_3)$, the misalignment error rotation matrix R_{mis}^i is given by

66

$$R_{mis}^i = \Xi(\theta_1, \theta_2, \theta_3) \qquad (i = 1,2) \qquad\qquad (3.21)$$

In the simulations, the small angles are taking values of $\pm 0.1 mrad$. By using the sign combinations, it can be avoided that the misalignment errors are possibly cancelled in the simulated KBR range.

The star catalog is a fundamental part of the attitude determination process that contains thousands of stars. A commonly used star catalog is the S*KY 2000 Master Catalog* (Myers, at al., 1997), which was developed at the Goddard Space Flight Center. For many space missions, mission star catalogs were generated as subsets of the S*KY 2000 Master Catalog*, such as XTE Star catalog, SWAS Star Catalog. The recently completed *Hipparcos Star Catalog* contains the most accurate astrometric and photometric star data compared with other star catalogs (ESA, 1997, Bae, 1998). The star catalog stored in the flight computer memory of the GRACE satellites is not available for this research. The Stauffer *Catalog* (Stauffer, 1999), adopted for the ICESAT satellite mission, is used in the simulations described here.

The second step is to add noises to the position angles of each observed star. The Gaussian white noises, with characteristics $(5 arcseconds, 1\sigma)$, are added to the position angles ϕ_s and λ_s to account for the star catalog position error and observation noise. The measured star corrupted with noises in the star camera frame is described by noisy position angles (ϕ_s', λ_s') and corresponding unit position vector (x_s', y_s', z_s').

Finally, the q-method algorithm is used to get the maximum-likehood estimate of attitude quaternions from the measured stars, collections of

(x'_s, y'_s, z'_s), and their reference positions, collections of (x^r_s, y^r_s, z^r_s). Starting with the minimization of the loss function, this algorithm transforms the minimization into an eigenvalue problem of a 4 by 4 matrix where the component of the eigenvector corresponding to the largest eigenvalue is determined as the attitude quaternion.

Basically, an orthogonal matrix A rotating from inertial system to the star camera fixed system is sought which satisfies

$$A\hat{V}_{i,k} = \hat{W}_{i,k} \qquad (i = 1,2...n_k) \qquad (3.22)$$

where $\hat{V}_{1,k},...\hat{V}_{n_k,k}$ are a set of reference unit vectors, which are n_k known directions in the reference coordinate system, and $\hat{W}_{1,k},...\hat{W}_{n_k,k}$ are the observation unit vectors, which are the same n_k directions as measured in the star camera fixed coordinate system, k is the time index.

To take advantage of multiple unit vectors simultaneously obtained by a CCD frame, a least square attitude problem was suggested in the early 1960's by Wahba (Wahba, 1996). Instead of solving Equation (3.22), it is to find an orthogonal matrix A_{opt} that minimizes the loss function

$$L(A) = \frac{1}{2} a_i \sum_{i=1}^{n_k} \left| \hat{W}_{i,k} - A\hat{V}_{i,k} \right|^2 \qquad (3.23)$$

where

$$\sum_{i=1}^{n_k} a_i = 1 \qquad (3.24)$$

68

The optimal estimate $\hat{q}^{obs}$ that minimizes the loss function (3.23) is given by q-method algorithm as follows

$$K\hat{q}^{obs} = \lambda_{max}\hat{q}^{obs} \tag{3.25}$$

where λ_{max} is the maximum eigenvalue of K, and the 4 by 4 matrix K is given by

$$K = \begin{bmatrix} S - \sigma I & Z \\ Z^T & \sigma \end{bmatrix} \tag{3.26}$$

where

$$\sigma = \sum_{i=1}^{n_k} \hat{W}_{i,k} \cdot \hat{V}_{i,k} \tag{3.27}$$

$$S = \sum_{i=1}^{n_k} (\hat{W}_{i,k}\hat{V}_{i,k}^T + \hat{V}_{i,k}\hat{W}_{i,k}^T) \tag{3.28}$$

$$Z = \sum_{i=1}^{n_k} a_i (\hat{W}_{i,k} \times \hat{V}_{i,k}) \tag{3.29}$$

Let δq be the quaternion of the small rotation that takes the true quaternion into the optimal quaternion calculated by Equation (3.25). δq is assumed to be unbiased, thus

$$E(\delta q) = E\begin{pmatrix} \delta Q \\ \delta \zeta \end{pmatrix} = \begin{bmatrix} 0_{3\times1} \\ 1 \end{bmatrix} \tag{3.30}$$

By this definition, the covariance of the quaternion estimate is defined as

$$P_{QQ} = E(\delta Q \delta Q^T) \tag{3.31}$$

69

Furthermore, it can be expanded as

$$P_{QQ} = \frac{1}{4}\sigma_{tot}^2[I - \sum_{i=1}^{n_k}\hat{W}_{i,k}\hat{W}_{i,k}^T]^{-1} \qquad (3.32)$$

where

$$(\sigma_{tot}^2)^{-1} = \sum_{i=1}^{n_k}(\sigma_{i,k}^2)^{-1} \qquad (3.33)$$

where $\sigma_{i,k}^2$ is the sum of covariance of measurement and reference unit vector at time t_k.

The other simulation approach is much simpler. It just corrupts the quaternion data based on the attitude measurement error model. The characteristics of the GRACE star camera are the 1σ value of $80\mu rad$ for the single axis accuracy at orbital rate relative to BD and $240\mu rad$ for the BD axis. The $\hat{z}$ axis of the star camera frame is parallel to BD direction.

Using the same notations as above, the simulated observed quaternion $\hat{q}_i^{obs}$ of each star camera by this approach is given by

$$\Re(\hat{q}_i^{obs}) = R_n R_{mis}^i R_{BS}^i \Re(q) \qquad (i=1,2) \qquad (3.34)$$

where $R_n = \Xi(\theta_1,\theta_2,\theta_3)$, and θ_3 is white noise with 1σ value of $240\mu rad$, θ_1 and θ_2 are white noises with 1σ value of $80\mu rad$.

The observed quaternion can be easily transferred back to the satellite body-fixed frame as

$$\Re(q_i^{obs}) = (R_{BS}^i)^T \Re(\hat{q}_i^{obs}) \qquad (3.35)$$

70

In the simulations, both approaches are tried. They yield almost the same level of calibration accuracy.

3.7 MAGNETOMETER INSTRUMENT AND SIMULATION DATA

3.7.1 Instrumentation Design Features

The Magnetometer (MAG) is one of the sensors utilized in the satellite's AOCS. With its three sensor axes orthogonal aligned, it senses the Earth's magnetic field in direction and amplitude at any current orbit position (Rieger, et al., 1996).

During the nominal mission phase, the prime purpose of the magnetometer is to allow the AOCS to adjust the three magnetic torque rod currents according to the attitude control needs. Additionally, from the variation of the magnetic field vector over the orbit and the knowledge on the orbit position, it allows the AOCS to determine the rate about an arbitrary momentary axis-of-rotation. However, during the center mass calibration and K-band ranging system calibration with a linearly drifting maneuver, the magnetometer provides the information of the Earth's magnetic field. Normally, the magnetometer outputs the observation data very 10 seconds, but it can output every 1 second when commanded.

The magnetometer hardware consists of a sensor head containing a three axes sensing assembly including pertinent coils, and pertinent electronics. Axes alignment accuracy of the magnetometer instrument is comprised by four parts. First, the angle between the magnetometer z-axis and the true normal axis of the mounting plane will not exceed 0.75 degree. Second, the angle between the mounting planes' normal vector and the ideal normal vector, which is given by

the boom's axis, will not exceed 1 degree. This value includes thermo-elastic stability, boom elastics (if any) and boom manufacturing and mounting tolerances. Third, the angle between each of the three sense axes of the magnetometer head will not exceed 0.75 degree relative to corresponding axis of the ideal sense axes' tripod. Finally, the deployment inaccuracy will not exceed 1 degree (GRACE Team, 1999d). In the worst case, all errors add up linearly.

The magnetic field sensing characteristics of the magnetometer are listed in Table 3.3.

Table 3.3   Characteristics of the Magnetometer

MEASUREMENT CHARACTERISTICS	
Measurement axes:	3 orthogonal axes
Measuring Range, each axis:	-50 micro Tesla to +50 micro Tesla
Resolution:	25 nano Tesla
Measurement Bandwidth:	$4.5\,Hz \pm 1\,Hz$
MAXIMUM MEASUREMENT DISTURBANCES (INDEPENDENT)	
Bias error	100 nano Tesla
Linearity error	25 nano Tesla
Noise	3 nano Tesla

3.7.2 Magnetometer Data Simulation

Given the real position of the satellite from orbit and attitude propagation, the geocentric distance, coelevation, and east longitude of the satellite r, θ, ϕ can be easily known. By Equation (2.27), the Earth's magnetic flux density component along vertically upward, local south direction, and local east direction B_r, B_θ, B_ϕ can be obtained. Furthermore, the magnetic flux density B expressed

in satellite body-fixed system can be obtained by Equation (2.29). After all, at any magnetometer observation time, the observed magnetic flux density $\overline{B}$ can be modeled as follows

$$\overline{B} = R_{mis}(B + bias\_B + noise\_B) \qquad (3.36)$$

where R_{mis} is the misalignment error matrix, $bias\_B$ is the measurement bias, and $noise\_B$ is gaussian measurement noise. These values are specified in Section 3.7.1.

3.8 KBR INSTRUMENT AND SIMULATION DATA

3.8.1 Instrumentation Design Features

To achieve $10\mu m$ precision, a laser system is usually the first candidate. While a laser system was considered, the range signals due to geoid variation are in a very low frequency range, below 0.05 Hz. In 1996, the technology to stabilize a laser's frequency at these long time scales had not been demonstrated. On the other hand, UltraStable Oscillators (USO) suitable for the GRACE mission were well developed and space qualified. Because the microwave wavelength is much longer than a laser wavelength, the phase of the signal must be stabilized to one part in 10,000. This technology is also available and qualified for space. To minimize the cost of the mission, a microwave system was selected to perform the ranging measurements.

The K-band ranging system can output the observation data every 0.1 second. It measures changes in distance between the GRACE satellites by exchanging linearly polarized K- and Ka-band carrier signals between the

satellites. The transmissions of the satellites differ in frequency by 20 ppm and propagate with perpendicular polarization directions. At each spacecraft, the transmit and receive signals are mixed to produce a quadrature baseband signal. The average of the phase change measured by each satellite results in a biased range measurement for which the clock noise is reduced by a high-pass filter with a 1 kHz cutoff frequency. Because the gravitational signal of interest lies below 0.05 Hz, this results in a tremendous improvement as compared to a one-way phase measurement. The use of simple digital filters results in a reduction of 3×10^{-54}.

The phase of the base-band signal is extracted digitally by the IPU (Instrument Processing Unit). Transmit power and antenna aperture have been selected to produce a carrier-to-noise ratio and resulting one-sigma carrier phase precision of below $1 \mu m$.

The major error source affecting the range observable is the variations of the measured phase with the change in temperature of the components. This has been addressed by controlling the temperature of the KBR to 0.2 K, minimizing the length of waveguide runs, and selecting components with small thermal coefficients. In the unlikely event the thermal control of the satellite is worse than 0.2 K, temperature measurements will allow the range to be corrected to about 10%. Another error source is multipath. If the geometry between the transmitter and receiver change, multipath will introduce a variable range offset which is difficult to calibrate. This error source has been dealt with by setting spacecraft

pointing requirements to keep the variable multipath error negligible (Davis, et al., 1999).

3.8.2 KBR Data Simulation

The GRACE mission uses the dual one-way K-band ranging system for precise inter-satellite phase measurements. Each satellite transmits K/Ka band microwave signals to the other satellite and receives that satellite's signals. Combination of the received signal and the reference signal, equivalent to the transmit signal, generates a phase measurement. The KBR system has four observation variables, K-band phase measurement at GRACE A, Ka-band phase measurement at GRACE A, K-band phase measurement at GRACE B and Ka-band phase measurement at GRACE B. These phase measurements are transmitted to the ground station for post-processing, which combines the four kinds of phase data to yield the low-low range observable.

The post-processing procedure of the dual one-way range measurement and the dual one-way ranging formulations from phase data can be found in Chapter 2 of Jeong-Rae Kim's dissertation (Kim, 2000). Instead of simulating the phase data and implementing post-processing algorithms to yield range data, the range and range rate data are simulated directly in this study in an equivalent way.

As shown in Figure 2.1, the position vectors of two K-band horn phase centers, $\vec{R}_1, \vec{R}_2$, in the inertial system can be formulated as

$$\Theta(\vec{R}_1) = \Theta(\vec{r}_1) + M_1 \Theta(\vec{d}_{pc1}) \qquad (3.37)$$

$$\Theta(\vec{R}_2) = \Theta(\vec{r}_2) + M_2 \Theta(\vec{d}_{pc2}) \qquad (3.38)$$

where M_1, M_2 are the rotation matrices from satellite body fixed system to inertial system, and $\vec{d}_{pc1}, \vec{d}_{pc2}$ are the position vectors of K-band horn phase centers in the satellite body fixed systems.

Thus

$$M_1 = \Re(q_1)^T \tag{3.39}$$
$$M_2 = \Re(q_2)^T \tag{3.40}$$

Then the biased range derived from K-band ranging system can be modeled as

$$R = \left| \vec{R}_1 - \vec{R}_2 \right| + R_{br} + R_{nr} \tag{3.41}$$

where R_{br}, R_{nr} are the range bias and range noise, respectively.

And the range rate, the time derivative of range, becomes

$$RR = \frac{(\vec{R}_1 - \vec{R}_2) \cdot (\dot{\vec{R}}_1 - \dot{\vec{R}}_2)}{\left| \vec{R}_1 - \vec{R}_2 \right|} + RR_n \tag{3.42}$$

where

$$\Theta(\dot{\vec{R}}_1) = \Theta(\dot{\vec{r}}_1) + M_1 \Theta(\omega_1 \times \vec{d}_{pc1}) \tag{3.43}$$
$$\Theta(\dot{\vec{R}}_2) = \Theta(\dot{\vec{r}}_2) + M_1 \Theta(\omega_2 \times \vec{d}_{pc2}) \tag{3.44}$$

where $\dot{\vec{r}}_1, \dot{\vec{r}}_2$ are the velocity vectors of the COMs of the spacecraft, and ω_1, ω_2 are the angular velocities of the spacecraft (Wang, et al., 2002a).

The K-band ranging system measurement noises, R_{br}, include oscillator noise, system noise and the multipath noise. Kim has made simulations of these noises. The detail formulations can be found in (Kim, 2000) and only brief introductions of these noises are presented below.

The GRACE satellite uses USO to generate the base frequency of the K/Ka band signals. The instability of USO results in frequency shifting from nominal frequency, which appears in the ionosphere-free range observation as oscillator noise. The major factors that affect the oscillator noise include microwave frequency, frequency offset and the time-of-flight. Certain values for these parameters are used to produce a pessimistic noise level in the simulations. For example, a larger frequency offset causes less efficient dual one-way filtering, and a higher altitude or larger separation angle implies a longer separation distance and longer time-of-flight, which causes less oscillator drift cancellation. Between K and Ka band frequency, K band, $f = 24GHz$, with frequency offset $\Delta f = 1.5MHz$ was chosen to get a feasible highest noise level (Kim, 2000).

The other major noise is system noise, which comes from the receiver subsystem. It can be approximated as white noise for the range measurement. Its magnitude depends on the distance between two GRACE satellites, and the nominal value is the PSD of $1(\mu m / \sqrt{Hz})^2$ at 230 km separation. This is the value after a dual-band calibration to remove the ionosphere effect with the SNR (Signal-to-Noise Ratio) of 69 dB-Hz (Thomas, 1999).

One sampled oscillator noise and system noise used in the KBR calibration simulation are shown in Figure 3.3.
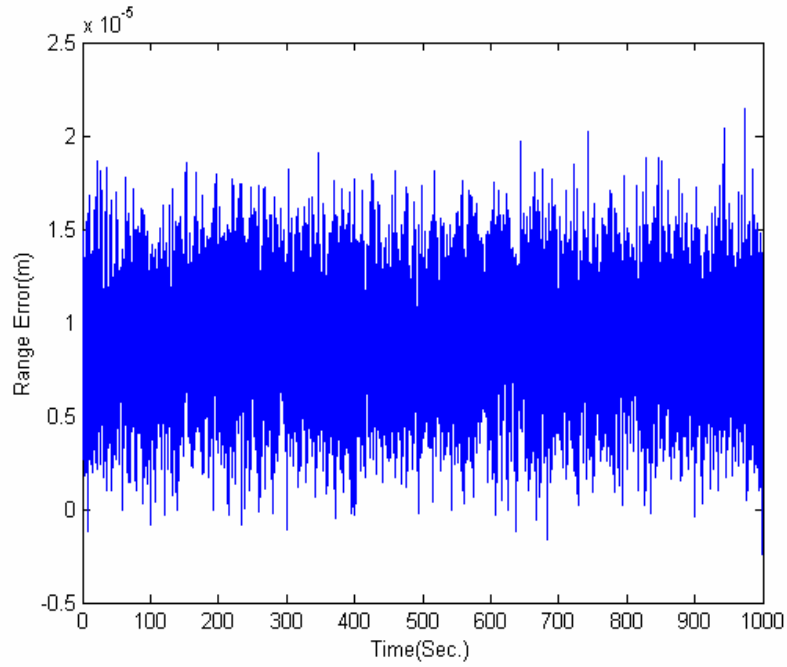
Figure 3.3 System and Oscillator Noise

The multipath noise is due to the indirect microwave signals that are reflected around antenna horn. The noise level depends on the reflectivity of front surface of the satellite and the satellite attitude. This error is pretty large during the K-band ranging system calibration since the cone angle is much larger than in the nominal phase.

One simple model of multipath error in the simulations is given as follows

$$\Delta R = \mu|\theta| \tag{3.45}$$

where μ is a constant taking value of 3 mm/rad and θ is the yaw or pitch angle deviation described in Section 3.3 (Kim, 2000).

The range observations can be obtained from Equation (3.41) once the real positions of spacecraft and tested phase centers are specified. The range noise R_{nr} is the sum of all noises stated above. There are two ways to simulate the range rate. One is by differentiating R_{nr} to get RR_n and obtain the range rate according to Equation (3.42). The other is by digital–filtering the range observation R to derive the range rate. It is the later approach that is adopted in the real data processing. Complete investigation of this topic can be found in (Thomas, 1999). In this study, the later approach to simulate the range rate is used.

The Finite Impulse Response (FIR) digital filters have been developed by Thomas (Thomas, 1999) for extracting range, range rate and acceleration from the dual one-way range values by simultaneously applying a low-pass filter, reducing the data rate, and, for range rate and acceleration, applying the appropriate differentiation. The digital filters should differentiate to the desired order and have a nearly rectangular response in the frequency domain with an appropriate low-pass cutoff. To avoid aliasing out-of-band noise into the signal band, the low-pass cutoff is set approximately equal to the Nyquist value. The frequency response must have sufficiently small sidelobes and cause amplitude distortion across the signal band at a level that satisfies the project goal of 0.01 cmG per degree for gravity coefficients. As is well known, such a filter can be theoretically generated by convolving a signal with a sinx/x function in the time domain. The CRN class of FIR digital filters is used to filter the KBR range observations.

There will be detail discussions of the CRN filter in the Appendix A. At this moment, one can just assume that after setting certain parameters, the filter

can smooth and differentiate time-series data with designed features. Let us denote the smoothing operator as $CRN()$ and first order differentiation operator as $CRN'()$, then the range rate can be obtained by CRN filtering the range observation as

$$RR = CRN'(R) \tag{3.46}$$

For second order differentiation, the operator $CRN''()$ is used in this study.

3.9 POD BY GPS AND SIMULATION DATA

The GPS receiver assembly serves for precise orbit determination (cm-accuracy) with continuous coverage of the orbit, and ionospheric electron content and atmospheric density, pressure and temperature sounding. To achieve these goals, satellite-to-satellite tracking between GRACE satellite and the high-altitude orbiting GPS spacecraft is performed.

The receiver assembly consists of four omni-directional antennas and TRSR-2 receiver. The system can simultaneously track up to 12 GPS satellites and derive the on-board navigation solution, and collect the tracking data for on-ground precise orbit determination. The receiver performs phase measurements of both GPS carrier frequencies L1 and L2, and derives pseudorange mesurements from L1 and L2 measurements. The output of the GPS receiver system is the complete navigation solution, in addition to the phases and pseudoranges from the GPS satellites tracked. Additionally, the aft antennas allow to derive ionospheric and atmospheric parameters. Knowing the positions of GRACE and the GPS

satellites, the measurement of the retardation of the carrier phases of L1 and l2 allows the determination of the propagation delays caused by the ionosphere and atmosphere.

The range and range rate observable of KBR system include relative orbit, instead of absolute orbit of spacecraft. The relative position and velocity of GRACE satellites, $\vec{r}_{12}$ and $\dot{\vec{r}}_{12}$, can be modeled as follows

$$\vec{r}_{12} = \vec{r}_1 - \vec{r}_2 + \vec{r}_{12n} \tag{3.47}$$
$$\dot{\vec{r}}_{12} = \dot{\vec{r}}_1 - \dot{\vec{r}}_2 + \dot{\vec{r}}_{12n} \tag{3.48}$$

where $\vec{r}_{12n}$ and $\dot{\vec{r}}_{12n}$ are relative position and velocity errors of the two GRACE satellites.

The program MSODP can provide precise orbit determination from GPS phase measurements. A complete simulation made Kang (Kang, 2001) has generated a time series of the relative position error and relative velocity error using the tool of MSODP. Various measurement model errors are included in his simulation of GRACE orbit determinations. A one day simulation is carried out. Based on the true orbits and determined orbits of GRACE satellites, the relative position determination error and relative velocity determination error can be derived. Sampled relative position errors are shown in Figure 3.4, from which it can be seen that these errors may be well filtered by polynomial functions in the calibration period.
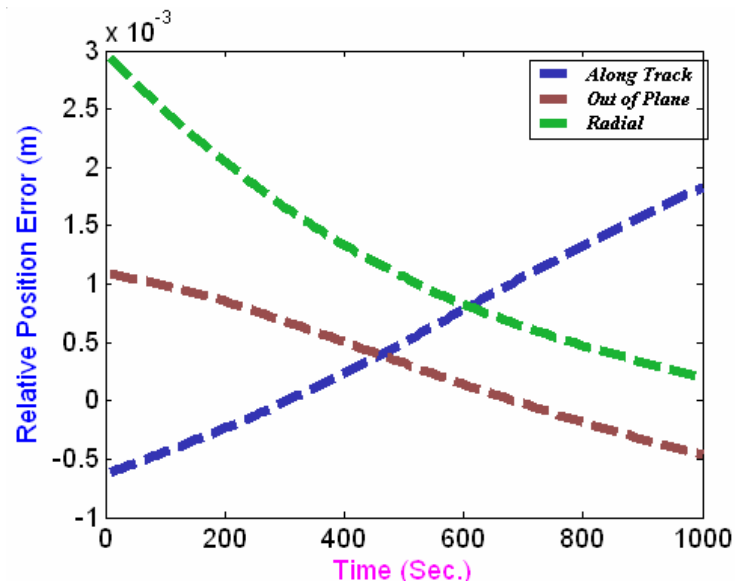
Figure 3.4 Relative Position Error Model

So far, the maneuvers for the COM and KBR calibration are designed. The behavior of the attitude motion track and the activation approach of the active torque are described. In addition, the performance characteristics of the measurement instruments of these two calibrations are presented and their measurement models are established. These models will be used in both data simulation and data processing.

82

Chapter 4: Calibration Estimation Algorithms

4.1 INTRODUCTION

Based on the descriptions in the previous chapters, simulation data of the center of mass calibration and K-band ranging system calibration can be generated. In this chapter, various estimation algorithms for processing the simulation data have been proposed. In fact, these algorithms have already been applied to process real calibration data and generated good results.

Since the data frequency and observation frame of the instruments are different, preprocessing needs to be done before the estimation algorithms are applied. The preprocessing algorithms to process the attitude quaternion data and magnetometer data are developed.

The minimum variance batch processor for the general non-linear system is reviewed. Based on this general estimation theory, the estimation algorithms for both calibrations are proposed in detail.

In addition, the covariance analysis for center of mass calibration is performed, from which the optimal calibration timing criterion is set. This criterion has a theoretical guidance for realizing the real calibration maneuver. The noise analysis for the K-band ranging system is also carried out. This analysis is quite helpful in determining the effects of various noises, which affect the calibration accuracy. It is also useful in the real calibration design and data analysis.

Given the estimated phase centers and the attitude observations, the KBR range observable can be corrected with the presence of misalignment of COMs and phase centers. The derivation is presented in detail, along with the formulation of star camera misalignment.

4.2 ESTIMATION ALGORITHMS FOR COM CALIBRATION

As described in the previous chapter, the GRACE onboard instruments, accelerometer, star camera and magnetometer, provide all the necessary observables for calibration of the center of mass offset. The accelerometer's observations directly reflect the proof mass offset. The observations of the star camera and the magnetometer provide an accurate attitude dynamic model and therefore the angular motion information can be determined. The ultimate goal of this calibration is to reduce the proof mass offset and make the accelerometer observations quantify the surface force accelerations acting on the satellite.

During the center of mass calibration, a periodic magnetic torque is applied to the satellite. This periodic torque creates the same periodic pattern for the angular velocity and angular acceleration. The non-gravitational accelerations, also called surface accelerations, are totally dependent upon the orbit environment and the satellite's orientation and, of course, the physical property of the surface of the satellite. The orbit environment and the physical property of the surface will not change much in the short calibration time span. Further, the attitude of the satellite is not sensitive to the periodic and relatively small torque and the satellite is approximately in its nominal attitude. Therefore, the non-gravitational accelerations are smooth compared to the more rapid frequency of the angular

velocity and angular acceleration and can be fitted by linear terms. This important point is used in developing the estimation algorithms later.

There will be three different estimation algorithms proposed. Starting from the observation data preprocessing, estimation theory, dynamic fitting model and observation fitting model, the estimation algorithms for center of mass calibration will be investigated thoroughly in this section.

4.2.1 Observation Data Preprocessing

The star cameras output the attitude quaternions of the star camera frames relative to the inertial space. The quaternion observation can uniquely determine the attitude orientation of the star camera. However, for a given attitude orientation, the attitude quaternion cannot be uniquely determined, due to an ambiguity in the sign difference. An interesting problem comes from the q-method algorithm when the quaternion is derived from the observed stars. This algorithm can result in the sign reversal of all quaternion components, when q_4 is close to zero. This problem can be overcome by forcing the largest magnitude component of the quaternion to be the same sign as this component's last value. Of course, the attitude observation data should be transformed to describe the satellite body-fixed system relative to the inertial system. In case the star-camera observation quaternion data are not unit vectors, they need to be normalized. Additionally, due to the different data output frequency of the instruments, the observation data from some of instruments should be interpolated. All of this work must be done during data preprocessing.

In this study, the quaternion data are chosen from the star camera with a 1 Hz data output frequency. Given a set of star camera's quaternion observation data $\{\hat{q}^{obs}(t_1), \hat{q}^{obs}(t_2), ... \hat{q}^{obs}(t_m)\}$, the following steps must be performed before performing the proof mass offset estimation.

The first thing to do is to transform the quaternion data to determine the satellite body-fixed system relative to the inertial system.

For quaternion observation $\hat{q}^{obs}(t_k)$ at time t_k, given the pre-determined rotation matrix R_{BS} from satellite body-fixed system to the star camera frame, the rotation matrix M, which describes the transformation from the inertial system to the satellite body-fixed system, can be obtained as

$$M = R_{BS}^{-1} \Re(\hat{q}^{obs}(t_k)) \tag{4.1}$$

The four-component quaternion, subject to $q_4 \geq 0$, can be obtained from rotation matrix M in the following way (Hughes, 1986)

$$\bar{q}_4 = \frac{1}{2}\sqrt{1 + Trace(M)} \tag{4.2}$$

$$\begin{bmatrix} \bar{q}_1 \\ \bar{q}_2 \\ \bar{q}_3 \end{bmatrix} = \frac{1}{4\bar{q}_4} \begin{bmatrix} M(2,3) - M(3,2) \\ M(3,1) - M(1,3) \\ M(1,2) - M(2,1) \end{bmatrix} \quad , \bar{q}_4 \neq 0 \tag{4.3}$$

and

$$\begin{bmatrix} \bar{q}_1 \\ \bar{q}_2 \\ \bar{q}_3 \end{bmatrix} = \begin{bmatrix} \sqrt{1 + M(1,1)}/\sqrt{2} \\ \sqrt{1 + M(2,2)}/\sqrt{2} \\ \sqrt{1 + M(3,3)}/\sqrt{2} \end{bmatrix} \quad , \bar{q}_4 = 0 \tag{4.4}$$

where *Trace*() in Equation (4.2) is the trace of the matrix. Later, the process to determine the quaternion q from any matrix M is denoted by operator $\tilde{\Re}()$ as $q = \tilde{\Re}(M)$ in the above formulations. The operator $\tilde{\Re}()$ is an inverse operator of $\Re()$.

Then it is necessary to check the sign polarity of the quaternion data $\{\bar{q}(t_1), \bar{q}(t_2), ... \bar{q}(t_m)\}$ and normalized if necessary. The restriction of $q_4 \geq 0$ cannot solve the sign ambiguity problem, since it is addressed by the largest magnitude component of quaternion and q_4 is not necessarily this component. If the sign flip does happen, the sign of all four components of the quaternion must be changed at that observation time. In fact this happens only $q_4 \approx 0$. When q_4 is large, there is no need to check the sign flip for the observed quaternion. After the sign ambiguity check, the quaternion data at any time t_k can be normalized by

$$q'(t_k) = \bar{q}(t_k) / \sqrt{\bar{q}_1^2(t_k) + \bar{q}_2^2(t_k) + \bar{q}_3^2(t_k) + \bar{q}_4^2(t_k)} \qquad (4.5)$$

As mentioned before, the star camera outputs observation data every one second, and the magnetometer outputs the Earth's magnetic field data every 10 seconds, while the accelerometer outputs observed acceleration data every 0.1 second. In this study, the star camera and magnetometer data are interpolated to construct derived data with 10 Hz frequency, which is consistent with that of the accelerometer observation data. A simple linear interpolator is applied to the quaternion and magnetometer data using the procedure illustrated below.

Suppose that the observation data rate is N_o/sec, and the interpolated data rate is N_i/sec, given the observation data y_{t_1} at time t_1 and y_{t_2} at time t_2, the interpolated data y_t at time t between t_1 and t_2 can be obtained as

$$y_t = y_{t_1} + k(t - t_1) \qquad (4.6)$$

where the slope k is given by

$$k = \frac{y_{t_2} - y_{t_1}}{t_2 - t_1} \qquad (4.7)$$

Of courses, t is evenly distributed between t_1 and t_2 with interpolated data rate N_i/sec.

Again, it may be necessary to normalize the quaternion data at any time t_k to construct the final preprocessed data

$$q_{obs}(t_k) = \overline{q}'(t_k) / \sqrt{\overline{q}_1'^2(t_k) + \overline{q}_2'^2(t_k) + \overline{q}_3'^2(t_k) + \overline{q}_4'^2(t_k)} \qquad (4.8)$$

So far, the observation data are preprocessed to be of the same data rate and ready for use.

4.2.2 Batch Estimation Theory

Before the estimation algorithms are proposed, the computational algorithm for the minimum variance batch processor for the general non-linear system and consider covariance analysis of the linear system deserve some reviews (Bettadpur, 1998, Junkins, 1978).

Without loss of generality, the dynamic model and the observation model are all assumed to be non-linear equations. The dynamic model is described by

$$\dot{X}(t) = F(X,t) \qquad (4.9)$$

And the observation model is represented by

$$Y(t) = G(X(t),t) + \varepsilon(t) \qquad (4.10)$$

where $\varepsilon(t)$ is observation white noise with characteristics of mean $E(\varepsilon) = 0$ and covariance $E(\varepsilon\varepsilon^T) = R$.

Given the initial guess of the dynamic model state, $X^*(t_0)$, the nonlinear dynamic model can be integrated to generate the nominal state trajectory $X^*(t)$ at any time t. The difference of the real state and the nominal trajectory state can be defined as the state residual, denoted by $x(t) = X(t) - X^*(t)$, which can be related to the state transition matrix $\Phi(t,t_0)$ as follows

$$x(t) = \Phi(t,t_0)x(t_0) \qquad (4.11)$$

where $x(t_0)$ is the state residual at initial epoch t_0, which obviously is unknown and is the estimate for the estimation system. And the state transition matrix satisfies

$$\dot{\Phi}(t,t_0) = A(t)\Phi(t,t_0) \qquad (4.12)$$

where the matrix $A(t)$ is the partial derivative of $F(X,t)$ evaluated on the nominal trajectory. It is given by

89

$$A(t) = \frac{\partial F(X(t),t)}{\partial X(t)}\bigg|_{X(t)=X^*(t)} \qquad (4.13)$$

The state transition matrix $\Phi(t,t_0)$ at any time t can be obtained by integrating Equations (4.9) and (4.12), using (4.13), with the initial values of $X^*(t_0)$ and $\Phi(t_0,t_0) = I$.

On the observation side, the difference between the real observation and the expected observation defined by the nominal trajectory state at time t is defined as the observation residual $y(t)$, explicitly, $y(t) = Y(t) - G(X^*(t),t)$. The observation residual can be related to the state residual by an observation-state mapping matrix $\tilde{H}(t)$ as follows

$$y(t) = \tilde{H}(t)x(t) \qquad (4.14)$$

where the observation-state mapping matrix is given by

$$\tilde{H}(t) = \frac{\partial G(X(t),t)}{\partial X(t)}\bigg|_{X(t)=X^*(t)} \qquad (4.15)$$

Thus, at any observation time t_k, the observation model can be reduced to linear equation as

$$y(t_k) = \tilde{H}(t_k)\Phi(t_k,t_0)x(t_0) + \varepsilon(t_k) \qquad (4.16)$$

Or

$$y(t_k) = H(t_k)x(t_0) + \varepsilon(t_k) \qquad (4.17)$$

All the observations can be combined into a m-dimensional observation vector as

$$\begin{bmatrix} y(t_1) \\ y(t_2) \\ \vdots \\ y(t_m) \end{bmatrix} = \begin{bmatrix} H(t_1) \\ H(t_2) \\ \vdots \\ H(t_m) \end{bmatrix} x(t_0) + \begin{bmatrix} \varepsilon(t_1) \\ \varepsilon(t_2) \\ \vdots \\ \varepsilon(t_m) \end{bmatrix} \qquad (4.18)$$

Or

$$y = Hx(t_0) + \varepsilon \qquad (4.19)$$

The minimum variance estimate for the above system is (Bettadpur, 1998)

$$\hat{x}(t_0) = (H^T R^{-1} H)^{-1} (H^T R^{-1} y) \qquad (4.20)$$

The covariance matrix of the minimum variance estimate $\hat{x}(t_0)$ is given by

$$\hat{P}(t_0) = (H^T R^{-1} H)^{-1} \qquad (4.21)$$

Finally, the initial estimate of the system state $X^*(t_0)$ can be updated by adding the estimate $\hat{x}(t_0)$ to the original guess and the whole process can be iterated until it converges.

The flow chart for the batch processor computational algorithm is shown in Figure 4.1.
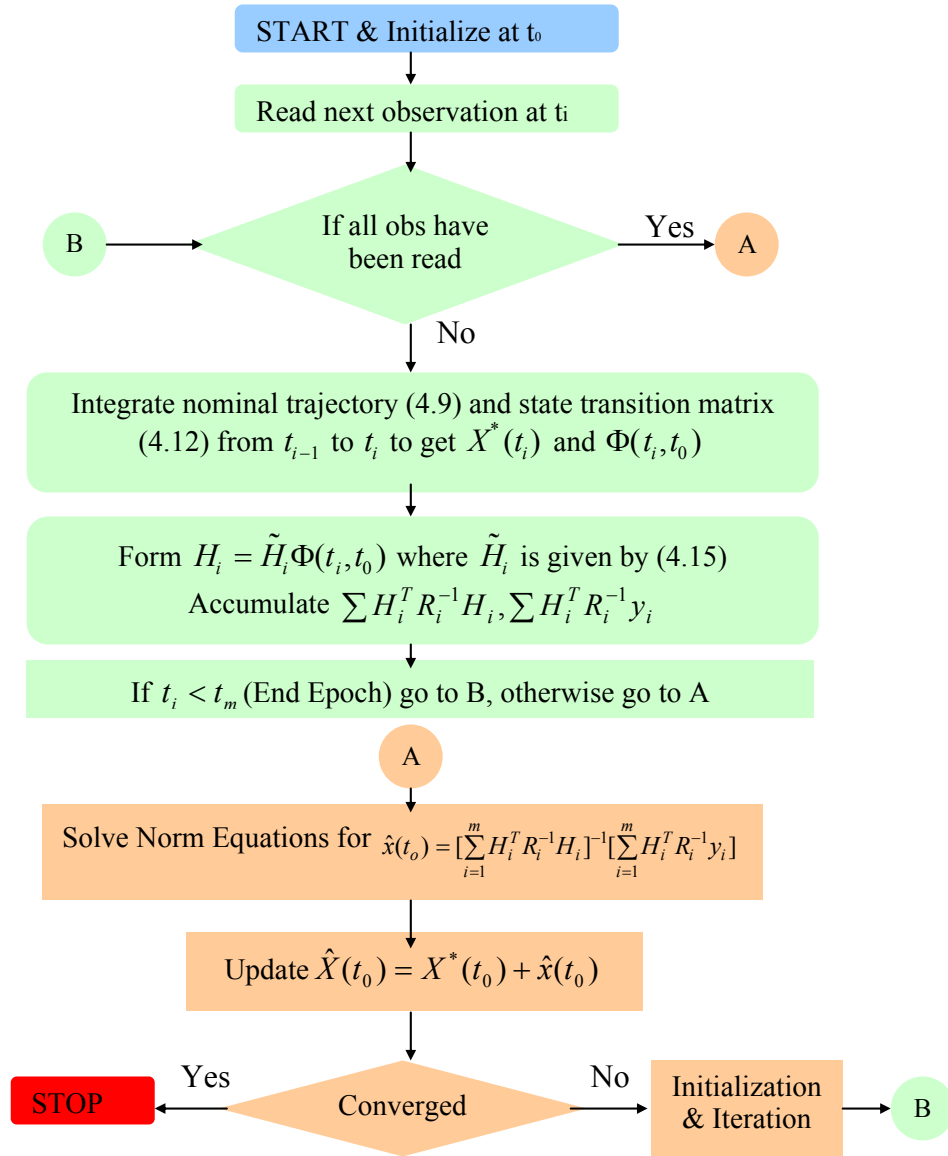
Figure 4.1 Flow Chart of Batch Processor Algorithm

92

Besides the batch processor, the consider covariance analysis needs to be reviewed for later use (Bettadpur, 1998).

Suppose a linearized observation model is given by

$$y = H_x x + H_c c + \varepsilon \tag{4.22}$$

where $\varepsilon(t)$ is observation noise with characteristics of mean $E(\varepsilon) = 0$ and covariance $E(\varepsilon\varepsilon^T) = R$, x is the estimated parameter, c is consider parameter with characteristics of $E(c) = 0$ and covariance $E(cc^T) = P_c$.

The estimate of x can be obtained as

$$\hat{x} = (H_x^T R^{-1} H_x)^{-1}(H_x^T R^{-1} y) + Sc \tag{4.23}$$

where S is the sensitivity matrix of the consider parameter to the estimate, and it is given by

$$S = -(H_x^T R^{-1} H_x)^{-1}(H_x^T R^{-1} H_c) \tag{4.24}$$

and the covariance of $\hat{x}$ is obtained

$$\hat{P} = (H_x^T R^{-1} H_x)^{-1} + S P_c S^T \tag{4.25}$$

4.2.3 Dynamic Fitting Model and Partial Derivatives

The dynamic fitting model for center of mass calibration is composed of the attitude dynamic equations of motion and attitude kinematic equations of motion. Since the disturbance environmental torques are dominated by the active magnetic torque, they are neglected in the attitude dynamic fitting model, although they appear in the real attitude propagation. Therefore, the attitude

dynamic equations of motion described by Equation (2.16) can be simplified as follows

$$\frac{d\omega}{dt} = J^{-1}(m_m \times B - \omega \times (J\omega))$$ (4.26)

The moment of inertia tensor J is with respect to the center of mass of the spacecraft. During the lifetime of the GRACE mission, the moment of inertia tensor, J_p, with respect to SF is updated from cold gas consumption analysis (Kruizinga, 2003). By Huygens-Steiner parallel axes theorem (Hughes,1986), J , can be decomposed into two parts, one is the moment of inertia tensor J_p relative to the proof mass of the accelerometer, and the other part is contributed by the proof mass offset. Thus

$$J = J_p + \Delta J$$ (4.27)

$$\Delta J = -m_S \begin{bmatrix} d_y^2 + d_z^2 & -d_x d_y & -d_x d_z \\ -d_x d_y & d_x^2 + d_z^2 & -d_y d_z \\ -d_x d_z & -d_y d_z & d_x^2 + d_y^2 \end{bmatrix}$$ (4.28)

The inverse of the moment of inertia tensor J becomes

$$\begin{aligned} J^{-1} &= (J_p + \Delta J)^{-1} \\ &= (J_p + \Delta J)^{-1}(J_p^{-1})^{-1}J_p^{-1} \\ &= (I + J_p^{-1}\Delta J)^{-1}J_p^{-1} \end{aligned}$$ (4.29)

In fact, this inversion could be simplified, since J_p^{-1} is very small, i.e., on the order of $10^{-3}\,Kg^{-1} \cdot m^{-2}$, and the 2-norm of $J_p^{-1}\Delta J$ is less than 1, which satisfy the condition for the Neuman series (Greenberg, 1978).

94

Neuman Series: If M is linear and its 2-norm $|M|_2 < 1$, then
$(I + M)^{-1} = I - M + M^2 - \dots$

By this theory, the inverse of the moment of inertia tensor can be expanded and simplified as

$$J^{-1} = J_p^{-1} - J_p^{-1} \Delta J J_p^{-1} + \dots$$
$$\approx J_p^{-1} \tag{4.30}$$

In addition, since $J_p \gg \Delta J$, the attitude dynamic equations of motion can be further simplified as

$$\frac{d\omega}{dt} = F_1 = J_p^{-1}(m_m \times B - \omega \times (J_p \omega)) \tag{4.31}$$

The attitude kinematic equations of motion used in the observation fitting model are the same as Equation (2.20), rewritten as follows

$$\dot{q}(t) = F_2 = \frac{1}{2}\Omega(\omega)q(t) \tag{4.32}$$

where $\Omega(\omega)$ is given by Equation (2.21).

The partial derivatives are required to linearize the fitting dynamic model. Carrying out the partial derivatives of Equations (4.31) and (4.32) about $q(t), \omega(t)$ yields

$$\frac{\partial F_1}{\partial q} = 0_{3\times4} \tag{4.33}$$

$$\frac{\partial F_1}{\partial \omega} = \Lambda_{3\times3} = -J_p^{-1}Q \tag{4.34}$$

95

$$\frac{\partial F_2}{\partial q} = \frac{1}{2}\Omega(\omega)_{4\times 4} \tag{4.35}$$

$$\frac{\partial F_2}{\partial \omega} = \Gamma_{4\times 3} \tag{4.36}$$

where

$$Q = \Pi(\omega) \cdot J_p - \Pi(J_p\omega) \tag{4.37}$$

$$\Gamma = \frac{1}{2}\begin{bmatrix} q_4 & -q_3 & q_2 \\ q_3 & q_4 & -q_1 \\ -q_2 & q_1 & q_4 \\ -q_1 & -q_2 & -q_3 \end{bmatrix} \tag{4.38}$$

The anti-symmetric matrix operator $\Pi()$ operating on any vector $v = [v_x, v_y, v_z]^T$ is defined by

$$\Pi(v) = \begin{bmatrix} 0 & -v_z & v_y \\ v_z & 0 & -v_x \\ -v_y & v_x & 0 \end{bmatrix} \tag{4.39}$$

The subscript $i \times j$ in Equations (4.33) through (4.36) stands for the dimension of the corresponding matrix, i rows and j columns. This notation is repeatedly used later.

4.2.4 Observation Fitting Model and Partial Derivatives

As assumed before, the non-gravitational accelerations which occur during the center of mass calibration could be approximated by a linear function of the time. Ignoring the effects of scale factors and misalignment errors, the

96

accelerometer's observation model given by Equation (3.12) could be simplified as follows

$$A_{out} = \widetilde{A}d + \alpha t + \beta + A_n \tag{4.40}$$

where α and β represent the fitting slope and bias of the non-gravitational accelerations, respectively. The bias parameter β absorbs both the non-gravitational accelerations bias and the accelerometer measurement bias. The mapping matrix $\widetilde{A}$ is given by

$$\widetilde{A} = \begin{bmatrix} -\omega_y^2 - \omega_z^2 & \omega_x \omega_y - \dot{\omega}_z & \omega_x \omega_z + \dot{\omega}_y \\ \omega_x \omega_y + \dot{\omega}_z & -\omega_x^2 - \omega_z^2 & \omega_z \omega_y - \dot{\omega}_x \\ \omega_x \omega_z - \dot{\omega}_y & \omega_z \omega_y + \dot{\omega}_x & -\omega_y^2 - \omega_x^2 \end{bmatrix} \tag{4.41}$$

And the attitude quaternion observation model from the star camera can be written as

$$q_{obs} = q \tag{4.42}$$

Equations (4.40) and (4.42) will be used to fit the observation model for the estimation system. Partial derivatives with respect to the time-varying parameters $q(t), \omega(t)$ and the constant parameters d, α, β are required to linearize these observation equations. The partial derivatives are given by

$$\frac{\partial A_{out}}{\partial q} = 0_{3 \times 4} \tag{4.43}$$

$$\frac{\partial A_{out}}{\partial \omega} = \begin{bmatrix} \dfrac{\partial (\widetilde{A}_1 + \widetilde{A}_2)}{\partial \omega_x} d & \dfrac{\partial (\widetilde{A}_1 + \widetilde{A}_2)}{\partial \omega_y} d & \dfrac{\partial (\widetilde{A}_1 + \widetilde{A}_2)}{\partial \omega_z} d \end{bmatrix} \tag{4.44}$$

97

$$\frac{\partial A_{out}}{\partial d} = \tilde{A}_{3\times 3} \tag{4.45}$$

$$\frac{\partial A_{out}}{\partial \alpha} = tI_{3\times 3} \tag{4.46}$$

$$\frac{\partial A_{out}}{\partial \beta} = I_{3\times 3} \tag{4.47}$$

$$\frac{\partial q_{obs}}{\partial q} = I_{4\times 4} \tag{4.48}$$

$$\frac{\partial q_{obs}}{\partial \omega} = \frac{\partial q_{obs}}{\partial d} = \frac{\partial q_{obs}}{\partial \alpha} = \frac{\partial q_{obs}}{\partial \beta} = 0_{4\times 3} \tag{4.49}$$

where

$$\frac{\partial \tilde{A}_1}{\partial \omega_x} = \begin{bmatrix} 0 & \omega_y & \omega_z \\ \omega_y & -2\omega_x & 0 \\ \omega_z & 0 & -2\omega_x \end{bmatrix} \tag{4.50}$$

$$\frac{\partial \tilde{A}_1}{\partial \omega_y} = \begin{bmatrix} -2\omega_y & \omega_x & 0 \\ \omega_x & 0 & \omega_z \\ 0 & \omega_z & -2\omega_y \end{bmatrix} \tag{4.51}$$

$$\frac{\partial \tilde{A}_1}{\partial \omega_z} = \begin{bmatrix} -2\omega_z & 0 & \omega_x \\ 0 & -2\omega_z & \omega_y \\ \omega_x & \omega_y & 0 \end{bmatrix} \tag{4.52}$$

$$\frac{\partial \tilde{A}_2}{\partial \omega_x} = \Pi(\Lambda_1) \tag{4.53}$$

$$\frac{\partial \tilde{A}_2}{\partial \omega_y} = \Pi(\Lambda_2) \tag{4.54}$$

$$\frac{\partial \tilde{A}_2}{\partial \omega_z} = \Pi(\Lambda_3) \tag{4.55}$$

The subscript i of Λ in Equations (4.53) through (4.55) stands for the column of its matrix.

So far, the dynamic fitting model and observation fitting model and their partial derivatives are obtained for the center of mass calibration estimation system.

4.2.5 Estimation Algorithms

After preprocessing the observed star camera data and the Earth magnetic field measurement data, estimation of the proof mass offset can be performed by the algorithms proposed in this section. In this research, three batch algorithms are developed, Accelerometer and Star camera data Separate ESTimation (ASSEST), Accelerometer and Star camera data Combined Full-dimensioned ESTimation (ASCFEST) and Accelerometer and Star camera data Combined Reduced-dimensioned ESTimation (ASCREST). All of these algorithms process the accelerometer data, star camera data and magnetometer data.

ASSEST algorithm processes the accelerometer data and the other observation data separately. Star camera data and magnetometer data are used to estimate the angular motion related information, including angular velocity and angular acceleration. This can be fulfilled by algorithms Full Dimension Estimation (FDE) and Reduced Dimension Estimation (RDE) presented later, or simply by digitally filtering the observation data and deriving from the attitude kinematic equations of motion. Given the angular motion related information, the accelerometer data can be fitted into the accelerometer observation model to estimate the proof mass offset. This part of estimation is not involved with star camera data, which means that the star camera's observation data need not be used if the angular velocity and angular acceleration can be known by other

means. For example, the angular velocity can be measured by the gyro, and angular acceleration can be measured by accelerometer.

Both ASCFEST algorithm and ASCREST algorithm process all the observation data together. The only difference is that the former estimator tries to estimate the full-dimensioned quaternion as part of the estimate, while the later estimator estimates the small angles, which describes the small rotation between the real attitude orientation and the nominal attitude orientation, instead. The disadvantage of ASCFEST is that it may encounter a singularity because only three variables are independent in the four-dimension quaternion vector. ASCREST overcomes this potential problem by reducing one dimension.

Theoretically, all three estimators yield the same estimation accuracy since they use the same observation information and are based on same fitting model. In the data processing, the algorithm, which is most convenient for implementation, can be chosen.

In developing the estimation algorithms in the following sections, instead of presenting all the detail, only the state transition matrix and observation-state mapping matrix for each algorithm are developed. Using this information, the batch estimation can be performed based on estimation theory presented in Section 4.2.2. The overlapping parts of batch estimation and each algorithm are omitted for writing conciseness.

Besides the observation data, each algorithm for the center of mass calibration needs the satellite moment of inertia J_p and magnetic dipole moment m_m. The moment of inertia is provided by Astrium (Kruizinga, 2003). The

magnetic dipole moment can be calculated according to Equation (3.11), given the type of maneuver when commanding the expected torque, or is directly available for the commanding of magnetic moment.

4.2.5.1 ASSEST Algorithm

As mentioned before, ASSEST algorithm is composed of two estimators, one is to determine the angular motion related information, and the other is to estimate the proof mass offset once the angular information are available.

The angular motion related information can be obtained in several ways. Perhaps the easiest way is to measure it directly. Each GRACE satellite has an accelerometer and gyro on board. The former instrument can output angular acceleration and the later one can sense angular velocity. This approach is called "direct measurement" in this research. Besides direct measurement, the star camera observations can be fitted into the attitude dynamic model to estimate the initial angular velocity and quaternion value at the calibration epoch. Thereafter the angular velocity and acceleration can be propagated to any observation time. Since the four-dimension quaternion is constrained to be a unit vector, the attitude dynamic model may be massaged such that all variables are fully independent by reducing one dimension of the quaternion. In the following, FDE algorithm, with full-dimensioned quaternion, and RDE algorithm, with reduced-dimensioned quaternion, are proposed to determine the angular information. In addition, by digitally filtering the star camera's quaternion observations and feeding into the attitude kinematic model, the angular information can also be obtained. This method is called Kinematic Model Filtering (KMF) in this study.

Full Dimension Estimation

The dynamic model is given by

$$\dot{q}(t) = \frac{1}{2}\Omega(\omega)q(t) \tag{4.56}$$

$$\frac{d\omega}{dt} = J_p^{-1}(m_m \times B - \omega \times (J_p\omega)) \tag{4.57}$$

The star camera observation model is described by

$$q_{obs} = q \tag{4.58}$$

The estimated parameter vector is defined as $X(t) = [q(t), \omega(t)]^T$, and its corresponding state residual is $x(t) = [\Delta q(t), \Delta\omega(t)]^T$. Then the state transition matrix mapping state residual satisfies

$$\dot{\Phi}_{11} = \frac{1}{2}\Omega(\omega)\Phi_{11} \text{ , with } \Phi_{11}(t_0, t_0) = I \tag{4.59}$$

$$\dot{\Phi}_{12} = \frac{1}{2}\Omega(\omega)\Phi_{12} + \Gamma\Phi_{22} \text{ , with } \Phi_{12}(t_0, t_0) = 0 \tag{4.60}$$

$$\dot{\Phi}_{22} = \Lambda\Phi_{22} \text{ , with } \Phi_{22}(t_0, t_0) = I \tag{4.61}$$

The sub-matrix Φ_{21} is equal to 0. Based on these sub-matrices, the state transition matrix $\Phi(t_k, t_0)$ can be constructed as

$$\Phi(t_k, t_0) = \begin{bmatrix} \Phi_{11} & \Phi_{12} \\ 0 & \Phi_{22} \end{bmatrix}_{7\times7} \tag{4.62}$$

And the observation-state mapping matrix is given by

$$\tilde{H}(t_k) = [I \quad 0]_{4\times7} \tag{4.63}$$

102

This estimation approach can determine the initial angular velocity and the initial attitude quaternion of the satellite. Then the dynamic equations of motion can be integrated to give $q(t)$, $\omega(t)$ and $\dot{\omega}(t)$ at any time t.

This state vector may result in a singular covariance matrix since only three of four quaternion components are independent. Thus it may create a serious problem when the estimation is performed. However, several simulations have been performed using this method and no singularity was encountered. To overcome the potential singularity problem, an alternative method, the Reduced Dimension Estimation, is proposed.

Reduced Dimension Estimation

The dynamic model for this algorithm is the same as Equations (4.56) and (4.57). The observation model is the same as Equation (4.58).

Although the state vector is the same as that of FDE algorithm, the state residual vector is defined differently as follows

$$x(t) = \left[\Delta\varsigma(t), \Delta\omega(t) \right]^T \tag{4.64}$$

where $\Delta\omega(t)$ is $\omega(t) - \omega^*(t)$, and $\Delta\varsigma(t)$ is $[\Delta\varsigma_1, \Delta\varsigma_2, \Delta\varsigma_3]^T$, which is a set of small rotation angles, by the 3-2-1 sequence of the Euler angles, that rotates from the nominal attitude to the true attitude. Thus

$$\Re(q(t)) = C(\Delta\varsigma(t)) \cdot \Re(q^*(t)) \tag{4.65}$$

where

$$C(\Delta\varsigma(t)) = \begin{bmatrix} c_2 c_3 & c_2 s_3 & -s_2 \\ s_1 s_2 c_3 - c_1 s_3 & s_1 s_2 s_3 + c_1 c_3 & s_1 c_2 \\ c_1 s_2 c_3 + s_1 s_3 & c_1 s_2 s_3 - s_1 c_3 & c_1 c_2 \end{bmatrix} \qquad (4.66)$$

where the shorthand c_i is $\cos(\Delta\varsigma_i(t))$, and s_i is $\sin(\Delta\varsigma_i(t))$. A new operator $\otimes$, which is defined in more detail in Appendix B, is introduced such that Equation (4.65) can be rewritten in the following form

$$q(t) = \frac{1}{\sqrt{1 + |\Delta\varsigma(t)|^2 / 4}} \begin{bmatrix} \Delta\varsigma(t)/2 \\ 1 \end{bmatrix} \otimes q^*(t) \qquad (4.67)$$

The differential of $x(t) = [\Delta\varsigma(t), \Delta\omega(t)]^T$ is carried out as follows

$$\dot{x}(t) = \begin{bmatrix} \Pi(\omega^*(t)) & I \\ \Lambda & 0 \end{bmatrix} x \qquad (4.68)$$

The corresponding state transition matrix satisfies

$$\dot{\Phi}_{11} = \Pi(\omega(t^*))\Phi_{11} \text{ , with } \Phi_{11}(t_0, t_0) = I \qquad (4.69)$$
$$\dot{\Phi}_{12} = \Pi(\omega^*(t))\Phi_{12} + \Phi_{22} \text{ , with } \Phi_{12}(t_0, t_0) = 0 \qquad (4.70)$$
$$\dot{\Phi}_{22} = \Lambda\Phi_{22} \text{ , with } \Phi_{22}(t_0, t_0) = I \qquad (4.71)$$

The measurement model given by the Equation (4.58) furnishes an optimal estimation $q_{obs}(t_k)$ such that

$$q_{obs}(t) = \frac{1}{\sqrt{1 + |\Delta v(t)|^2 / 4}} \begin{bmatrix} \Delta v(t)/2 \\ 1 \end{bmatrix} \otimes q(t) \qquad (4.72)$$

where $\Delta v(t)$ represents a set of small rotation angles.

The new derived measurement $\Delta u(t)$, which is equivalent to the observation residual, is defined such that

$$q_{obs}(t) = \frac{1}{\sqrt{1 + |\Delta u(t)|^2 / 4}} \begin{bmatrix} \Delta u(t)/2 \\ 1 \end{bmatrix} \otimes q^*(t) \qquad (4.73)$$

The derived measurement can be explicitly given by

$$\Delta u_2 = -\sin^{-1} c_{13}$$
$$\Delta u_1 = \tan^{-1}\left(\frac{c_{23}}{\cos(\Delta u_2)}, \frac{c_{33}}{\cos(\Delta u_2)}\right) \qquad (4.74)$$
$$\Delta u_3 = \tan^{-1}\left(\frac{c_{12}}{\cos(\Delta u_2)}, \frac{c_{11}}{\cos(\Delta u_2)}\right)$$

where the matrix elements on the right hand of the above equations are from the matrix C, which is given by

$$C = \Re(q_{obs}) \cdot \Re(q^*)^{-1} \qquad (4.75)$$

Thus the observation residue is

$$y(t_k) = \Delta u(t_k) = \Delta \varsigma(t_k) + \Delta v(t_k) \qquad (4.76)$$

where $\Delta v(t_k)$ represents the measurement noise.

The state transition matrix $\Phi(t_k, t_0)$ can be constructed as

$$\Phi(t_k, t_0) = \begin{bmatrix} \Phi_{11} & \Phi_{12} \\ 0 & \Phi_{22} \end{bmatrix}_{6\times6} \qquad (4.77)$$

And the observation-state mapping matrix is given by

105

$$\tilde{H}(t_k) = \begin{bmatrix} I & 0 \end{bmatrix}_{3\times6} \tag{4.78}$$

Following the batch processing procedure described in Section 4.2.2, the estimate $\hat{x}(t_0) = [\Delta\hat{\varsigma}(t_0), \Delta\hat{\omega}(t_0)]^T$ can be obtained. The final state vector $\hat{X}(t_0) = [\hat{q}(t_0), \hat{\omega}(t_0)]^T$ can be updated as follows

$$\begin{bmatrix} \hat{q}(t_0) \\ \hat{\omega}(t_0) \end{bmatrix} = X^*(t_0) + \begin{bmatrix} \Delta q \\ \Delta\hat{\omega}(t_0) \end{bmatrix} \tag{4.79}$$

where $\Delta q = \bar{\Re}(E)$, and $E = C(\Delta\hat{\varsigma}(t_0)) \cdot \Re(q^*)$.

Of course, the initial state can be improved by iteration. Additionally, the dynamic equations of motion can be propagated to give $q(t)$, $\omega(t)$ and $\dot{\omega}(t)$ at any time t.

Kinematic Model Filtering

The CRN filter is applied to the quaternion data, q, to get the differentials as follows

$$\dot{q} = CRN'(q) \tag{4.80}$$

Then the angular velocity can be obtained from attitude kinematic equations of motion as follows

$$\begin{aligned}
\omega_x &= 2(q_4 \cdot \dot{q}_1 + q_3 \cdot \dot{q}_2 - q_2\dot{q}_3 - q_1\dot{q}_4) \\
\omega_y &= 2(q_4 \cdot \dot{q}_2 - q_3 \cdot \dot{q}_1 - q_2\dot{q}_4 + q_1\dot{q}_3) \\
\omega_z &= 2(q_4 \cdot \dot{q}_3 - q_3 \cdot \dot{q}_4 + q_2\dot{q}_1 - q_1\dot{q}_2)
\end{aligned} \tag{4.81}$$

After the angular velocity is obtained, the angular acceleration can be obtained as a first derivative by the CRN filter as

$$\dot{\omega} = CRN'(\omega) \qquad (4.82)$$

By this approach, the $q(t)$, $\omega(t)$ and $\dot{\omega}(t)$ at any time t can be determined from the attitude kinematic equations of motion and the star camera observations.

After the angular motion information are available, the proof mass offset can be estimated by fitting the accelerometer observations. The fitting model is the same as Equation (4.40). Let the estimated parameter be $X = [d, \alpha, \beta]^T$, then the observation-state mapping matrix is given by

$$H(t_k) = \begin{bmatrix} \widetilde{A} & t_k I & I \end{bmatrix}_{3 \times 9} \qquad (4.83)$$

Therefore, given the accelerometer observation data $\{A_{out}(t_1), A_{out}(t_2), ... A_{out}(t_m)\}$ as the observation vector and observation weight matrix R^{-1}, the estimate of the proof mass offset can be determined from the linear model.

4.2.5.2 ASCFEST Algorithm

The dynamic model for this algorithm is the same as Equations (4.56) and (4.57) and the observation model is the same as Equations (4.40) and (4.58).

The estimated parameter vector is defined as $X(t) = [q(t), \omega(t), d, \alpha, \beta]^T$, and its corresponding state residual is $x(t) = [\Delta q(t), \Delta \omega(t), \Delta d, \Delta \alpha, \Delta \beta]^T$. Given the initial guess of the estimated vector $X^*(t_0)$, Equations (4.56) and (4.57) and

state transition matrices (4.59) through (4.61) can be numerically integrated jointly. The state transition matrix $\Phi(t_k, t_0)$ mapping the state residual can be constructed as

$$\Phi(t_k, t_0) = \begin{bmatrix} \Phi_{11} & \Phi_{12} & 0 & 0 & 0 \\ 0 & \Phi_{22} & 0 & 0 & 0 \\ 0 & 0 & I_{3\times3} & 0 & 0 \\ 0 & 0 & 0 & I_{3\times3} & 0 \\ 0 & 0 & 0 & 0 & I_{3\times3} \end{bmatrix}_{16\times16} \tag{4.84}$$

And the observation-state mapping matrix is given by

$$\tilde{H}(t_k) = \begin{bmatrix} 0 & \dfrac{\partial A_{out}}{\partial \omega} & \tilde{A} & t_k I_{3\times3} & I_{3\times3} \\ I_{4\times4} & 0 & 0 & 0 & 0 \end{bmatrix}_{7\times16} \tag{4.85}$$

Given the accelerometer observation data $\{A_{out}(t_1), A_{out}(t_2), ... A_{out}(t_m)\}$ and star camera data $\{q_{obs}(t_1), q_{obs}(t_2), ... q_{obs}(t_m)\}$, state residual can be estimated. The updated parameter vector includes the proof mass offset. Furthermore, the estimate can be improved by iteration.

4.2.5.3 ASCREST Algorithm

The dynamic model for this algorithm is the same as Equations (4.56) and (4.57) and the observation model is the same as Equations (4.40) and (4.58).

The estimated parameter vector is defined as $X(t) = [q(t), \omega(t), d, \alpha, \beta]^T$. Unlike ASCFEST algorithm, the corresponding state residual for this algorithm is defined as $x(t) = [\Delta\varsigma(t), \Delta\omega(t), \Delta d, \Delta\alpha, \Delta\beta]^T$, where $\Delta\varsigma(t)$ is the same as in Equation (4.65).

The differential of the state residual is carried out as follows

$$\dot{x}(t) = \begin{bmatrix} \Pi(\omega^*(t)) & I & 0 & 0 & 0 \\ \Lambda & 0 & 0 & 0 & 0 \\ 0 & 0 & 0 & 0 & 0 \\ 0 & 0 & 0 & 0 & 0 \\ 0 & 0 & 0 & 0 & 0 \end{bmatrix} x(t) \tag{4.86}$$

Given the initial guess of the estimated parameter $X^*(t_0)$, Equations (4.56) and (4.57) and state transition matrices (4.69) through (4.71) can be integrated together. The state transition matrix corresponding to the state residual is constructed as

$$\Phi(t_k, t_0) = \begin{bmatrix} \Phi_{11} & \Phi_{12} & 0 & 0 & 0 \\ 0 & \Phi_{22} & 0 & 0 & 0 \\ 0 & 0 & I_{3\times3} & 0 & 0 \\ 0 & 0 & 0 & I_{3\times3} & 0 \\ 0 & 0 & 0 & 0 & I_{3\times3} \end{bmatrix}_{15\times15} \tag{4.87}$$

The observation residual with respect to the accelerometer observation is as usually defined, and, with respect to the star camera observation is the same as Equation (4.76). The observation-state mapping matrix is given by

$$\tilde{H}(t_k) = \begin{bmatrix} 0 & \dfrac{\partial A_{out}}{\partial \omega} & \tilde{A} & t_k I_{3\times3} & I_{3\times3} \\ I_{3\times3} & 0 & 0 & 0 & 0 \end{bmatrix}_{6\times15} \tag{4.88}$$

Given the accelerometer observations and star camera observations, the state residual can be estimated. The final update of the estimated parameter gives

the estimate of the proof mass offset. If necessary, the proof mass offset can be improved by iteration. Before each iteration, the nominal quaternion vector has to be normalized.

4.2.6 Covariance Analysis and Optimal Location Criterion

It is essential to analyze the covariance matrix of the estimate. For simplification, the linear terms are eliminated from the simplified accelerometer observation model. In addition, since the angular acceleration will be much larger than the product of the angular velocities, the angular velocity induced acceleration is ignored. Using these assumptions, the covariance of the proof mass offset estimate along each axis can be approximated as

$$\sigma^2(d_k) = F \cdot \omega_k^2 \quad (k = x, y, z) \tag{4.89}$$

where F is a scale variable of angular acceleration.

From the accelerometer observation model, it can be seen that the larger angular acceleration is, the stronger the angular motion related acceleration signal is, which permits the proof mass offset to be easily detected. However, the covariance matrix indicates that the covariance of estimate along each axis is proportional to the angular acceleration along its axis, which implies that the larger angular acceleration along one axis, the least insensitive of the proof mass offset along that axis is observed. So there should be a careful design of the calibration maneuver in order to obtain an accurate proof mass offset determination along each axis. Once the expected torque or magnetic moment is telecommanded, the resultant angular acceleration is totally dependent upon the

satellite location over the Earth. Based on this covariance analysis and simulations presented later, the optimal location criterion is summarized as follows.

Optimal location criterion: The center of mass calibration should be carried out at location over the Earth where the angular acceleration during the calibration is large enough and also is of the same order along each axis.

With this criterion, the proof mass offset along each axis can be estimated from one single center of mass calibration maneuver. This is a very important rule for finding the optimal location over the Earth when the maneuver is done.

By applying the center of mass calibration maneuver at the optimal calibration location to GRACE satellite, the proof mass offset can be determined with good accuracy by the estimation algorithms proposed in the previous sections. This will be demonstrated in the simulations later. However, several important points should be brought out before switching to K-band ranging system calibration.

The Earth's magnetic field is measured by the magnetometer, whose data are used in modeling the active torque during the COM calibration. However, the magnetometer could fail during the GRACE mission lifetime. If this happens, the spherical harmonic model for the Earth's magnetic field can be used to create the magnetic field data. Given the satellite's position, determined accurately from GPS observations, and the satellite's attitude orientation, determined from the star cameras, and a good set of IGRF gaussian coefficients, the Earth magnetic field model can be used to produce the Earth magnetic field data. It is expected that

loss of magnetometer data would not affect the center of mass calibration accuracy too much.

After the proof mass offset is determined, the MTM system is operated to adjust the proof mass of the accelerometer to be coincident with the center of mass of the satellite. Follow-up calibrations can be performed to test if the offset is within the tolerance. If the proof mass offset is still large, due to inaccurate proof mass offset determination and/or inaccurate MTM's mass balancing operation, the center of mass calibration should be repeated, until the proof mass offset is within the required tolerance.

4.3 ALGORITHMS FOR LINEARLY DRIFTING KBR CALIBRATION

The observation data set for linearly drifting K-band ranging system calibration, as defined in the previous chapter, includes the KBR range rate data, star camera observations, magnetometer observations and PODs from GPS observations. The K-band ranging system provides observations of phase response to the rotating satellite. The attitude determination from the star camera and orbit determination from the GPS provide precise satellite relative orbit and attitude configuration. In addition, the observations of the star camera and the magnetometer permit an accurate attitude dynamic model to be established and therefore the angular motion information can be well known. All of this information at each sub-maneuver are packed together into the estimation algorithms, which can estimate the phase centers of both antennas of the GRACE satellites.

112

There will be two different estimation algorithms proposed for this KBR calibration maneuver. Starting from the dynamic fitting model and observation fitting model, the estimation algorithms will be fully investigated in this section.

The data rate of range rate is 10 Hz while the data rates of star camera and magnetometer are 1 Hz, 0.1 Hz, respectively. The orbit determination from the GPS observations usually has a small data rate, such as 0.2 Hz and 0.1 Hz. The low output frequency data require interpolation just as in COM calibration. The same preprocessing algorithm described in Section 4.2.1 can be applied to star camera data, magnetometer data and precise orbits in order to produce derived data of same data rate as range rate.

The attitude dynamic fitting model and partial derivatives are the same as described in Section 4.2.3 for center of mass calibration. The observation fitting model and estimation algorithms will be presented below.

4.3.1 Observation Fitting Model and Partial Derivatives

The KBR range and range rate observation model can be rewritten as follows

$$R = \left| \vec{R}_1 - \vec{R}_2 \right| + R_{br} + R_{nr} \tag{4.90}$$

$$RR = \frac{(\vec{R}_1 - \vec{R}_2) \cdot (\dot{\vec{R}}_1 - \dot{\vec{R}}_2)}{\left| \vec{R}_1 - \vec{R}_2 \right|} + RR_n \tag{4.91}$$

where the characteristics of noises R_{nr}, RR_n are specified with mean $E(R_{nr}) = E(RR_n) = 0$, and covariance $E(R_{nr} R_{nr}^T) = R_r$ and $E(RR_n RR_n^T) = R_{rr}$.

And the attitude quaternion observation model from the star camera can be rewritten as

$$q_{obs} = q \qquad (4.92)$$

Equations (4.90) through (4.92) will be used to fit the observation model for the estimation system. Carrying out the partial derivatives of Equation (4.90) about $q_1, \omega_1, q_2, \omega_2, \vec{d}_{pc1}, \vec{d}_{pc2}$ yields

$$\frac{\partial R}{\partial q_1} = e^T \begin{bmatrix} A_1 d_{pc1} & B_1 d_{pc1} & C_1 d_{pc1} & D_1 d_{pc1} \end{bmatrix} \qquad (4.93)$$

$$\frac{\partial R}{\partial \omega_1} = 0_{1\times3} \qquad (4.94)$$

$$\frac{\partial R}{\partial q_2} = -e^T \begin{bmatrix} A_2 d_{pc2} & B_2 d_{pc2} & C_2 d_{pc2} & D_2 d_{pc2} \end{bmatrix} \qquad (4.95)$$

$$\frac{\partial R}{\partial \omega_2} = 0_{1\times3} \qquad (4.96)$$

$$\frac{\partial R}{\partial R_{br}} = 1 \qquad (4.97)$$

$$\frac{\partial R}{\partial d_{pc1}} = e^T M_1 \qquad (4.98)$$

$$\frac{\partial R}{\partial d_{pc2}} = -e^T M_2 \qquad (4.99)$$

where M_1 and M_2 are rotation matrices from the satellite body-fixed frame to inertial system, and

$$e = \frac{(\vec{R}_1 - \vec{R}_2)}{\left| \vec{R}_1 - \vec{R}_2 \right|} \qquad (4.100)$$

114

$$A = \begin{bmatrix} 0 & 2q_2 & 2q_3 \\ 2q_2 & -4q_1 & -2q_4 \\ 2q_3 & 2q_4 & -4q_1 \end{bmatrix} \qquad (4.101)$$

$$B = \begin{bmatrix} -4q_2 & 2q_1 & 2q_4 \\ 2q_1 & 0 & 2q_3 \\ -2q_4 & 2q_3 & -4q_2 \end{bmatrix} \qquad (4.102)$$

$$C = \begin{bmatrix} -4q_3 & -2q_4 & 2q_1 \\ 2q_4 & -4q_3 & 2q_2 \\ 2q_1 & 2q_2 & 0 \end{bmatrix} \qquad (4.103)$$

$$D = \begin{bmatrix} 0 & -2q_3 & 2q_2 \\ 2q_3 & 0 & -2q_1 \\ -2q_2 & 2q_1 & 0 \end{bmatrix} \qquad (4.104)$$

The derivative of Equation (4.91) about any variable p is of the same form as follows

$$\frac{\partial RR}{\partial p} = \frac{\partial e}{\partial p} \cdot (\dot{\vec{R}}_1 - \dot{\vec{R}}_2) + e \cdot \frac{\partial (\dot{\vec{R}}_1 - \dot{\vec{R}}_2)}{\partial p} \qquad (4.105)$$

where $p \in \{q_1, \omega_1, q_2, \omega_2, \vec{d}_{pc1}, \vec{d}_{pc2}\}$.

More explicitly

$$\frac{\partial e}{\partial p} = \frac{\partial (\vec{R}_1 - \vec{R}_2)}{\partial p} \cdot \frac{1}{\left| \vec{R}_1 - \vec{R}_2 \right|} - e \cdot (\frac{\partial R}{\partial p}) \cdot \frac{1}{\left| \vec{R}_1 - \vec{R}_2 \right|} \qquad (4.106)$$

$$\frac{\partial (\dot{\vec{R}}_1 - \dot{\vec{R}}_2)}{\partial q_1} = \begin{bmatrix} A_1 \Pi(\omega_1) d_{pc1} & B_1 \Pi(\omega_1) d_{pc1} & C_1 \Pi(\omega_1) d_{pc1} & D_1 \Pi(\omega_1) d_{pc1} \end{bmatrix} \qquad (4.107)$$

$$\frac{\partial (\dot{\vec{R}}_1 - \dot{\vec{R}}_2)}{\partial \omega_1} = \begin{bmatrix} M_1 S_1 d_{pc1} & M_1 S_2 d_{pc1} & M_1 S_3 d_{pc1} \end{bmatrix} \qquad (4.108)$$

$$\frac{\partial (\dot{\vec{R}}_1 - \dot{\vec{R}}_2)}{\partial q_2} = -\begin{bmatrix} A_2 \Pi(\omega_2) d_{pc2} & B_2 \Pi(\omega_2) d_{pc2} & C_2 \Pi(\omega_2) d_{pc2} & D_2 \Pi(\omega_2) d_{pc2} \end{bmatrix} \qquad (4.109)$$

$$\frac{\partial (\dot{\vec{R}} - \dot{\vec{R}})}{\partial \omega_2} = -\left[M_2 S_1 d_{pc2} \quad M_2 S_2 d_{pc2} \quad M_2 S_3 d_{pc2} \right] \tag{4.110}$$

$$\frac{\partial (\dot{\vec{R}}_1 - \dot{\vec{R}}_2)}{\partial d_{pc1}} = M_1 \Pi(\omega_1) \tag{4.111}$$

$$\frac{\partial (\dot{\vec{R}}_1 - \dot{\vec{R}}_2)}{\partial d_{pc2}} = M_1 \Pi(\omega_1) \tag{4.112}$$

where

$$S_1 = \begin{bmatrix} 0 & 0 & 0 \\ 0 & 0 & -1 \\ 0 & 1 & 0 \end{bmatrix} \tag{4.113}$$

$$S_2 = \begin{bmatrix} 0 & 0 & 1 \\ 0 & 0 & 0 \\ -1 & 0 & 0 \end{bmatrix} \tag{4.114}$$

$$S_3 = \begin{bmatrix} 0 & -1 & 0 \\ 1 & 0 & 0 \\ 0 & 0 & 0 \end{bmatrix} \tag{4.115}$$

The derivatives of Equation (4.92) are given as follows

$$\frac{\partial q_{obs}}{\partial q} = I_{4 \times 4} \tag{4.116}$$

$$\frac{\partial q_{obs}}{\partial \omega} = \frac{\partial q_{obs}}{\partial d_{pc1}} = \frac{\partial q_{obs}}{\partial d_{pc2}} = 0_{4 \times 3} \tag{4.117}$$

This completes the partial derivatives of the observation model for the linear drifting KBR calibration.

116

4.3.2 Batch Estimation of KBR Phase Centers

After preprocessing the observation data, the estimation algorithms can be applied. In this research, two batch estimation algorithms for this kind of KBR calibration are proposed, KBR and Star camera data Separate ESTimation (KSSEST), KBR and Star camera data Combined Full-dimensioned ESTimation (KSCFEST). These two estimators use same input information, KBR range rate data, star camera data, magnetometer data and PODs from GPS observations.

Interestingly, it has been found that the range rate, instead of range, can yield good determination accuracy of phase centers for this calibration maneuver. So in the following algorithms, range rate rather than range observations are processed.

KSSEST algorithm processes the KBR range rate data and the star camera data separately. In each calibration sub-maneuver, star camera data and magnetometer data are fitted into attitude dynamic equations of motion and kinematic equations of motion to estimate the initial angular velocity and quaternion and to propagate these quantities to any time during the KBR calibration. With this information, the KBR range rate data from all sub-maneuvers are combined and fitted into the KBR observation model to estimate the antenna phase centers. This algorithm is a counterpart of ASSEST in the center of mass calibration.

The KSCFEST algorithm processes the observation data from all sub-maneuvers jointly, and estimates the four-dimension quaternion, besides the phase centers. The disadvantage of KSCFEST is that it may encounter a singularity

because only three variables are independent in the four-dimension quaternion vector. But in fact, no singularity problem has been encountered in the simulations. This approach is a counterpart of ASCFEST in center of mass calibration.

In the following algorithm presentations, a variable or a set of variables with a subscript or superscript MA, MB, MC or MD represents sub-maneuver A, sub-maneuver B, sub-maneuver C or sub-Maneuver D, respectively.

Although each sub-maneuver has three calibration phases, the observation data only from the last phase are processed. Besides the observation data, each algorithm requires the satellite moment of inertia J_p, and the magnetic dipole moment m_m activated at each sub-maneuver.

4.3.2.1 KSSEST Algorithm

The angular velocity and quaternion of each sub-maneuver can be estimated by the estimation algorithms presented in the Section 4.2.5.1. Thereafter, the KBR range rate observations can be processed.

The observation model at each sub-maneuver is the same as Equation (4.91), rewritten as

$$RR = \frac{(\vec{R}_1 - \vec{R}_2) \cdot (\dot{\vec{R}}_1 - \dot{\vec{R}}_2)}{\left| \vec{R}_1 - \vec{R}_2 \right|} + RR_n \qquad (4.118)$$

The precise orbit, attitude and angular motion of each satellite are directly used in the above model without any adjustment. Therefore, the estimated

118

parameter vector is $X = [d_{pc1}, d_{pc2}]^T$ and state residual is $x = [\Delta d_{pc1}, \Delta d_{pc2}]^T$. Its observation-state mapping matrix is given by

$$H(t_k) = \begin{bmatrix} \dfrac{\partial RR}{\partial d_{pc1}} & \dfrac{\partial RR}{\partial d_{pc2}} \end{bmatrix} \qquad (4.119)$$

The batch processor computational algorithm outlined in Figure 4.1 is still valid for this estimation system. However, in this case, the accumulations have to be done for all sub-maneuvers. The normal matrix can be accumulated with each observation and each sub-maneuver as

$$(H^T R^{-1} H) = \sum_{p=A,B,C,D} \sum_{k=1}^{m} (H^{Mp}(t)_k)^T R_{rr}^{-1} H^{Mp}(t)_k \qquad (4.120)$$

where k is an observation index, and p is a sub-maneuver index.

The observation residual can be accumulated as

$$(H^T R^{-1} y) = \sum_{p=A,B,C,D} \sum_{k=1}^{m} H^{Mp}(t)_k R_{rr}^{-1} y^{Mp} \qquad (4.121)$$

Finally, the estimate is

$$\hat{x} = (H^T R^{-1} H)^{-1} H^T R^{-1} y \qquad (4.122)$$

Therefore, the phase centers of both antennas can be found. Of course, the estimate can be improved by iteration.

4.3.2.2 KSCFEST Algorithm

The dynamic model at each sub-maneuver is given by

$$\dot{q}(t) = \frac{1}{2}\Omega(\omega)q(t) \tag{4.123}$$

$$\frac{d\omega}{dt} = J^{-1}(T_d - \omega \times (J\omega)) \tag{4.124}$$

where T_d represents the dominating active torque, it can be $m_m \times B$ if the magnetic torques are applied or 0 if no active torque works.

The observation model at each sub-maneuver is given as follows

$$RR = \frac{(\vec{R}_1 - \vec{R}_2) \cdot (\dot{\vec{R}}_1 - \dot{\vec{R}}_2)}{\left| \vec{R}_1 - \vec{R}_2 \right|} + RR_n \tag{4.125}$$

$$q_{obs} = q_1 \tag{4.126}$$

$$q_{obs} = q_2 \tag{4.127}$$

The estimated parameter vector of this complicated estimation system is $X(t) = \left[q_1^{MA}, \omega_1^{MA}, q_2^{MA}, \omega_2^{MA}, q_1^{MB}, \omega_1^{MB}, \cdots d_{pc1}, d_{pc2} \right]$. Given the initial guess of the estimated vector $X^*(t_0)$, Equations (4.123), (4.124) and the state transition matrices (4.59) through (4.61) can be integrated for each satellite. Then the state transition matrix $\Phi(t_k, t_0)$ at each sub-maneuver can be constructed as

$$\Phi(t_k, t_0) = \begin{bmatrix} \Phi_{11}^1 & \Phi_{12}^1 & 0 & 0 & 0 & 0 \\ 0 & \Phi_{22}^1 & 0 & 0 & 0 & 0 \\ 0 & 0 & \Phi_{11}^2 & \Phi_{12}^2 & 0 & 0 \\ 0 & 0 & 0 & \Phi_{22}^2 & 0 & 0 \\ 0 & 0 & 0 & 0 & I_{3\times3} & 0 \\ 0 & 0 & 0 & 0 & 0 & I_{3\times3} \end{bmatrix}_{20\times20} \tag{4.128}$$

The observation-state mapping matrix is given by

$$\widetilde{H}(t_k) = \begin{bmatrix} \partial/\partial q_1 & \partial/\partial \omega_1 & \partial/\partial q_2 & \partial/\partial \omega_2 & \partial/\partial d_{pc1} & \partial/\partial d_{pc2} \\ I & 0 & 0 & 0 & 0 & 0 \\ 0 & 0 & I & 0 & 0 & 0 \end{bmatrix}_{9 \times 20} \quad (4.129)$$

where the first row of the above equation is partial derivative with respect to range rate.

The Equations from (4.120) through (4.122) presented in the above section can be used to estimate the phase centers.

4.4 ALGORITHM FOR PERIODIC OSCILLATION KBR CALIBRATION

As stated in Section 3.1, the required observation set for this KBR calibration includes KBR range data, star camera data and PODs from GPS observations. From the data processing point of view, the major differences from linearly drifting KBR calibration are the attitude dynamic equations of motion are no longer needed and the rang observations are processed instead of range rate.

The star camera observation data are used directly to determine the attitude orientations of both satellites. The observation noise and misalignment of the star camera frame induce certain errors to the phase centers determination. GPS receiver assembly onboard each satellite allows to accurately determine the position of satellite. However, only relative position is in the range observation and the single satellite's position error may be partially cancelled due to some similar perturbations. In addition, during the KBR calibration, combinations of magnetic torque and thruster torque are used to oscillate the satellite about a biased angle. The oscillation period is generally smaller than the orbit perturbation period. In the range observation model, it is expected that the relative

121

orbit determination errors can be smooth enough to be filtered by polynomial function.

The range observation is modeled the same as Equation (4.90). Suppose that the relative position is determined as $\vec{r}_{12}^{*}$, and its error can be fitted by polynomial function, then the range fitting model can be simplified as follows

$$R = \left| \vec{r}_{12}^{*} + \Re(q_1)^T \Theta(\vec{d}_{pc1}) - \Re(q_2)^T \Theta(\vec{d}_{pc2}) \right| + R_{br} + R_{nr} + Poly(n) \quad (4.130)$$

where $Poly(n)$ represents the n-th order polynomial function, i.e., $a_n t^n + \ldots + a_1 t + a_0$. The partial derivatives of the range model about the phase centers and bias can be found in Equations (4.97) through (4.99). The partial derivative about any polynomial function coefficient a_i is given as follows

$$\frac{\partial R}{\partial a_i} = t^i \qquad (i = 0,1,2,\ldots n) \qquad (4.131)$$

The estimated parameter of this system is defined as a high dimension vector $X = \left[d_{pc1}, d_{pc2}, R_{br}^{MA}, \ldots R_{br}^{MD}, a_i^{MA}, \ldots a_i^{MD} \right]$. Given the initial guess of the estimated vector X^{*} and the observation data, the observation residual for each sub-maneuver can be obtained as

$$y = R - \left| \vec{r}_{12}^{*} + M_1 \Theta(\vec{d}_{pc1}^{*}) - M_2 \Theta(\vec{d}_{pc2}^{*}) \right| - R_{br}^{*} - Poly(n)^{*} \quad (4.132)$$

The mark * indicates the nominal values. The observation-state mapping matrix of sub-maneuver A is given by

$$H_{MA} = \begin{bmatrix} \dfrac{\partial R_{MA}}{\partial d_{pc1}} & \dfrac{\partial R_{MA}}{\partial d_{pc2}} & 1 & 0 & 0 & 0 & \dfrac{\partial R_{MA}}{\partial a_i^{MA}} & 0 & 0 & 0 \end{bmatrix} \quad (4.133)$$

Likewise, the observation-state mapping matrix for other sub-maneuvers can be obtained. Then the Equations from (4.120) through (4.122) can be used to estimate the phase centers except that weight matrix R_r^{-1} is used instead of R_{rr}^{-1}. In this study, a fourth order polynomial function is used.

4.4.1 Noise Analysis

There are three noise sources for this estimation system, K-band ranging system phase (range) observation noise, relative position determination error of the satellites and the attitude quaternion error. All these errors could decrease the accuracy of the phase centers determination.

The K-band ranging system range observation noise includes oscillator noise, system noise and mutipath noise. In a short time interval, the oscillator noise and system noise have very small drifts. They can be treated as the range bias and easily removed by the above algorithm. In case the maneuver takes a long time, there may be drift present. Even so, the drift can be fitted by this polynomial function term.

In order to analyze the effect of multipath noise, a one degree of freedom case, i.e., the sub-maneuver A, with only multipath noise is considered. To highlight the phase change due to the angular motions of the spacecraft, the derived range change, $\left| \vec{r}_1 - \vec{r}_2 \right| - R$, the difference of the distance between COMs

of GRACE satellites and KBR range data, is used in the analysis. The derived range change can be approximated as follows

$$R(\theta) = T - L\cos(\theta + \psi) \qquad (4.134)$$

where T is a bias, $L = \sqrt{x_{pc1}^2 + y_{pc1}^2}$, and $\psi = \arctan\dfrac{y_{pc1}}{x_{pc1}}$. Note this equation is consistent with Equation (1.4).

The observed derived range is corrupted with the multipath noise as follows

$$R^{obs}(\theta) = R(\theta) + \mu|\theta| \qquad (4.135)$$

Substituting the rotation angle θ with θ_{yaw}^1, in form of Equation (3.1), into the above equation and expanding it yield

$$\begin{aligned} R^{obs}(\theta) = T - L\cos(\psi + \theta_\circ)\cos(A\sin(\omega t)) + L\sin(\psi + \theta_\circ)\sin(A\sin(\omega t)) \\ + \mu|\theta_0 + A\sin(\omega t)| \end{aligned} \qquad (4.136)$$

Since the angle variation is small, the observed derived range can be simplified as

$$R^{obs}(\theta) = T' + (L\sin(\psi + \theta_\circ) \pm \mu)A\sin(\omega t) \qquad (4.137)$$

On the other hand, the fitting model without the multipath noise is

$$R^{obs}(\theta) = T' + \hat{L}\sin(\hat{\psi} + \theta_\circ)A\sin(\omega t) \qquad (4.138)$$

Therefore, in the estimation, the following equation is satisfied.

$$L\sin(\psi + \theta_0) \pm \mu = \hat{L}\sin(\hat{\psi} + \theta_\circ) \qquad (4.139)$$

The K-band horn is mounted far away, about 1.4 meters, from the center of mass of the satellite. Therefore, it is reasonable to assume that $L = \hat{L}$. Thus

$$\hat{\psi} = \psi \pm \frac{\mu}{L} \qquad (4.140)$$

The sign in the above equation depends on the oscillation angle θ. From this equation, it can be seen that the multipath noise can shift the phase angle ψ of the phase center. The shifting magnitude is determined by L and μ. What is more important, at sub-maneuver with $(\theta_0 > 0)$, the multipath effect in Equation (4.140) takes a positive sign, while at mirror sub-maneuver $(\theta_0 < 0)$, it takes a negative sign. If the mutipath error parameter, μ, is same for the sub-maneuver and its mirror sub-maneuver, this error can be cancelled when the estimates are averaged from these two sub-maneuvers. However, this assumption might be not true.

The relative position error is smooth and can be removed by a polynomial function.

In addition, the attitude quaternion from the star camera can be accurate enough to be used directly. However, the misalignment error and measurement noise are reflected in the SCA observations. It is necessary to analyze the effect of the attitude quaternion error on the phase center determination by means of consider covariance analysis.

For simplicity, only one sub-maneuver without other error sources are considered. The sensitivity of the attitude quaternion error $(\Delta q_1, \Delta q_2)$ to the estimate of the phase centers is given by

$$F = -(H_x^T R_r^{-1} H_x)^{-1}(H_x^T R_r^{-1} H_c) \qquad (4.141)$$

where

$$H_x = \left[\begin{array}{cc} \dfrac{\partial R}{\partial d_{pc1}} & \dfrac{\partial R}{\partial d_{pc2}} \end{array} \right] \qquad (4.142)$$

$$H_c = \left[\begin{array}{cc} \dfrac{\partial R}{\partial q_1} & \dfrac{\partial R}{\partial q_2} \end{array} \right] \qquad (4.143)$$

This sensitivity analysis indicates how star camera observation errors affect phase center determination.

4.5 ANTENNA BORESIGHT

Since the KBR range observation has a bias, the direction of the phase center determination, instead of magnitude, is more important. Therefore, the determination accuracy of the phase center is weighed by the antenna boresight determination error, as defined below.

The boresight is shown in Figure 4.2. In this figure, o-xyz is the line-of-sight frame where the origin o is the center of mass of the satellite, with PC_{ir} and PC_{ie} representing the true and estimated phase center, respectively. The line-of-sight frame is determined by the positions of both satellites. The x_i axis is defined to be pointing to each other, the z_i axis points radial downward and the y_i axis points out of the orbital plane. The boresight is defined as the direction pointing to

126

the phase center from the center of mass. The phase center determination error is defined by θ_{ier}, where i is the satellite index.
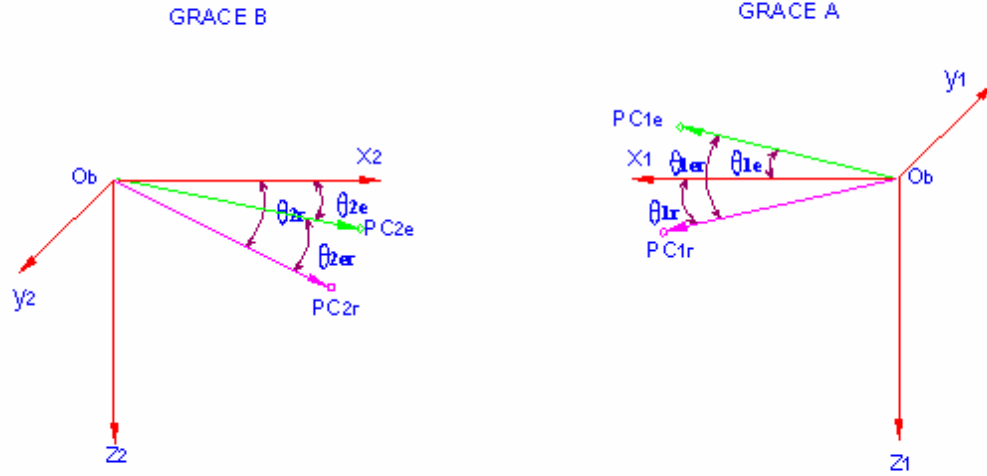

Figure 4.2   Boresight Definition

The boresight, defined in the line-of-sight frame, is the same as seen in the star camera frame. Thus the KBR calibration determines the alignment of the K-band boresight with the star camera.

4.6 KBR MISALIGNMENT CORRECTION

Knowing the phase centers of the K-band ranging system and the attitude orientations of both satellites, corrections can be applied in the KBR range processing to compensate the geometric misalignment of COMs and phase centers.

Given the positions of GRACE satellites A and B in the inertial frame, $\vec{r}_1(x_1, y_1, z_1)^T$ and $\vec{r}_2(x_2, y_2, z_2)^T$, the line-of-sight frame of GRACE B is defined as

$$\hat{x}_2 = \frac{(\vec{r}_1 - \vec{r}_2)}{|\vec{r}_1 - \vec{r}_2|}$$

$$\hat{y}_2 = \frac{(\vec{r}_1 - \vec{r}_2) \times \vec{r}_1}{|(\vec{r}_1 - \vec{r}_2) \times \vec{r}_1|} \qquad (4.144)$$

$$\hat{z}_2 = \hat{x}_2 \times \hat{y}_2$$

The rotation matrix from inertial frame to line-of-sight frame of GRACE B is defined as

$$LOS_2 = \begin{bmatrix} \hat{x}_2^T \\ \hat{y}_2^T \\ \hat{z}_2^T \end{bmatrix} \qquad (4.145)$$

The phase centers of GRACE A and GRACE B in this frame, d_{LPC1} and d_{LPC2}, can be obtained as follows

$$d_{LPC1} = LOS_2 \cdot \Re(q_1)^{-1} d_{PC1} + \begin{bmatrix} b & 0 & 0 \end{bmatrix}^T \qquad (4.146)$$

$$d_{LPC2} = LOS_2 \cdot \Re(q_2)^{-1} d_{PC2} \qquad (4.147)$$

where d_{PCi} $(i = 1,2)$ is the phase center of GRACE A/B in its own body-fixed frame, q_i is the attitude quaternion of GRACE A/B and b is the range between the COMs of both satellites.

Thus the real range between phase centers is given by

$$r = |d_{LPC2} - d_{LPC1}|$$
$$\approx b + x_{LPC1} - x_{LPC2} \qquad (4.148)$$

where x_{LPCi} is the x component of d_{LPCi}. Therefore, the correction due to the misalignment of COMs and phase centers is

$$\Delta = -x_{LPC1} + x_{LPC2} \qquad (4.149)$$

If the first rows of the matrices $LOS_2 \cdot \Re(q_1)^{-1}$ and $LOS_2 \cdot \Re(q_2)^{-1}$ are denoted as ℓ_1 and ℓ_2, then the correction can be written as

$$\Delta = -\ell_1 \cdot d_{PC1} + \ell_2 \cdot d_{PC2}$$
$$= -L_1 \cos(\alpha_1) + L_2 \cos(\alpha_2)$$
$$= -L_1 \cos(\theta_{1r}) + L_2 \cos(\theta_{2r}) \qquad (4.150)$$

where L_i is the magnitude of the phase center vector d_{PCi}, α_i is the angle between ℓ_i and d_{PCi}, and i is the satellite index.

In the real situation, the attitude quaternion observation may have a certain level of bias and noise with respect to the true attitude orientation. Additionally, the estimated phase center may be different from the true phase center.

Suppose the attitude quaternion observation q_i^{body} is related to the true attitude q_i as

$$\Re(q_i^{body}) = \Xi(\beta_{i1}, \beta_{i2}, \beta_{i3})\Re(q_i) \qquad (4.151)$$

and the estimated phase center is d_{ePCi}. The error of correction would then be

$$Err(\Delta) = -\ell_1 \cdot d_{PC1} + \ell_2 \cdot d_{PC2}$$
$$+ \ell_1 \Xi(-\beta_{11}, -\beta_{12}, -\beta_{13}) \cdot d_{ePC1} - \ell_2 \Xi(-\beta_{21}, -\beta_{22}, -\beta_{23}) \cdot d_{ePC2} \quad (4.152)$$

where $\ell_i \Xi(-\beta_{i1}, -\beta_{i2}, -\beta_{i3}) \cdot d_{ePCi}$ can be approximated as

$$\ell_i \Xi(-\beta_{i1}, -\beta_{i2}, -\beta_{i3}) \cdot d_{ePCi} \approx \ell_i (d_{ePCi} + \begin{bmatrix} 0 & \beta_{i3} & -\beta_{i2} \end{bmatrix} x_{ePCi} \quad (4.153)$$

Therefore

$$Err(\Delta) = \sum_{i=1}^{2} (-1)^i \ell_i \cdot (d_{PCi} - d_{ePCi}) - \sum_{i=1}^{2} (-1)^i \ell_i \cdot \begin{bmatrix} 0 & \beta_{i3} & -\beta_{i2} \end{bmatrix} x_{ePCi} \quad (4.154)$$

which can be roughly bounded by

$$Err(\Delta) < L \cdot |\theta_{er} \cdot AttBand| + 4L|\beta \cdot AttBand| \quad (4.155)$$

where L is about 1.4 meters, θ_{er} is the phase center boresight determination error, β represents the misalignment level (which is about 0.8 mrad) and *AttBand* represents the deadband of the attitude control, which is about 4 mrad in the current mission period.

Since the proof mass offset exists within a requirement of 0.1 mm, it will also affect this correction error. However, it is small enough to be neglected. A rough calculation shows that this effect is on the order of the product of the offset and the square of *AttBand*, which is far below $1\mu m$.

4.7 STAR CAMERA MISALIGNMENT ANALYSIS

As stated in Section 3.6.2, the observation of star camera 1 can be modeled as

$$\mathfrak{R}(q_1^{obs}) = R_n^1 R_{mis}^1 R_{BS}^1 \mathfrak{R}(q) \tag{4.156}$$

And the observation of star camera 2 can be modeled as

$$\mathfrak{R}(q_2^{obs}) = R_n^2 R_{mis}^2 R_{BS}^2 \mathfrak{R}(q) \tag{4.157}$$

The rotation matrices R_{mis}^1, R_n^1, R_{mis}^2 and R_n^2 are all small angular rotation matrices and anti-symmetrical.

Suppose

$$R_n^1 = \Xi(\varepsilon_1, \varepsilon_2, \varepsilon_3) \tag{4.158}$$
$$R_{mis}^1 = \Xi(\theta_1, \theta_2, \theta_3) \tag{4.159}$$
$$R_n^2 = \Xi(\alpha_1, \alpha_2, \alpha_3) \tag{4.160}$$
$$R_{mis}^2 = \Xi(\beta_1, \beta_2, \beta_3) \tag{4.161}$$

Combining the Equations (4.156) and (4.157) yield

$$R_n^1 R_{mis}^1 (R_{BS}^1 (R_{BS}^2)^{-1})(R_n^2 R_{mis}^2)^{-1} = \mathfrak{R}(q_1^{obs})\mathfrak{R}(q_2^{obs})^{-1} \tag{4.162}$$

There is a nice property about the small angular rotation matrix. That is, two continuous small angular rotations can be equivalent to one rotation with the rotation angles being the sum of the two small angular rotation angles. Therefore

$$R_n^2 R_{mis}^2 = \Xi(\alpha_1 + \beta_1, \alpha_2 + \beta_2, \alpha_3 + \beta_3) \tag{4.163}$$
$$R_n^1 R_{mis}^1 = \Xi(\varepsilon_1 + \theta_1, \varepsilon_2 + \theta_2, \varepsilon_3 + \theta_3) \tag{4.164}$$

Furthermore, the rotation matrix R_{BS}^1 and R_{BS}^2 are known and can be assumed to be fixed. Based on Equation (3.20), it has

131

$$R_{BS}^1 (R_{BS}^2)^{-1} = \begin{bmatrix} 1 & 0 & 0 \\ 0 & 0 & 1 \\ 0 & -1 & 0 \end{bmatrix} \tag{4.165}$$

Substituting Equations (4.163) through (4.165) into Equation (4.162) and ignoring the higher order small angle products yields

$$\begin{bmatrix} 1 & \varepsilon_2 + \theta_2 - \alpha_3 - \beta_3 & \varepsilon_3 + \theta_3 + \alpha_2 + \beta_2 \\ -\alpha_2 - \beta_2 - \varepsilon_3 - \theta_3 & \alpha_1 + \beta_1 - \varepsilon_1 - \theta_1 & 1 \\ \varepsilon_2 + \theta_2 - \alpha_3 - \beta_3 & -1 & \alpha_1 + \beta_1 - \varepsilon_1 - \theta_1 \end{bmatrix} = B \tag{4.166}$$

where

$$B = \Re(q_1^{obs})\Re(q_2^{obs})^{-1} \tag{4.167}$$

Given the quaternion observation data q_1^{obs} and q_2^{obs}, the average of B matrix, denoted by $\overline{B}$, is given as follows

$$\overline{B} = \frac{1}{m}\sum_{i=1}^{m}\Re(q_1^{obs}(t_i))\Re(q_2^{obs}(t_i))^{-1} \tag{4.168}$$

Assumed that $E(\varepsilon_i) = E(\alpha_i) = 0$, where $i = 1,2,3$, then we have

$$\theta_2 - \beta_3 = \overline{B}_{12} \tag{4.169}$$
$$\beta_2 + \theta_3 = \overline{B}_{13} \tag{4.170}$$
$$\beta_1 - \theta_1 = \overline{B}_{22} \tag{4.171}$$

From Equations (4.169) through (4.171), it can be seen that although the misalignment angles of each star camera cannot be determined by this approach, certain combination can. During the processing of real data, this set of equations

132

will be combined with the ACC observations and dual star cameras observations to determine each component of misalignment parameters of each star camera sensor.

The other way to look at the misalignment error is to observe the difference of the attitude quaternion of the satellite body-fixed frame obtained from two different star cameras.

The attitude quaternion of the satellite body-fixed frame obtained from star camera 1 is given by

$$\Re(q_1^{body}) = (R_{BS}^1)^{-1}\Re(q_1^{obs}) \tag{4.172}$$

Of course

$$\Re(q_2^{body}) = (R_{BS}^2)^{-1}\Re(q_2^{obs}) \tag{4.173}$$

Substituting Equation (4.156) into Equation (4.172) and ignoring the noise matrix yield

$$\Re(q_1^{body}) = (R_{BS}^1)^{-1} R_{mis}^1 R_{BS}^1 \Re(q) = M^{e1}\Re(q) \tag{4.174}$$

where

$$M^{e1} = \Xi(\theta_1,(\cos\theta)\theta_2 - (\sin\theta)\theta_3,(\cos\theta)\theta_3 + (\sin\theta)\theta_2) \tag{4.175}$$
$$\theta = -135° \tag{4.176}$$

In the following equations, $\theta = -135°$. On the other hand

$$\Re(q_2^{body}) = M^{e2}\Re(q) \tag{4.177}$$

133

where

$$M^{e2} = \Xi(\beta_1, (\cos\theta)\beta_2 + (\sin\theta)\beta_3, (\cos\theta)\beta_3 - (\sin\theta)\beta_2) \quad (4.178)$$

If we apply operator $\otimes$, defined in Appendix B, to quaternion q, q'', q' as follows, we obtain

$$q = q'' \otimes q' \quad (4.179)$$

The result can be written as

$$q = \begin{bmatrix} q_4'' & q_3'' & -q_2'' & q_1'' \\ -q_3'' & q_4'' & q_1'' & q_2'' \\ q_2'' & -q_1'' & q_4'' & q_3'' \\ -q_1'' & -q_2'' & -q_3'' & q_4'' \end{bmatrix} q' = \aleph(q'')q' \quad (4.180)$$

Note there is another operator $\aleph()$ defined in the above equation.

Furthermore, from the property described by Equation (B.9), it can be easily seen that

$$\Xi(\theta_1, \theta_2, \theta_3) \approx \Re(\frac{\theta_1}{2}, \frac{\theta_2}{2}, \frac{\theta_3}{2}, 1) \quad (4.181)$$

Therefore

$$q_1^{body} - q_2^{body} = [\aleph(q_{err}^1) - \aleph(q_{err}^2)]q \quad (4.182)$$

where

$$q_{err}^1 \approx (\theta_1/2, [(\cos\theta)\theta_2 - (\sin\theta)\theta_3]/2, [(\cos\theta)\theta_3 + (\sin\theta)\theta_2)]/2, 1) \quad (4.183)$$
$$q_{err}^2 \approx (\beta_1/2, [(\cos\theta)\beta_2 + (\sin\theta)\beta_3]/2, [(\cos\theta)\beta_3 - (\sin\theta)\beta_2)]/2, 1) \quad (4.184)$$

Due to the un-normalized quaternion, the above Equations (4.181), (4.183) and (4.184) use approximate equalities instead of a strict equality.

Since $|q| = 1$, it has

$$| q_1^{body} - q_2^{body} | < \frac{1}{2}(\sum_{i=1}^{3}(|\theta_i| + |\beta_i|)) \qquad (4.185)$$

which will be called the boundary condition for the quaternion difference due to the misalignment. If the observation noise matrix is taken into account, then

$$| q_1^{body} - q_2^{body} | < \frac{1}{2}(\sum_{i=1}^{3}(|\theta_i| + |\beta_i| + |\alpha_i| + |\varepsilon_i|)) \qquad (4.186)$$

This is the instantaneous boundary for the difference of the quaternions.

Chapter 5: Calibration Simulations

5.1 INTRODUCTION

In the previous chapters, the maneuver designs, required observation instruments, instrument simulation models and data processing algorithms for both COM calibration and KBR calibration are explored. The maneuver designs outline the procedures for the AOCS system to control the satellites during the calibration maneuvers. The instruments required to collect the data are also specified. For simulation purpose, the instrument observation models are established. The data processing algorithms are proposed to process not only the simulation data, but also the real calibration data.

Complete simulations will be carried out in the following sections. From the simulations and analyses, the maneuver parameters will be determined for the real mission. Based on simulations with the designed parameters, it can be seen that the COM calibration and KBR calibration determination accuracies can meet the instrument validation requirements. The center of mass calibration is dependent on the geographic location. The estimation accuracy is dependent on the calibration location over the Earth, as is indicated by the optimal location criterion. The optimal location will be determined by the following simulations. Two calibration maneuvers are designed for KBR calibration. By comparison of the calibration accuracies in the simulations, the periodic oscillation maneuver is chosen for the real mission. The star camera misalignment determination

simulations are also performed. Additionally, the assumptions made in developing the estimation algorithms will be verified by the simulations.

5.2 CENTER OF MASS CALIBRATION

Two polar, near circular orbits with an altitude of 500 km, e.g., typical orbits for the initial GRACE satellites, are used in the simulations. Since the GRACE center of mass calibration can be carried out for each satellite individually, most of the following descriptions are with regard to one satellite. Simulations are made for both satellites in this research.

There were a number of simulations conducted. In each simulation, the true orbits and attitudes of each GRACE satellite are generated from the thirteen-dimension dynamic model described by Equation (2.30). The orbit perturbations and environmental torques described in Chapter 2 are applied during the integration. In addition to the translational state vector, the angular acceleration $\dot{\omega}$, non-gravitational acceleration $\vec{f}_{ng}$ and the Earth's magnetic flux density B are also determined at each integration step. Using these data, the observation data from the accelerometer, star camera and magnetometer are obtained based on the corresponding instrument simulation model. The data rates of the observation data are 10 Hz, 1 Hz and 0.1 Hz, respectively. The data preprocessing algorithms can be applied to star camera data and the magnetometer data to obtain derived observation data with rate of 10 Hz. The algorithms ASSEST, ASCFEST, ASCREST can then be used to estimate the proof mass offset.

The applied orbit perturbations and external torques, used to generate the real orbit and attitude, are summarized in Table 5.1 (Bettadpur, 2001).

137

Table 5.1   Orbit Perturbations and External Torques

Gravitational Forces		
Category	*Model*	*Parameters*
Spherical Harmonics	EGM96	COM Cal 20×20 KBR Cal 90×90

Non-Gravitational Forces		
Category	*Model*	*Parameters*
Atmospheric Drag	Trapezoid Area Model Density: DTM plus Short Variations Winds: HWM93	$C_d = 0.2 \qquad K_p = 2.5$ $F_{10.7} = 184 \quad m = 420\,\mathrm{Kg}$
Solar Radiation Pressure	Trapezoid Area Model Flux/Reflectivity	$\eta = 0.5$
Earth Radiation Pressure	Trapezoid Area Model Albedo/Emissivity	$\eta_e = 0.5\,, a_0 = 0.34\,, c_0 = 0.\,,$ $c_1 = 0.1\,, c_2 = 0.\,, a_2 = 0.29\,,$ $e_0 = 0.68\,, k_0 = 0.\,, k_1 = -0.07\,,$ $k_2 = 0.\,, e_2 = -0.18$

Gravitational Torques		
Category	*Model*	*Parameters(Kgm^2)*
Spherical Harmonics	Spherical Mass	$I_{xx} = 80, I_{xy} = -3, I_{xz} = -3$ $I_{yy} = 420, I_{yz} = -0.3, I_{zz} = 470$

Environmental Torques		
Category	*Model*	*Remarks*
Atmospheric Drag	Trapezoid Area Model Density: DTM plus Short Variations Winds: HWM93	From programs coded at AMA/LaRC
Solar Radiation Pressure	Trapezoid Area Model Flux/Reflectivity	

Active Torques		
Category	*Model*	*Remarks*
Magnetic Torque	-Spherical harmonic model -IGRF 95 Gaussian coefficients	Operated in both KBR and COM calibrations
Thruster Torque	In Section 2.4.1.4	Operated only in KBR calibration

5.2.1 Assumptions and Verification

As pointed out in the previous chapters, several assumptions are made to develop the estimation algorithms for center of mass calibration. The main assumptions are summarized as follows.

Assumption 1: The non-gravitational accelerations are flat compared to the high frequency angular motion related acceleration, and they can be approximated by a linear function during the center of mass calibration period.

Assumption 2: The angular motion related acceleration (a_{acc} and a_{vel}) is the dominating periodic disturbance acceleration in the accelerometer observation, especially a_{acc}. All the other disturbance accelerations can be approximated by a linear term.

Assumption 3: The magnetic torque dominates over the environmental torques in the center of mass calibration. As a matter of fact, the largest torque during the nominal phase is the thruster torque. However, the thruster torque is not applied during the COM calibration.

Assumption 4: The satellite angular rotation about any axis satisfies the angular motion requirement of the star camera, which allows the optimum resolution and accuracy of the star cameras observation.

Simulations have been done to verify the assumptions summarized above. As stated before, there are several approaches to produce the active magnetic torque. In the following simulations, commanding a sine magnetic moment (denoted by *Sin M*), commanding waveform magnetic moment (denoted by *Wav M*) and commanding expected torque along roll/pitch/yaw axis (denoted by *Roll*

T, *Pitch T*, *Yaw T*, respectively) are simulated based upon Section 3.4. In each case, the period of the magnetic torque is 12 seconds, the calibration time span is 3 minutes, the calibration location is over the Earth's equator, and the proof mass offset is assumed on the order of ~mm. These parameters are used in the real COM calibration. Figures are presented to illustrate the common phenomena appearing in the center of mass calibration. For simplicity, the figures depict only GRACE A. In fact, exactly the same pattern and conclusions can be found for GRACE B. Some figures only plot data for one minute for better illustration purpose.

Figure 5.1 (Figure 5.1 (a), Figure 5.1 (b)) shows the non-gravitational acceleration a_{ng}, including the atmosphere drag, solar radiation pressure (denoted by SRP) and Earth radiation pressure (denoted by ERP). It can be seen that a_{ng} could be fitted by a linear function, although not perfectly, especially along the roll axis. The main source that causes the non-perfect linear function fitting is the short period atmospheric density variations, which may be too pessimistic in the simulations. Still, a_{ng} is quite flat considering that the period of active torque is 12 seconds. This confirms Assumption 1.

The angular acceleration induced disturbance acceleration a_{acc}, angular velocity induced disturbance acceleration a_{vel} and the gravity gradient induced disturbance acceleration gg are shown in Figure 5.2 (Figure 5.2 (a), Figure 5.2 (b)). Obviously, the angular motion related acceleration (a_{acc} and a_{vel}), especially a_{acc}, is the dominating periodic disturbance acceleration. The

141

acceleration gg can be linearly approximated. This typical figure gives effective support of Assumption 2.

Figure 5.3 (Figure 5.3 (a), Figure 5.3 (b)) shows the magnetic torque, aerodynamic torque, solar radiation torque and gravitational torque. The domination of the magnetic torque over the environmental torque is very obvious and appears quite reasonable from the AOCS point of view. This figure is a clear proof of Assumption 3.

The angular velocity $\omega(t)$ in the calibration history is shown in Figure 5.4, from which it can be seen that the angular rotation about any axis does not exceed a value of $0.1^{\circ}/s$, which is required for the star cameras to obtain the optimum resolution and accuracy. Therefore, the observation data from the star camera can be used in determining the proof mass offset. There confirms that Assumption 4 is valid.
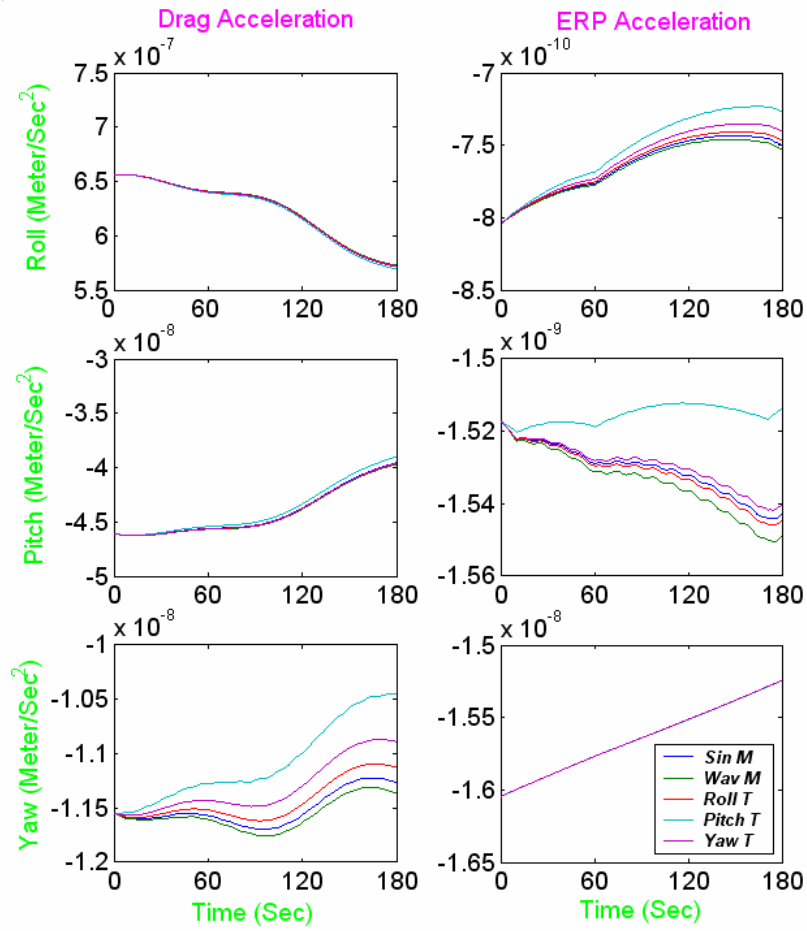
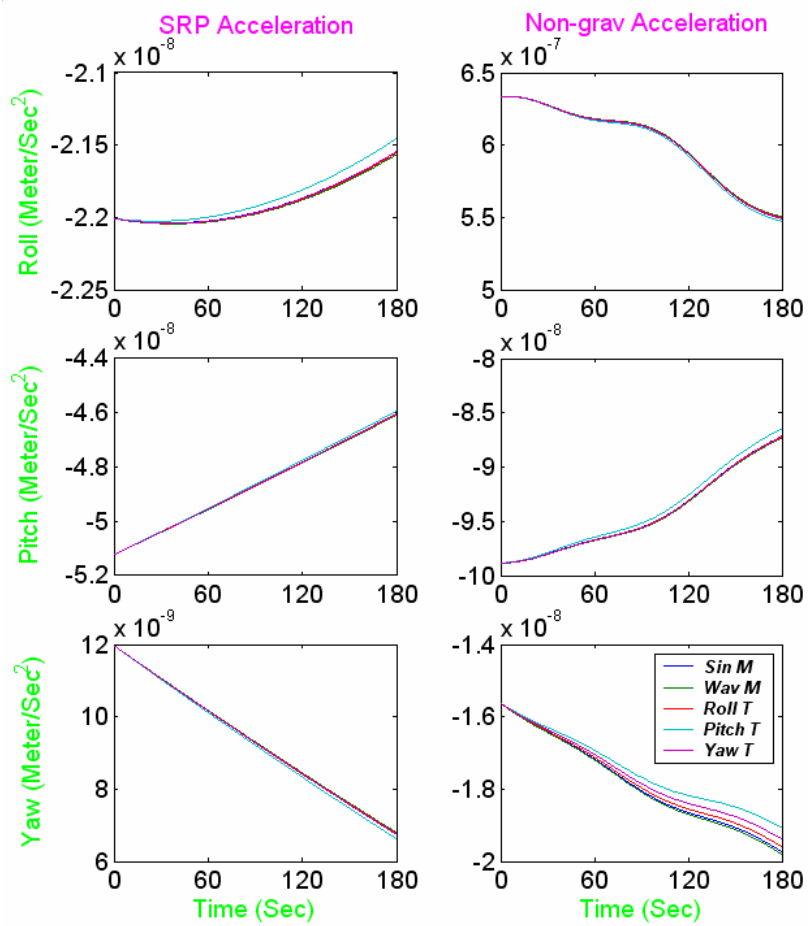Figure 5.1 (a) Non-gravitational Accelerations on GRACE A

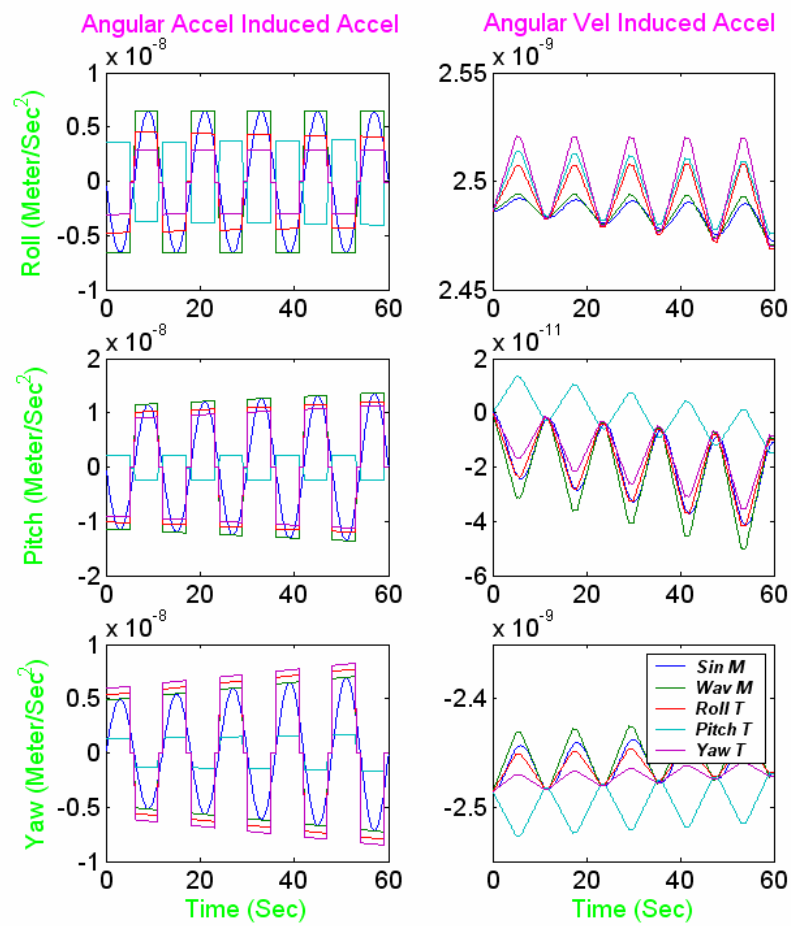Figure 5.1 (b) Non-gravitational Accelerations on GRACE A
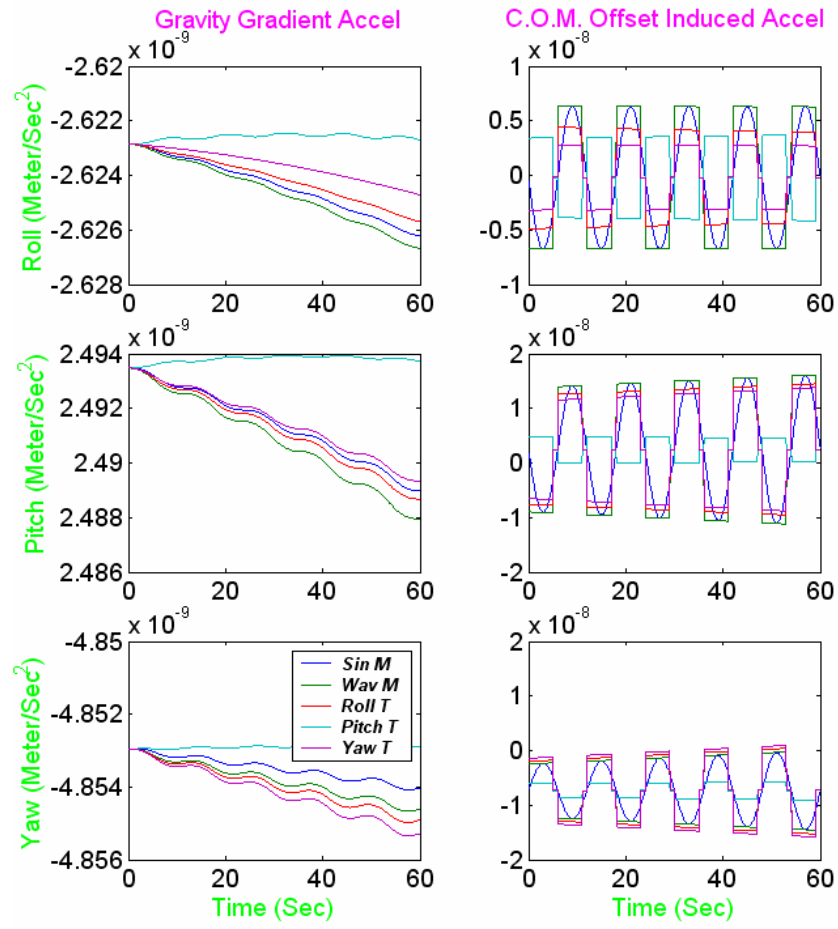
Figure 5.2 (a) Disturbance Accelerations on GRACE A

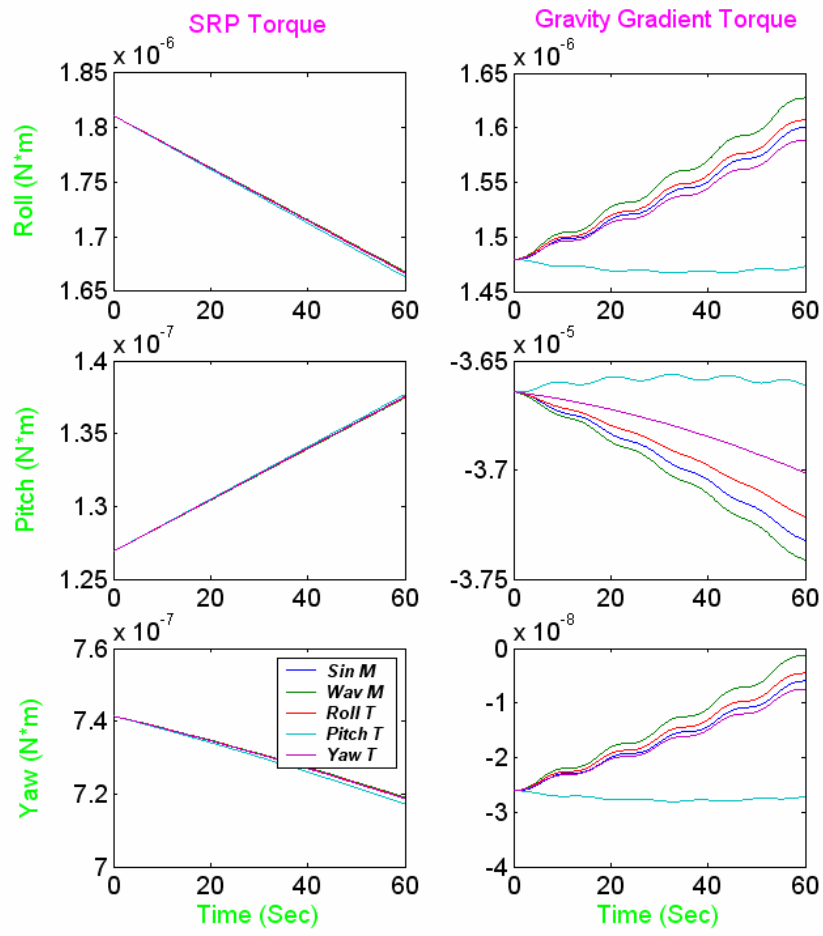Figure 5.2 (b) Disturbance Accelerations on GRACE A
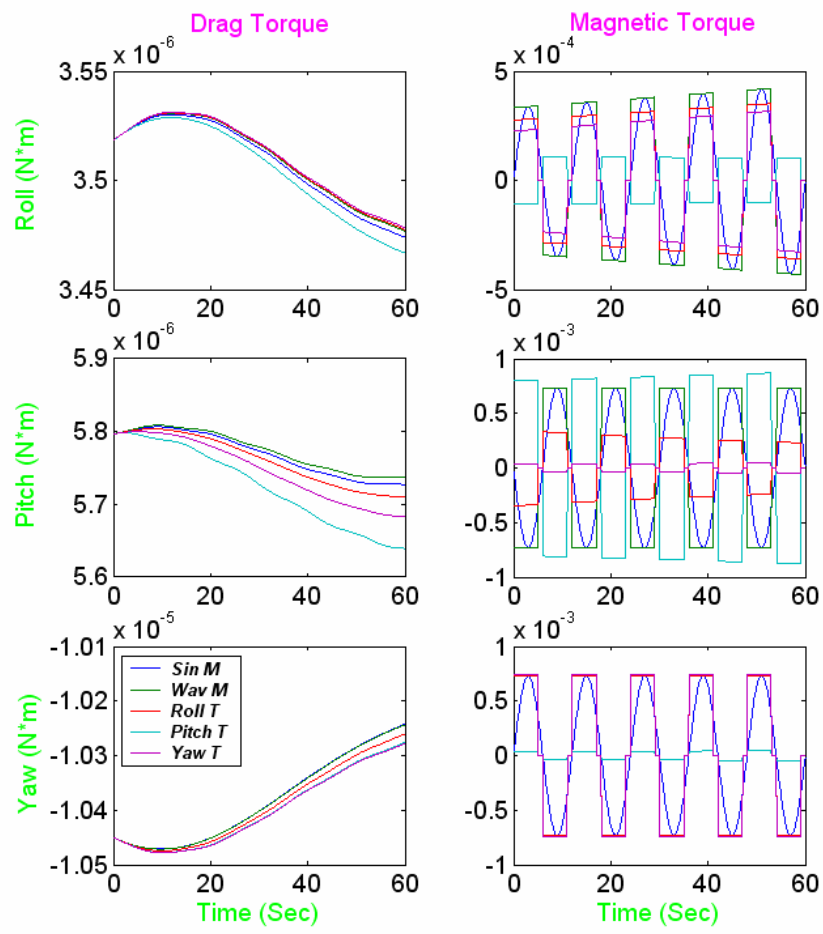
Figure 5.3 (a) External Torques on GRACE A

147

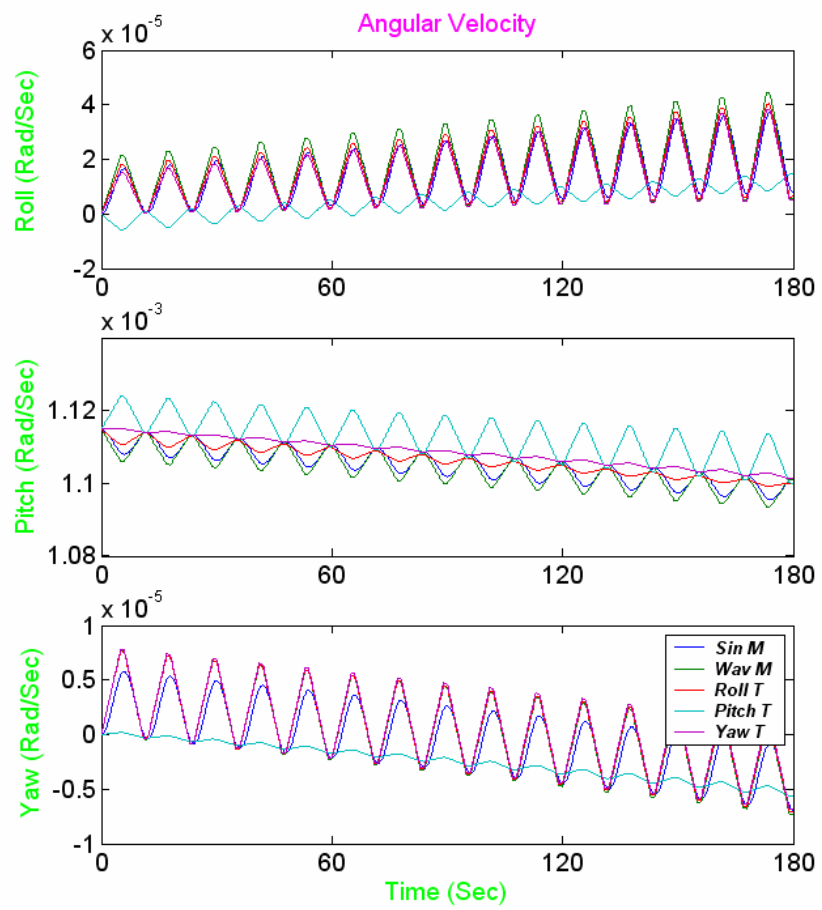Figure 5.3 (b) External Torques on GRACE A

Figure 5.4 Angular Motions on GRACE A

5.2.2 Location Variation Analysis and Optimal Location

Since the profile of the Earth's magnetic field cannot be changed and it varies with the geographic location, the resultant magnetic torque, which is the mathematical cross product of the magnetic moment and the Earth's magnetic flux density, can be quite different over the global scale of the Earth. Hence, the angular acceleration during the center of mass calibration is highly dependent on the satellite location over the Earth. Recalled from Section 4.2.6, the covariance of the proof mass offset estimate along each axis is dependent on the angular acceleration along this axis. The optimal location criterion states that it is preferred that the angular acceleration during the calibration is large enough and also is of the same order along each axis.

In order to globally view the angular acceleration profile in the center of mass calibration, the angular acceleration distribution functions are defined for commanding torque cases.

When commanding a torque along roll axis, the distribution function is defined by

$$DF(x) = \frac{(|\dot{\omega}_x| - |\dot{\omega}_y|)^2 + (|\dot{\omega}_x| - |\dot{\omega}_z|)^2}{\dot{\omega}_x^2} \tag{5.1}$$

where $\dot{\omega}_x, \dot{\omega}_y, \dot{\omega}_z$ are the angular acceleration along the roll, pitch, and yaw axis, respectively. A small value of this distribution function implies that the angular acceleration along each axis is of the same order and the magnitude of angular acceleration is large.

Likewise, the distribution function

$$DF(y) = \frac{(|\dot{\omega}_y| - |\dot{\omega}_x|)^2 + (|\dot{\omega}_y| - |\dot{\omega}_z|)^2}{\dot{\omega}_y^2} \qquad (5.2)$$

is defined for the pitch maneuver and

$$DF(z) = \frac{(|\dot{\omega}_z| - |\dot{\omega}_x|)^2 + (|\dot{\omega}_z| - |\dot{\omega}_y|)^2}{\dot{\omega}_z^2} \qquad (5.3)$$

is defined for the yaw maneuver.

Figure 5.5, Figure 5.6 and Figure 5.7 show the angular acceleration distribution function over the global scale of the Earth when the roll maneuver, pitch maneuver and yaw maneuver are performed. For better illustration, the distribution function value is set to ten when it is above this value. It can be seen that the distribution function is small over the Earth's equator for all three cases. Particularly, the roll and pitch maneuvers over the Earth's equator have very small distribution function value. Therefore, it is expected this region leads to good proof mass offset determination simply by one single calibration maneuver. This will be demonstrated by the simulations in the later sections.

Therefore, the optimal timing to carry out the center of mass calibration is to perform roll maneuver and pitch maneuver when the satellite is over the Earth's equator. In this way, one single calibration maneuver allows the accurate determination of the proof mass offset along each coordinate axis.
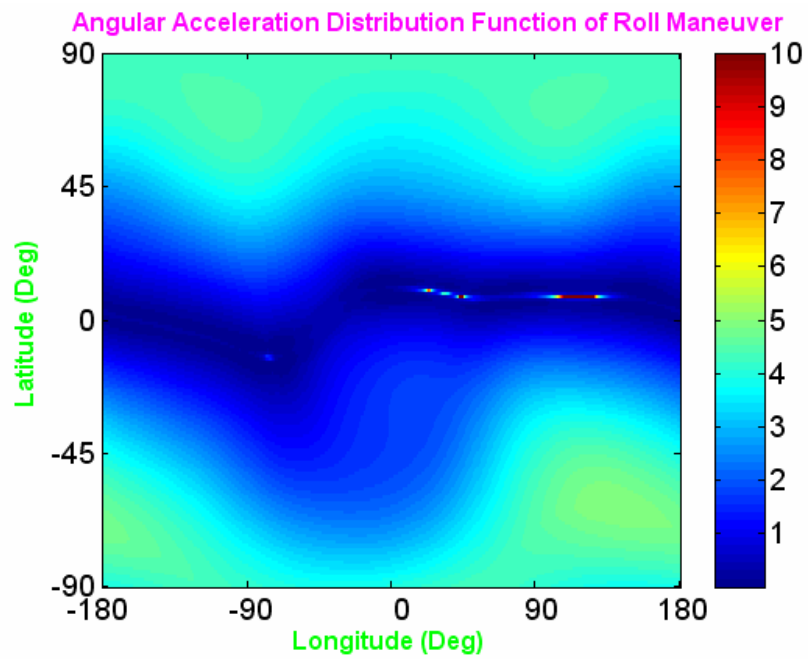
151

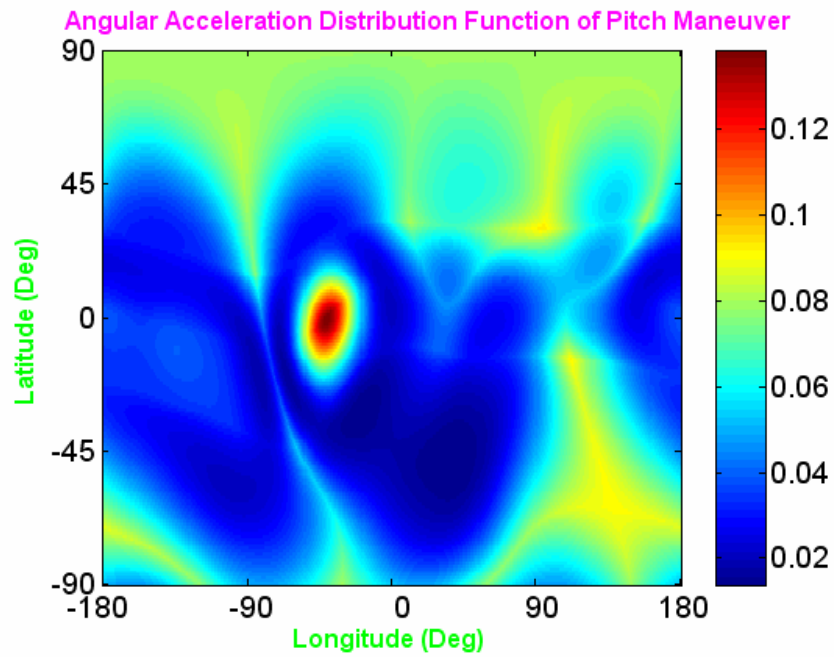Figure 5.5   The Distribution Function DF(x) of the Roll Maneuver

Figure 5.6   The Distribution Function DF(y) of the Pitch Maneuver
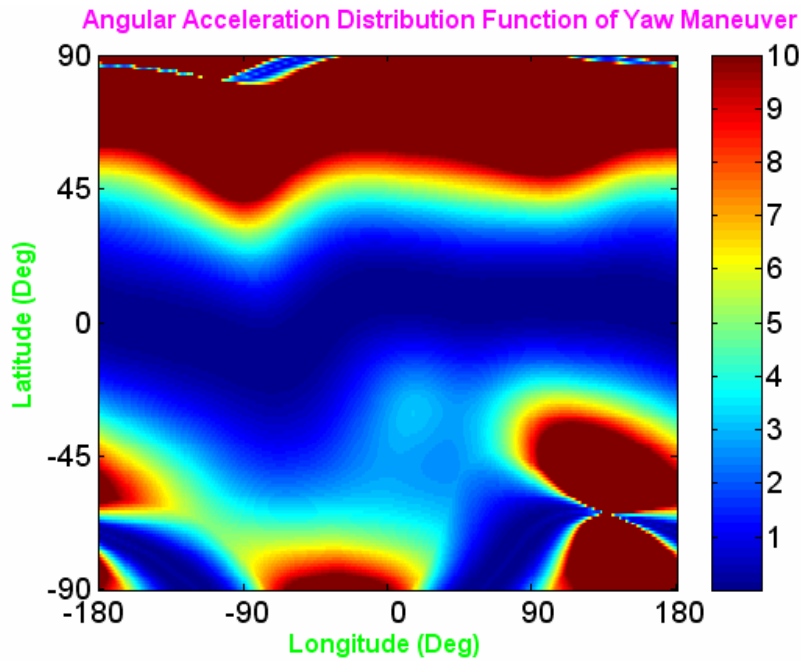
152

Figure 5.7   The Distribution Function DF(z) of the Yaw Maneuver

5.2.3 Simulation Results and Analyses

Since the center of mass calibration of the two GRACE satellites does not affect each other, the maneuver can be performed individually or at the same time. For simulation simplicity, the center of mass calibrations are operated simultaneously for the two satellites in this study. Following the simulation procedure, a variety of simulation cases are investigated to observe the corresponding calibration accuracy. These preliminary simulations provide valuable suggestions for the real calibration preformed after the launch of the GRACE satellites.

There are two different locations under test, one is over the Earth's equator, and the other is over the Earth's north pole. In each case, commanding a

153

sine magnetic moment, commanding a waveform magnetic moment and commanding an expected torque along roll/pitch/yaw axis are simulated. The torque period has been tested for 12 seconds, denoted by Period 12sec, for 32 seconds, denoted by Period 32sec, and 62 seconds, denoted by Period 62sec. The calibration time span has been tested for 1 minute, 3 minutes, 5 minutes and 10 minutes. In addition, the proof mass offset values have been tested for two sets of values, one represents the large offset, $d = \begin{bmatrix} 2.0 & -2.0 & 2.0 \end{bmatrix} mm$, and the other one represents the small offset, i.e., the result from first iteration of calibration with large offset, $d = \begin{bmatrix} 0.2 & 0.2 & -0.2 \end{bmatrix} mm$. The simulation parameter variations are summarized in Table 5.2.

Table 5.2   COM Calibration Test Parameter Variations

COM Calibration Simulation Parameters	
Category	*Parameters*
Location	- Over the Equator - Over the North Pole
Magnetic Torque	- Commanding Sine Magnetic Moment - Commanding Waveform Magnetic Moment - Roll Maneuver; Pitch Maneuver; Yaw Maneuver
Torque Period	- 12 Seconds; 32 Seconds; 62 Seconds
Duration	- 1 Min; 3 Mins; 5 Mins; 10 Mins
Offset	- Large ~ 2MM; Small ~0.2 MM

Using the combination of these parameters, various simulations have been performed. For each specific test case, simulations are done for five times based on the same instrument observation characteristics, but different values of observation noises. Then the root mean square of the determination errors of these

five simulations is used to represent the proof mass offset determination error for this test case.

The observation data of each specific test case can be processed individually using the estimation algorithms proposed in Chapter 4. The estimation error of every single maneuver is quite consistent with the location variation analysis and optimal location criterion. The estimation results are shown in Figures 5.8 through 5.11. In fact, the calibration data from multiple maneuvers can also be combined together to determine the proof mass offset. In the calibration simulation, the observation data from four maneuvers, roll maneuver over pole, pitch maneuver over pole, yaw maneuver over equator and pitch maneuver over equator, is the exact same combination used in the real calibration, where all are processed together. The estimation algorithms are slightly different from what are applied to a single maneuver. The differences are explained in Section 6.2.2 in detail. Figure 5.12 and Figure 5.13 show the determination accuracy of these multiple maneuver processing.

Figures 5.8 through 5.11 show the estimation errors for all single maneuver simulation cases. Again, these figures only depict GRACE A. In fact, exactly the same pattern and conclusions can be found for GRACE B. In these figures, the red dashed line, parallel to the horizontal axis, represents the proof mass offset requirement, which is 0.1 mm. The error values are bounded by 2 mm when they exceed this value. This is not only for better illustration purpose but also because the MTM system can only balance the proof mass offset within 2 mm. Any maneuver that has all three components of proof mass offset

155

determination error below the red dashed line is a good candidate for the real mission.

From the optimal timing analysis, the center of mass calibration should be done over the Earth's equator with roll and pitch maneuvers. The first two subplots from the top of Figure 5.8 and Figure 5.9 represent this optimal timing case. It can be seen that calibrations yield good accuracy with the torque period of 12 seconds. The determination error of these cases with this period can be less than the requirement of 0.1 mm along all three axes. In general, short torque period case yields better estimation in the same time span than longer torque period calibration. In addition, it can be seen that commanding the sine and waveform magnetic moments can also yield good estimates, which are even better than the roll maneuver and pitch maneuver. However, in the real mission, the commanded torque is selected, based on a simple mechanization requirement.

When the calibration is done over the Earth's north pole, as illustrated by Figures 5.10 and 5.11, most of the estimates are bad. In general, angular acceleration along roll axis is much larger than along pitch and yaw axes and the estimation accuracy along the roll axis is poor. This is consistent with the covariance analysis in Section 4.2.6.

Figure 5.12 and Figure 5.13 show the determination accuracy of the multiple maneuvers processing with large offset and small offset. Again, the red dashed line, parallel to the horizontal axis, represents the 0.1 mm proof mass offset requirement. From these figures, it can be seen that the data processing with multiple maneuvers is quite stable with respect to the calibration duration. As

long as the duration is longer than 3 minutes, the determination results are quite close. In addition, these figures shows that the proof mass offset along the roll axis is the most poorly determined, whereas the pitch axis it can be determined very well. Overall, all three axes can be determined much better than 0.1 mm.
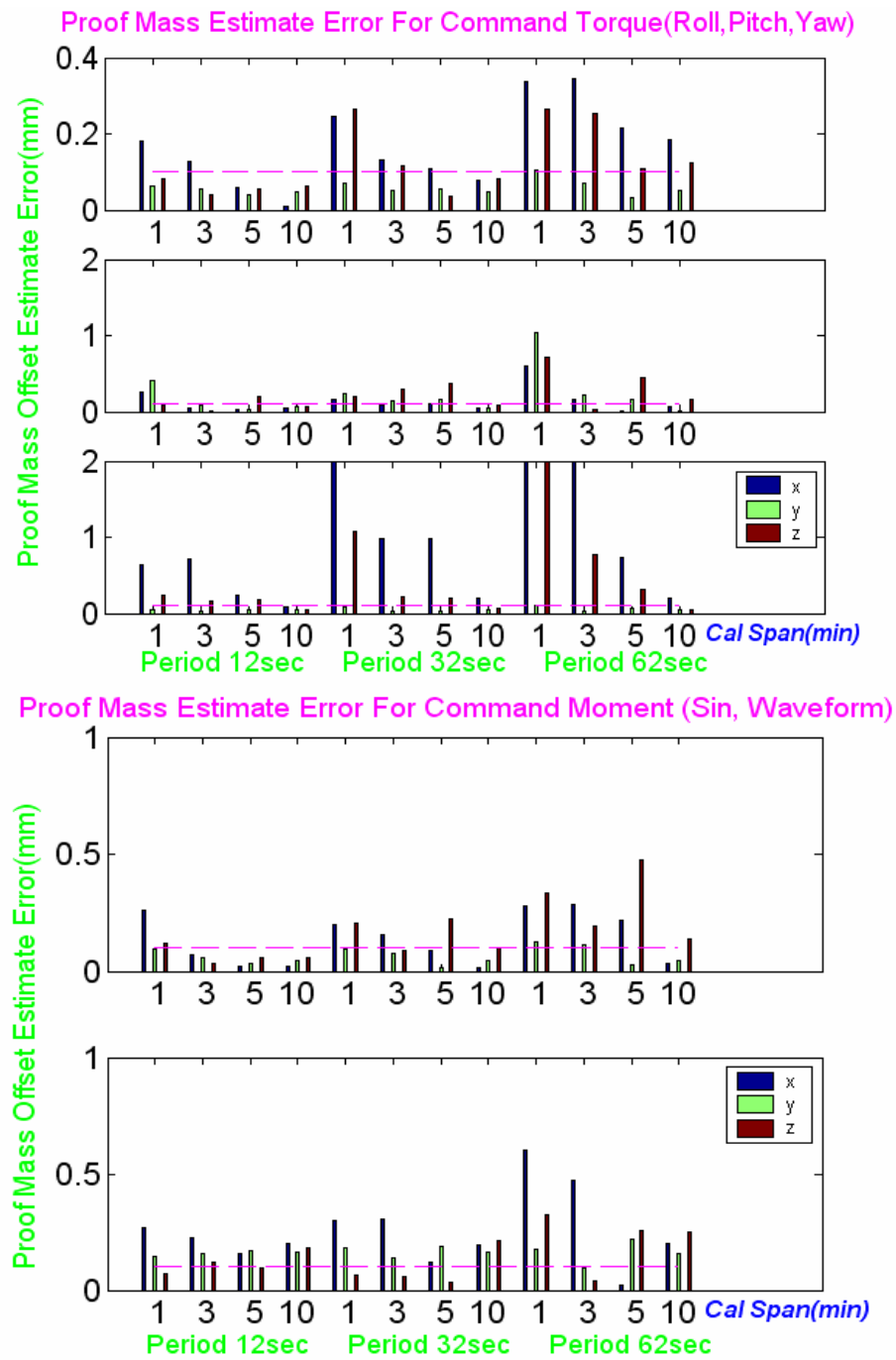
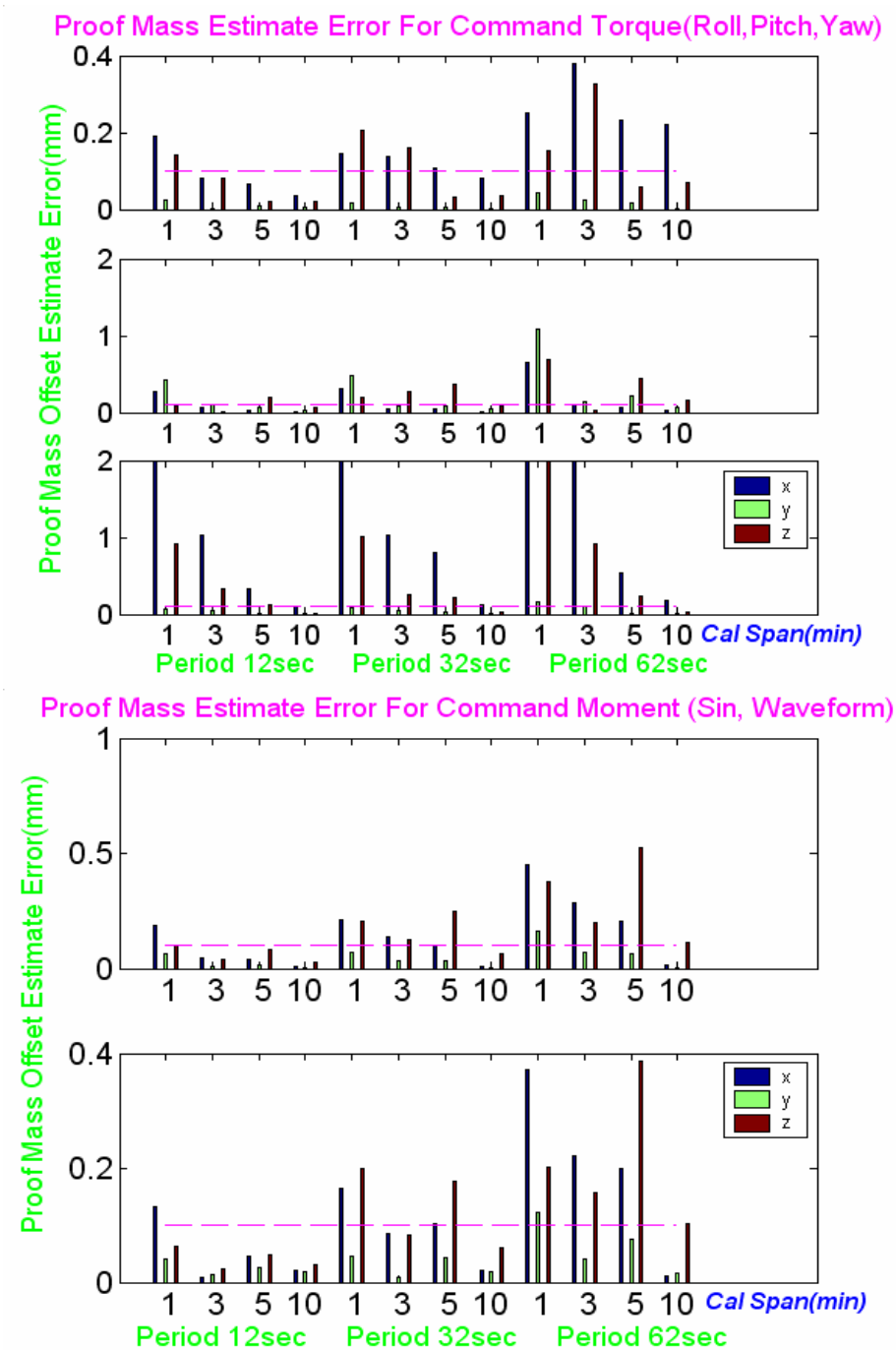Figure 5.8   Simulation with Large Offset Over Equator for GRACE A

Figure 5.9   Simulation with Small Offset over Equator for GRACE A

159
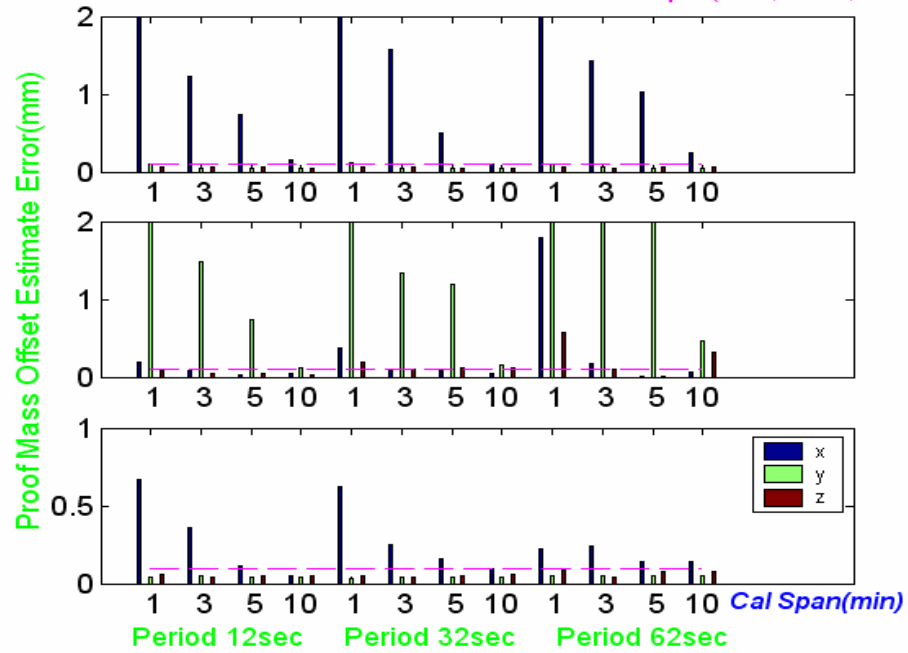
Figure 5.10 Simulation with Large Offset over Pole for GRACE A

Figure 5.11   Simulation with Small Offset over Pole for GRACE A

Figure 5.12   Multiple Maneuvers with Large Offset for GRACE A

Figure 5.13   Multiple Maneuvers with Small Offset for GRACE A

162

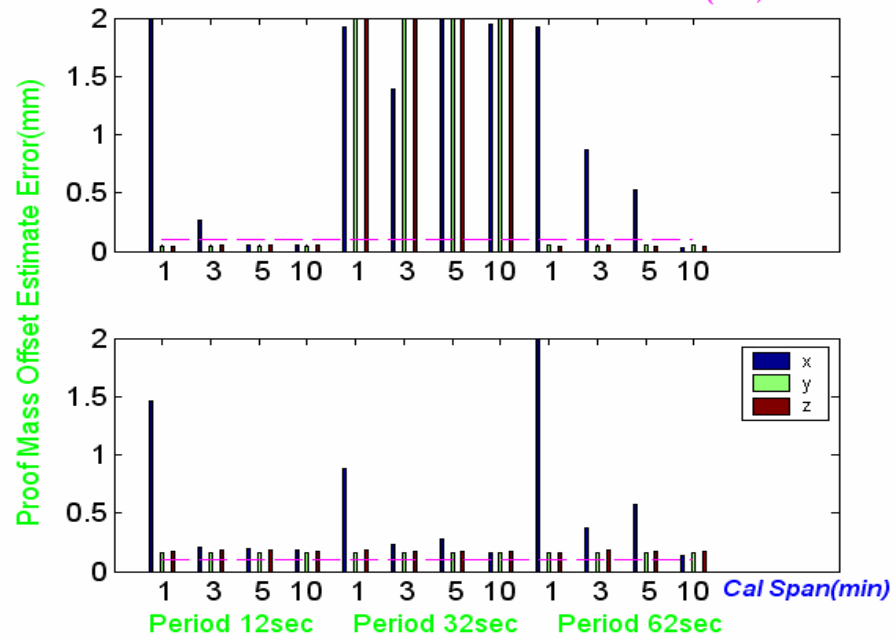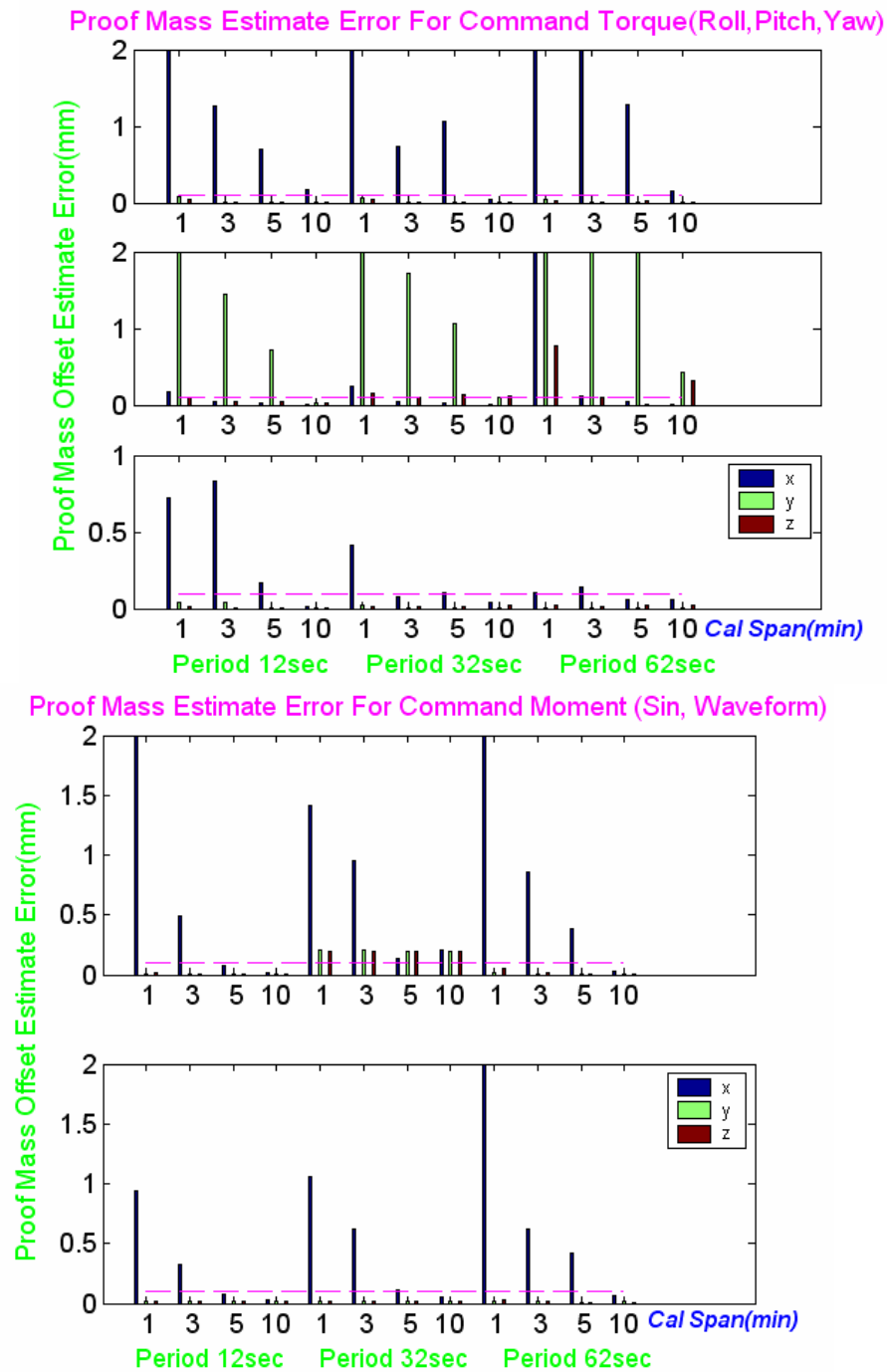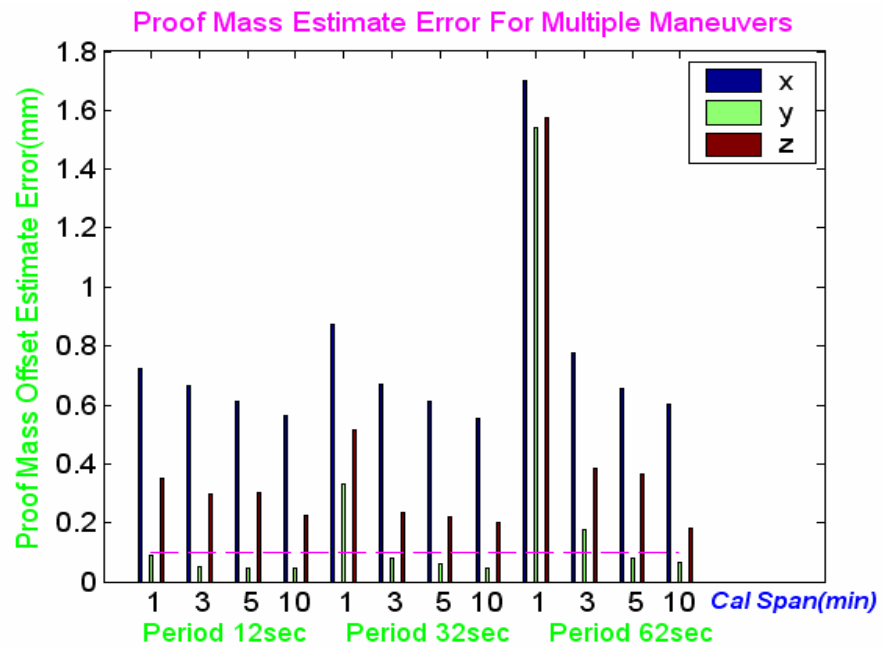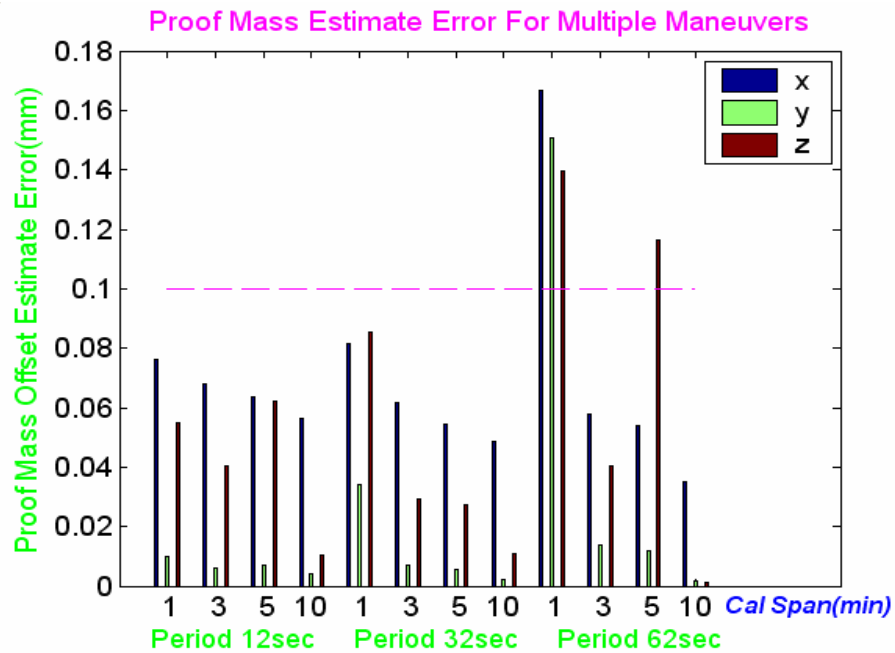### 5.2.4 COM Calibration Parameters for Real Mission

The simulation results and analyses in the previous section show that the proof mass offset can be well determined by both individual processing, referred to as "single maneuver processing", and by joint processing, referred to as "multiple maneuver processing". The calibration parameters and expected determination accuracy of each processing approach are displayed in Table 5.3 for the real mission.

Table 5.3 The COM Calibration Parameters Design

Real COM Calibration Parameters	
Single Maneuver Processing	
Location	- Over the Equator
Magnetic Torque	- Roll Maneuver - Pitch Maneuver
Torque Period	- 12 Seconds
Duration	- 3 Mins
Pessimistically Expected Accuracy	- By averaging estimation results of both maneuvers, all three axes are expected ~0.05mm
Multiple Maneuver Processing	
Magnetic Torque	- Roll Maneuver over Pole - Pitch Maneuver over Pole - Yaw Maneuver over Equator - Pitch Maneuver over Equator
Torque Period	- 12 Seconds
Duration	- 3 Mins
Pessimistically Expected Accuracy	- Expected that ~0.07mm along roll, ~0.01mm along pitch, ~0.04mm along yaw axis

5.2.5 Main Error Sources of COM Calibration

There are a number of error sources which affect the estimation results. These include the accelerometer observation noise (denoted by ACC), star camera observation noise (denoted by SCA), magnetometer measurement noise (denoted by MAG), moment of inertia error (denoted by MoI), and the non-linearity of the non-gravitational accelerations when treated as linear function (denoted by NoG).

In this study, single maneuver processing is used to test the effects of error sources. These same effects can also be found in multiple maneuver processing. Simulations of small offset over the Earth's equator of GRACE A with ASCFEST algorithm have been carried out. In each simulation, one error source has been deactivated. Suppose the estimate error of proof mass offset with all noises is d_{all}, and the estimate error when one certain error source is deactivated is d_{est}, Figure 5.14 shows the magnitude of $|d_{all} - d_{est}|$. So the large bar represents a large error source deactivated. It can be seen that the accelerometer noise and magnetometer measurement noise are two largest error sources.
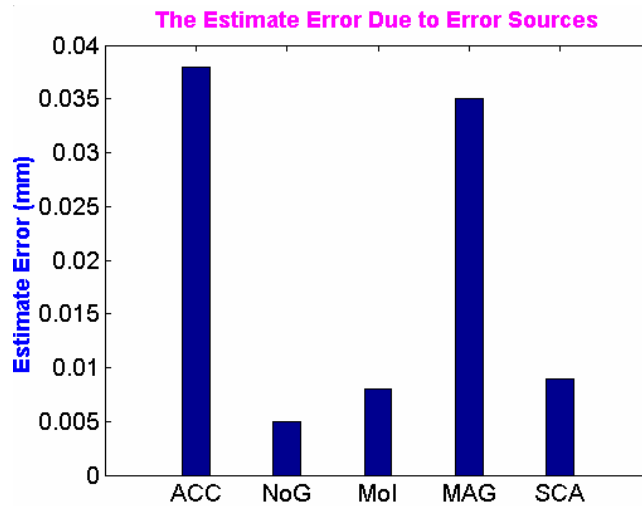
Figure 5.14   Estimation Accuracy with respect to Various Error Sources

5.2.6 Impact of Loss of Magnetometer Data

As mentioned before, the magnetometer could be in a failure mode during the GRACE mission lifetime. In this case, a spherical harmonic model of the Earth's magnetic field will be used to create the magnetic field data. Given the satellite position, determined highly accurately from GPS observations, the satellite attitude orientation, determined from the star cameras, and IGRF gaussian coefficients, the Earth magnetic field model can be used to produce the Earth magnetic field data.

The spherical harmonic model can only represent the main field of the Earth's magnetic field. In fact, there are a number of perturbations which influence this model. The primary source of geomagnetic field perturbations is the Sun. The Sun constantly emits a neutral plasma called solar wind, which compresses the field ahead of it until the plasma energy density equals the

165

magnetic field energy density at a distance of about 10 Earth radii. Although the solar wind is fairly constant, it is frequently augmented by energetic bursts of plasma emitted by solar flares. When this plasma encounters the geomagnetic field, it compresses the field further giving a rise in field intensity on the surface of the Earth. This causes a magnetic storm (Campbell, 1997). The geomagnetic field is monitored continuously at a series of magnetic observatories, which report the observed magnetic activity as an index K. These values can be averaged to obtain the planetary index, Kp. The magnetic field deviation can be roughly obtained as

$$\Delta B(nT) = 4\exp((Kp + 1.6)/1.75) \qquad (5.4)$$

Substituting Kp with value of 2.5 in the above equation, and considering other perturbations such as polar electrojet and the equatorial electrojet, the magnetic flux density deviation along each axis is assumed to be 150 nT as the spherical harmonics model error, which will be used to simulate the impact on the estimation if magnetometer is in failure.

The simulation of commanding sine magnetic moment with small proof mass offset during flight that is near to the Earth's equator has been performed. The same determination pattern can be found in other processing cases. The proof mass offset determination error is shown in Figure 5.15, from which it can be seen that the impact on the estimation accuracy is small. It is expected that the proof mass offset determination, with the loss of magnetometer data, can still be much better than 0.1 mm along each axis.

166
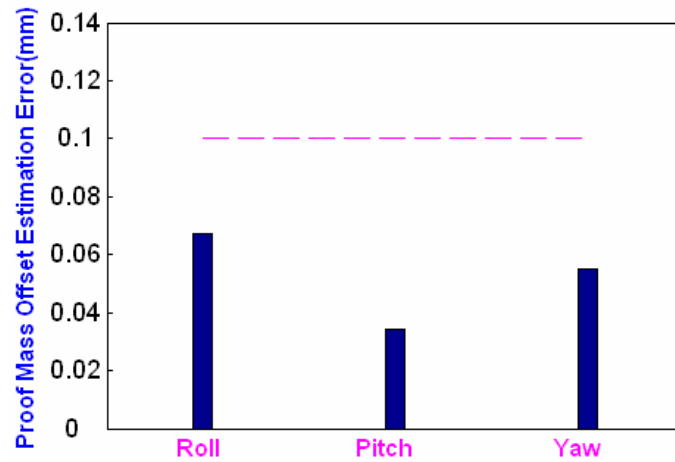
Figure 5.15   Loss of Magnetometer Simulations

5.3 KBR CALIBRATION WITH LINEARLY DRIFTING MANEUVER

The K-band ranging system calibration with linearly drifting maneuver is based upon the experimental techniques of phase center determination in electrical engineering (IEEE, 1979). The antenna under test is rotated in a manner to induce the phase change, which allows the numerical determination the phase center of the antenna under test. In fact, the linearly drifting maneuver design satisfies the phase center determination arrangement shown in Figure 1.3.

As pointed out before, since the phase centers of the two GRACE antennas are highly correlated in the range observation, four separate K-band ranging system calibration sub-maneuvers are implemented to overcome this correlation problem. While processing the observation data, all the data from four sub-maneuvers need to be combined together to determine the estimate of the phase centers of the GRACE K-band horns.

167

Although the GRACE KBR calibration in the real mission uses the periodic oscillation maneuver instead of the linearly drifting maneuver, this maneuver still deserves consideration for comparison and possible future mission use.

In the simulations, the initial orbits and attitudes of GRACE satellites are the same as in center of mass calibration. The perturbations and external torques are described in Table 5.1. After integrating the dynamic model, the KBR range rate data, star camera data, magnetometer observation data and POD from the GPS observations can be simulated. With preprocessed star camera data, magnetometer data and the POD data, algorithms KSSEST and KSCFEST can be used to estimate the KBR antenna phase centers.

5.3.1 Simulation Results and Analyses

Four sub-maneuvers and their mirror sub-maneuvers are simulated. There are two simulation cases under investigation, one is to simulate a maneuver near the equator, and the other is to simulate a maneuver near the north pole. This is to test the correlation of the estimation accuracy with the location. In the simulations, the phase center of GRACE A in the satellite body-fixed frame is assumed as $d_{pc1} = [1.4 \quad 0.01 \quad -0.01]^T m$, and $d_{pc2} = [1.4 \quad 0.01 \quad 0.01]^T m$ for GRACE B. The observation data of the sub-maneuvers and their mirrors are processed in separate and combined manners. In each simulation, the boresight error, based on the true phase center and determined phase center, is calculated. The boresight errors for the two cases are shown in Table 5.4.

Table 5.4   Boresight Errors for KBR Calibration (linearly drifting)

Boresight Errors (mrad)					
Test Case	Four Sub-maneuvers		Four Mirror Sub-maneuvers		Eight Combined Sub-maneuvers**	
Over	GRACE A	GRACE B	GRACE A	GRACE B	GRACE A	GRACE B
Equator	2.30	0.76	2.10	0.91	0.21	0.21
Pole	2.64	1.30	2.92	1.54	0.15	0.16

**: results with the same POD error model for each case

In this table, the boresight error of each satellite in each case is presented. It can be seen that the boresight error is about 3 mrad from the calibration with sub-maneuvers or their mirrors. However, if the POD error models for the mirror sub-maneuvers ($\theta_1 < 0$) are the same as these for sub-maneuvers ($\theta_1 > 0$), the combined results can be better than 0.3 mrad. This condition may be not realistic, but it does indicate that the POD errors are largely removed by the approach used for the analysis. In fact, it has been found that the combined calibration results from the sub-maneuvers and mirror sub-maneuvers with different POD error models can not be improved. This fact is a strong indication that the POD error is a large contribution to the overall error. In addition, the calibration maneuvers over the equator and over pole yield the same level of accuracy, which demonstrates that the calibration accuracy is independent of the calibration location, unlike center of mass calibration.

5.3.2 Main Error Sources

From the observation data used in the estimation system, it can be seen that there are four major error sources corrupting the estimation results for KBR

169

calibration with the linear drifting maneuver. These are the KBR range rate noise (denoted by KBR), the POD error fusing the GPS observations (denoted by POD), the star camera attitude noise (denoted by SCA) and the magnetometer noise (denoted by MAG).

If we consider the calibration over the equator as an example, the effect on the boresight error due to these error sources is simulated. In each simulation run, one error source is deactivated. Suppose the boresight error with all noises is b_{all}, and the boresight error, when one error source is deactivated, is b_{est}. Figure 5.16 shows the magnitude of $|b_{all} - b_{est}|$ for every error source. This figure clearly demonstrates that the POD from the GPS observations is the largest error source, which is consistent with the simulation analysis.
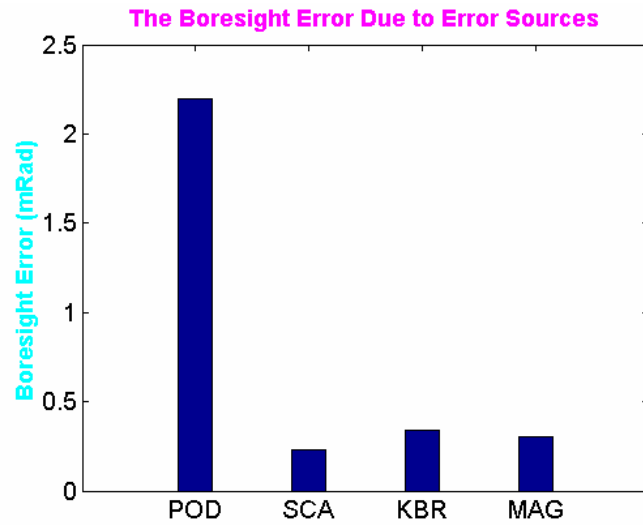

Figure 5.16 Boresight Error Due to Error Sources

5.4 KBR CALIBRATION WITH PERIODIC OSCILLATION MANEUVER

The principle of the K-band ranging system calibration with the periodic oscillation maneuver is the same as the calibration with the linear drifting maneuver. However, the realization and data processing of these two calibrations are quite different. From a realization point of view, the major difference between those two maneuvers is how the angular variations are induced. The periodic oscillation maneuver is conducted by oscillating about a bias angle while the linearly drifting maneuver is conducted by linearly rotating without an oscillation. In the data processing for the oscillating maneuver, the attitude dynamic equations of motion are not modeled and the processing is simple and direct.

As shown in Section 5.3.2, the main error source of the KBR calibration with the linearly drifting maneuver is position and velocity determination errors of the GRACE satellites. However, the periodicity of the angular variations in KBR calibration with the periodic oscillation maneuver may help to partially remove the flat relative orbit determination errors and therefore improve the calibration accuracy. However, another problem is encountered with the periodic angular variation. Since the multipath error is dependent on the magnitude of the angular variation, it exists as periodic signal in the K-band ranging system observations. Therefore, the K-band ranging system observations have two periodic signals, one is due to angular variation, the other is due to mutipath error. This is a significant disadvantage because these two signals can not be separated. There may be two potential solutions to this problem, one is to obtain a good

171

model for the antenna multipath effect, and the other is to possibly eliminate the multipath effects by mirror maneuvers.

In the simulations to evaluate these two approaches, the initial orbits and attitudes of the GRACE satellites are the same as in the center of mass calibration. At each dynamic integration step, the nominal line-of-sight between the GRACE satellites can be determined from the real attitude and orbit information. On the other hand, the expected satellite attitude can be obtained from the calibration maneuver design. Based on the expected attitude, the star camera observations can be generated. It should be pointed out that the star camera observations are based on the expected periodic oscillation attitude, not on the real attitude at each dynamic integration step. This is purely for simulation simplicity, because, otherwise, a quite complicated attitude control mechanism is required for the simulation. Meanwhile, the other observation data, such as the KBR range observations, and the POD, can be simulated. After preprocessing the star camera observation data and the POD data, the algorithm proposed in Section 4.4 can be used to estimate the K-band horn phase centers.

As a summary, the simulation procedure flow chart for center of mass calibration, KBR calibration with linearly drifting maneuver and KBR calibration with periodic oscillation maneuver is illustrated in Figure 5.17. The measurement corresponding to a particular calibration type has the same color. For example, the KBR periodic calibration uses the KBR range, POD and SCA data.
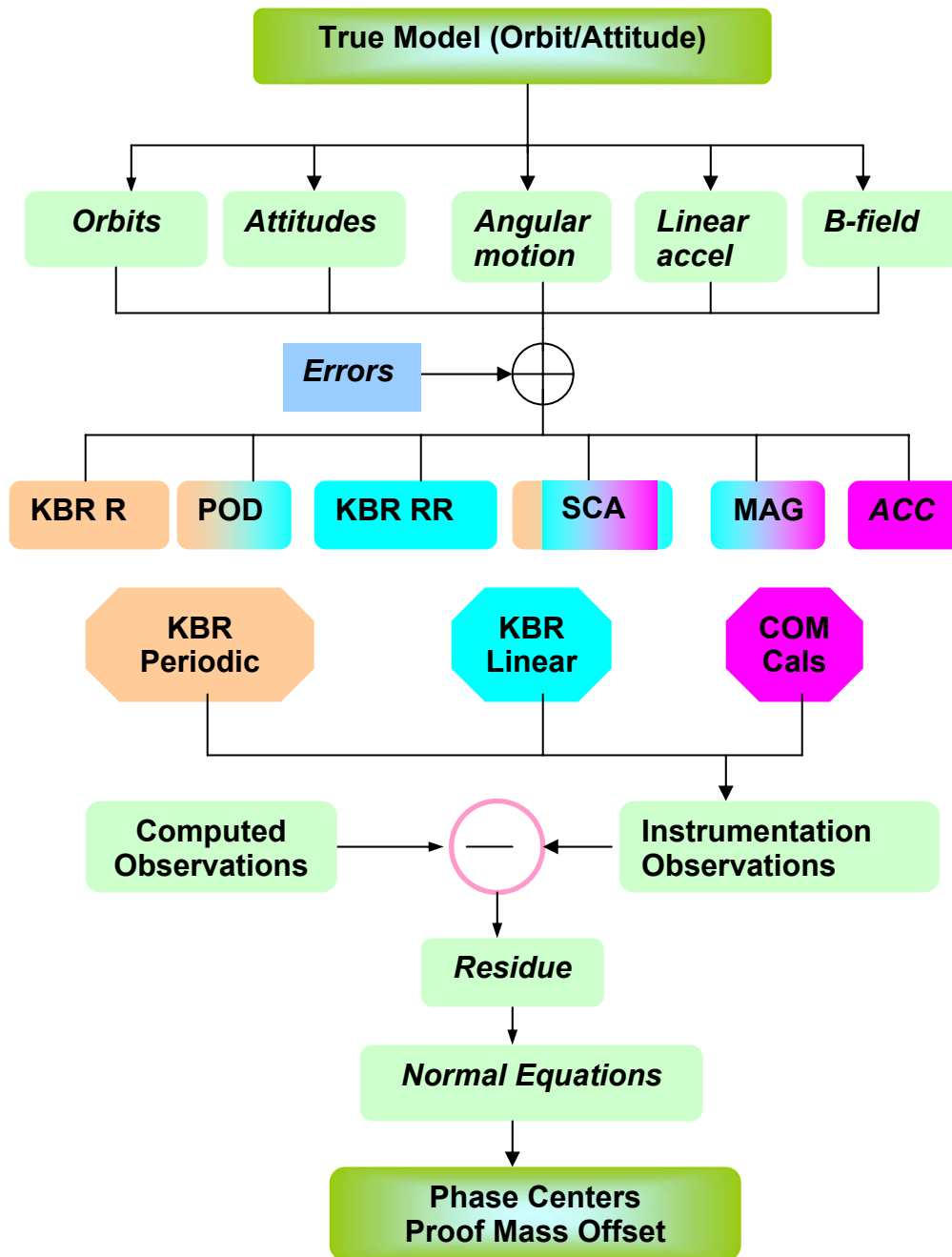
172

Figure 5.17   Flowchart of COM and KBR Simulation Procedure

5.4.1 Simulation Results and Analyses

The sub-maneuvers and their mirror sub-maneuvers for the periodic oscillation calibration are simulated in this section. Due to the maneuver realization constraint, the calibration duration is very long, typically 1,000 seconds. This time span is roughly a quarter of the satellite orbital period. In this duration, the ground tracks of the GRACE satellites will cover geographical locations near the equator and near the pole. In addition, since an active torque is not used in the data processing, there is no reason that location variations will result in different calibration accuracy. Therefore, only one orbit starting from the equator and ending near the north pole is simulated. However, there are some variations of maneuver parameters, including the angle deviation bias angle, $\theta_\circ$, angular variation amplitude, A, and the period, $2\pi / \omega$. The parameter variations and test cases are summarized in Table 5.5. The K-band horn phase center values for GRACE A and GRACE B are the same as for the KBR calibration with linearly drifting maneuvers. In each simulation, the boresight error, based on the true phase center and determined phase center, is calculated. The calibration accuracy for each test case can be measured by the boresight error.

Table 5.5 Calibration Test Parameter Variations

Test Case	Bias (Deg)	Amplitude (Deg)	Period (Sec)
Case I	2.0	1.00	250
Case II	2.5	0.50	200
Case III	3.0	0.17	100

Take the sub-maneuver A, in test case I, as an example. A sample of the observation data are plotted to illustrate some important points. Figure 5.18 shows the real KBR range data. It can be seen that the range changes about 650 meters during the whole calibration span. Of course, this value varies with the initial position at the beginning of the K-band ranging system calibration. The change is mainly due to the different orbit perturbations upon the two GRACE satellites. No obvious sine signal can be seen in the range observation. However, the derived range change, $|\vec{r}_1 - \vec{r}_2| - R$, contains a very strong sine signal due to the angular variation of GRACE A in the sub-maneuver, as illustrated by Figure 5.19. The phase centers can be extracted from the derived range change provided that the precise position determination of the satellites is available. Unfortunately, as pointed out before, the multipath error has exactly the same signal pattern as the derived range change variable, shown in Figure 5.20. These two signals cannot be separated. From Figure 5.20, it can be seen that the mutlipath error is about one tenth of the derived phase change. The multipath model in this study is a little pessimistic (or conservative) and the real multipath error could be smaller than the values used for this simulation.
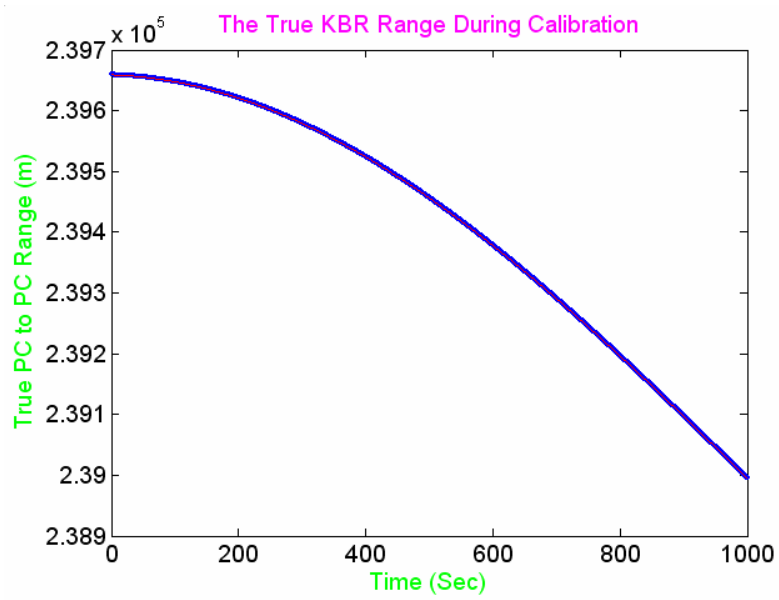
Figure 5.18   KBR Range Observation
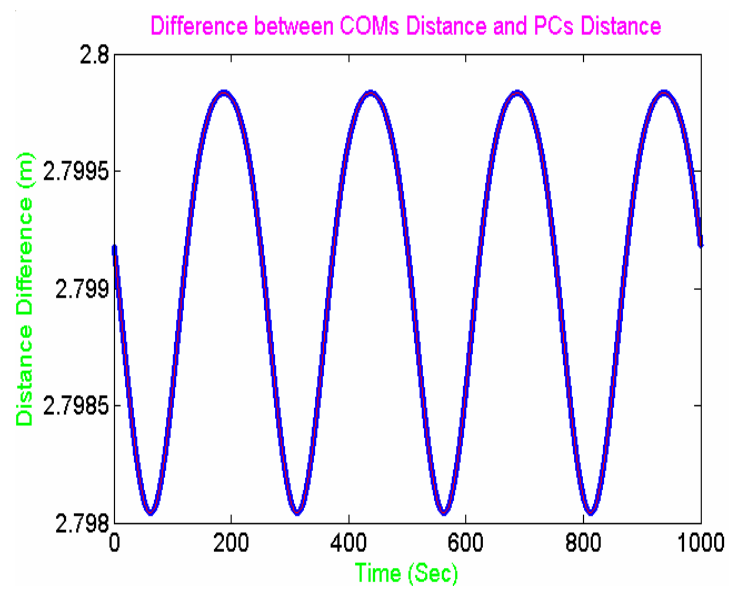
Figure 5.19   Derived Range Change dependent upon Angular Variation
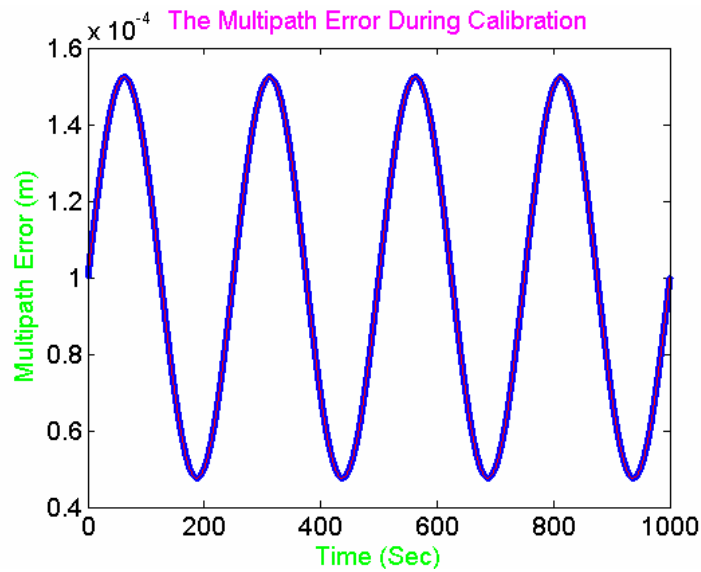
Figure 5.20   Mutipath Error

The boresight errors for these test cases are shown in Table 5.6. In this table, the boresight error of each satellite in each case is presented. Four sub-maneuvers and their mirror sub-maneuvers are processed in both separate and combined manners. From this table, it can be seen that both Test case I and Test II yield boresight errors which are around 3 mrad from sub-maneuvers or their mirrors. It is likely that the results of Test III are bad due to much smaller angular variations compared to test case I and test case II since large angular variations induce strong phase change signals.

Suppose that the antenna multipath error parameter μ is exactly the same for both the sub-maneuver and its mirror sub-maneuver, the multipath error can be cancelled by averaging the estimates from the sub-maneuvers and their mirrors based on the noise analysis in Section 4.4.1. From Table 5.6, it can be seen that the combined results can be greatly improved in test case I and test case II due to

177

the multipath error cancellation. This may be not realistic, especially the sub-maneuvers B and D, since the K-band horns are not symmetrical with respect to the nominal attitude when these sub-maneuvers and their mirrors are carried out. However, it is expected that the estimates can be improved by the total eight sub-maneuvers. We caution again that the multipath error used in simulations may be pessimistic.

Table 5.6   Boresight Error for KBR Calibration (periodic oscillation)

Boresight Errors (mrad)						
Test Case	Four Sub-maneuvers		Four Mirror Sub-maneuvers		Eight Combined Sub-maneuvers**	
	GRACE A	GRACE B	GRACE A	GRACE B	GRACE A	GRACE B
Case I	2.95	3.49	2.40	3.44	0.29	0.08
Case II	0.16	6.59	1.26	6.74	0.59	0.15
Case III	3070	3067	3066	3067	3012	3011

**: The results are based on the assumption that mutipath error can be eliminated by mirror maneuvers, which might not be valid.

This table shows that if the multipath error can be eliminated, the boresight error of the phase center determination can be better than 0.3 mrad. Otherwise, based on the noise analysis in Section 4.4.1, the multipath error causes the boresight error shifting 0.003(m/rad)/1.4(m), about 3 mrad, which is the boresight error for sub-maneuvers or mirrors.

5.4.2 KBR Calibration Parameters for Real Mission

If the multipath error can be removed for the K-band ranging system calibration with the periodic oscillation maneuver, the boresight of the phase

center estimation can be better than 0.3 mrad, which is much better than the results from the K-band ranging system calibration with the linearly drifting maneuver. The possibility of removing the mutipath error may evolve in two ways. One is to obtain a good mutipath model, and the other is the possible reduction by mirror maneuvers. Based on this conjecture, the K-band ranging system calibration with the periodic oscillation maneuver is chosen for the real mission by calibration design team. Based on the simulation results and analyses, the calibration parameters for the real mission are specified in Table 5.7.

Table 5.7   The KBR Calibration Parameter Design

Real KBR Calibration Parameters	
Category	*Parameters*
Location	- No preference
Angle Bias	- 2 Deg
Amplitude	- 1 Deg
Period	- 250 Seconds
Duration	- 1000 Seconds

In fact, this parameter set is the same as test case I in the simulations.

5.4.3 KBR Misalignment Correction Error Simulation

The estimated phase center can be different from the true phase center. Using the estimated phase center and attitudes and orbits of satellites, the KBR range observation can be corrected to compensate the misalignment of the COMs and phase centers. However, the range correction may have some errors, thus affecting the accuracy of the range rate and range acceleration values.

In this simulation, the attitudes and orbits of the GRACE satellites on August, 18, 2002 are used as an example. On this day, the attitude control deadband is about 4mrad. Based on the KBR correction error formulation, shown by Equation (4.155), it is expected that the range correction error can be $\sim 10\mu m$ if the phase center boresight error is 3 mrad, and $\sim 1\mu m$, if the phase center boresight error is 0.3 mrad. Using the CRN filter, the range rate and range acceleration can be derived from the KBR corrected (noise containing) range. Figure 5.21 shows the error of KBR corrected range, range rate (denoted by RR) and range acceleration (denoted by RA). It can be seen that the range error is at the same level as predicted by Equation (4.155). The range rate can be far less $1\mu m/s$ for both large boresight error and small boresight error. This figure ensures that the KBR calibration results can be used in KBR range correction and that the resultant KBR range and range rate satisfy with the mission requirement.
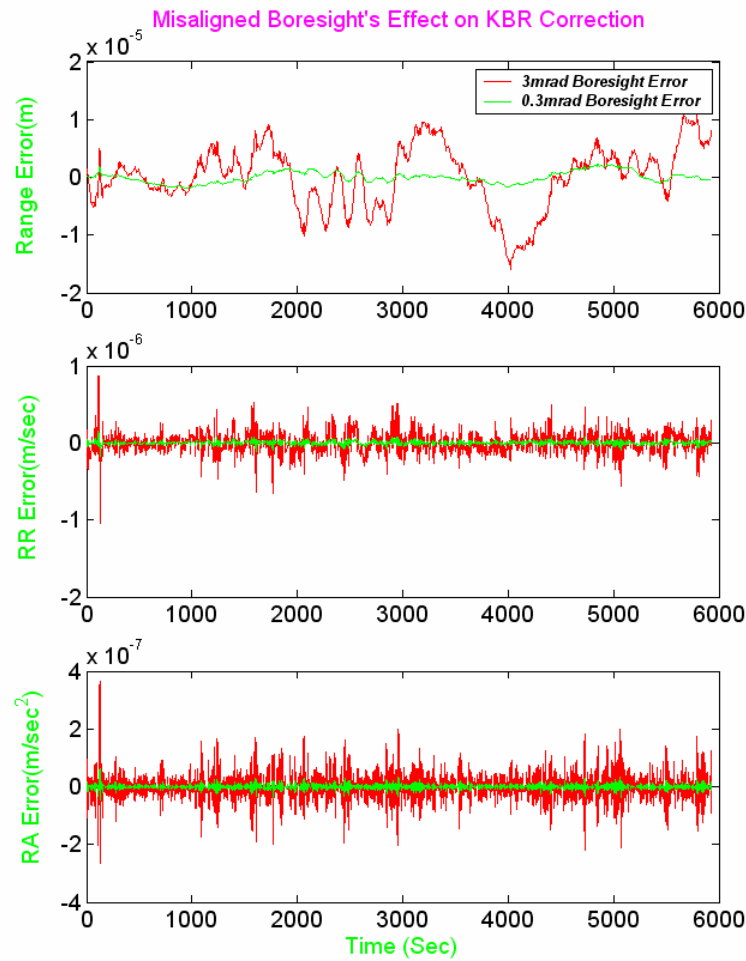
Figure 5.21   Range/RR/RA Errors from Phase Center Corrected KBR Range

5.4.4 AOCS Simulation and Analysis

Using the maneuver parameters listed in Table 5.7, a simulation was conducted using the AOCS control side at Dynamics and Control Systems Analysis, Space Systems/ Loral (Cully, 2002). This simulation confirms that the

181

K-band ranging system calibration with the periodic oscillation maneuver can be realized with the designed parameters.

Figure 5.22 shows sub-maneuver and its mirror sub-maneuver in KBR calibration maneuver design. It can be seen that the attitude control mechanism is really capable of driving the satellite in the designed calibration manner.
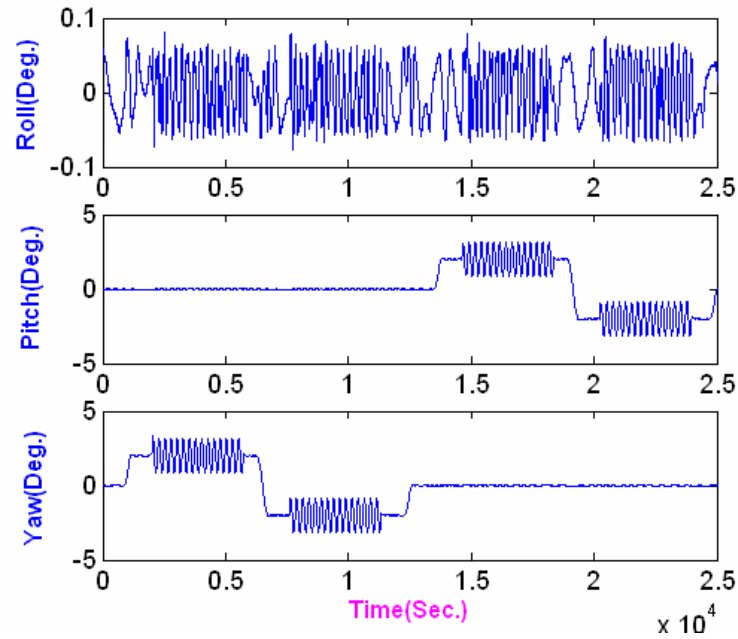
Figure 5.22   Sub-maneuver and its Mirror Sub-maneuver

5.4.5 Main Error Sources

There are three error sources which influence the estimation accuracy for this KBR calibration. They are the KBR range errors (denoted by KBR* and MUL), POD errors from GPS observations (denoted by POD) and the star camera attitude errors (denoted by SCA).

Take test case I as an example, the boresight error due to these three error sources is carried out in the same way as the error source simulation described in Section 5.3.2. The results, shown below in Figure 5.23, clearly demonstrate that multipath error is the largest error source.
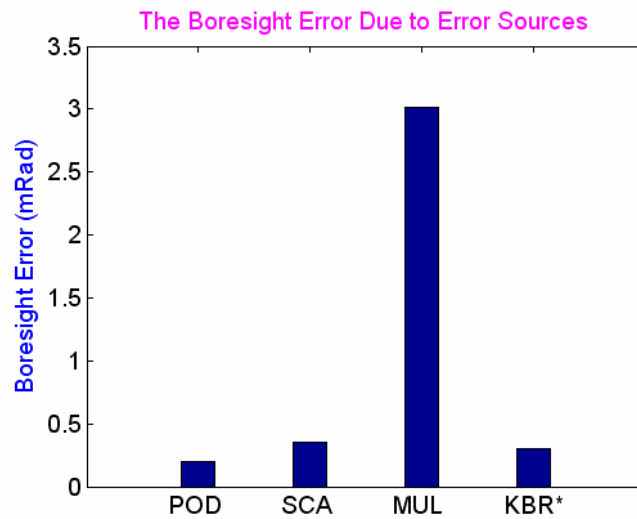
Figure 5.23   The Error Sources Effect upon Boresight

Note: KBR* includes everything, but the multipath error.

It is within expectation that the KBR range error is the largest error source, particularly the multipath error. The POD errors from the GPS observations are largely removed by a polynomial function due to its flatness relative to the sine signal, and star camera's observations are quite accurate and ready for use directly. Therefore, these two error sources contribute much less to the boresight error than the KBR range error.

5.5 START CAMERA MISALIGNMENT ESTIMATION

As developed in Section 4.7, the star cameras misalignment can be determined from the observations of both star cameras. Although the misalignment of each star camera with respect to the satellite body-fixed frame can not be determined by this approach, the misalignment of one star camera with respect to the other one can be determined.

Given a series of observations from both star cameras, q_{obs}^1 and q_{obs}^2. At each observation point, the derived rotation matrix B can be obtained from Equation (4.167). By averaging this rotation matrix, denoted by $\overline{B}$, the star cameras misalignment parameters $(\theta_1, \theta_2, \theta_3)$ and $(\beta_1, \beta_2, \beta_3)$ can be obtained as $\beta_2 - \theta_3 = \overline{B}_{12}$, $\theta_2 - \beta_3 = \overline{B}_{13}$, $\theta_1 - \beta_1 = \overline{B}_{22}$, given by Equations (4.169) through (4.171). The misalignment parameters of each star camera are a set of small rotation Euler angles mapping its nominal star camera frame and true frame.

The simulation uses both star cameras' observations, generated based on the procedure described in Section 3.6.2. The true values of the misalignment parameters $(\theta_1, \theta_2, \theta_3)$ are assigned the quantities (-0.2, 0.2, -0.15) mrad, and $(\beta_1, \beta_2, \beta_3)$ are considered to be (-0.1, 0.1, 0.23) mrad. The true values and estimated values of the combination of misalignment parameters are shown in Table 5.8.

Table 5.8   Simulation Results for Star Cameras Misalignment

Relative Combination	$\theta_2 - \beta_3 = \overline{B}_{12}$	$\beta_2 + \theta_3 = \overline{B}_{13}$	$\beta_1 - \theta_1 = \overline{B}_{22}$
True Values (mrad)	-0.03	-0.05	0.1
Estimated Values (mrad)	-0.0237	-0.0367	0.1274

From this table, it can be seen the small angle misalignment parameters can be determined better than 0.05 mrad.

Chapter 6: Real Data Processing

6.1 SUCCESSFUL LAUNCH OF GRACE

A Russian rocket booster, Eurockot, successfully launched the twin GRACE satellites on March 17, 2002. It lifted off from the snow-covered Plesetsk Cosmodrome in northern Russia at 4:21 am EST (0921 GMT) and placed the two satellites into 500-km polar orbits. The two satellites, nicknamed "Tom" and "Jerry" after two classic cartoon characters, fly about 200 kilometers apart. The flight trajectory is illustrated in Figure 6.1.
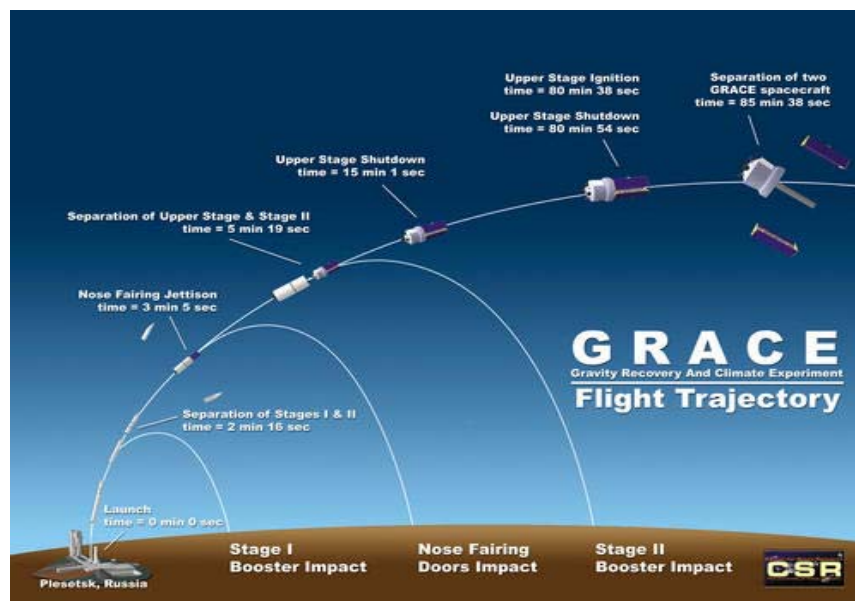
Figure 6.1   Russian-built rocket lift off with GRACE on March 17, 2002

186

6.2 CENTER OF MASS CALIBRATION

6.2.1 Main Events History

On Day 17 and Day 18 after the GRACE launch, the wiggle tests were executed for GRACE B and then GRACE A, respectively. These tests are to determine whether the designed maneuver can be realized. The wiggle tests were perfectly executed, which is a good indication of future successful center of mass calibration maneuver.

On Day 29, the first calibration maneuvers for GRACE A and GRACE B were successfully executed. Unfortunately, a saw-tooth profile for the angular accelerations occurred. This anomaly could possibly reduce the proof mass offset calibration accuracy. However, the effects on the estimation results are highly dependent upon the data processing algorithms. The estimation algorithms proposed in this study are relative insensitive to attitude corrections of this type. Still, better angular acceleration profiles are desired. After careful review of the data anomaly, the AOCS team determined that the anomaly is caused by the interaction between the magnetometer and magnetorquer system. As pointed out in previous sections, the magnetometer measures the Earth's magnetic field, and the magnetorquer system is used to control the attitude of satellite via a magnetic torque. The real center of mass calibration adopts a commanded torque according to the procedure discussed in Section 3.4. Recalled that the applied magnetic moment (as in Equation (3.11)) is based on the magnetic field B_c, which can be obtained from the magnetic field model or by direct measurement with the magnetometer. The calibrations on this day and Day 17 and Day 18 use

magnetometer data to determine the Earth's magnetic field B_c. Due to the interaction between magnetometer and magnetorquer system, a saw-tooth control anomaly occurred in many of the cases. A typical anomaly is shown in Figure 6.2. In order to avoid such an anomaly, a pure magnetic field dipole model (Wertz, 1978, Stevens, 2003) is used to represent the Earth's magnetic field.

Figure 6.2   Angular Acceleration Anomaly in COM Calibration
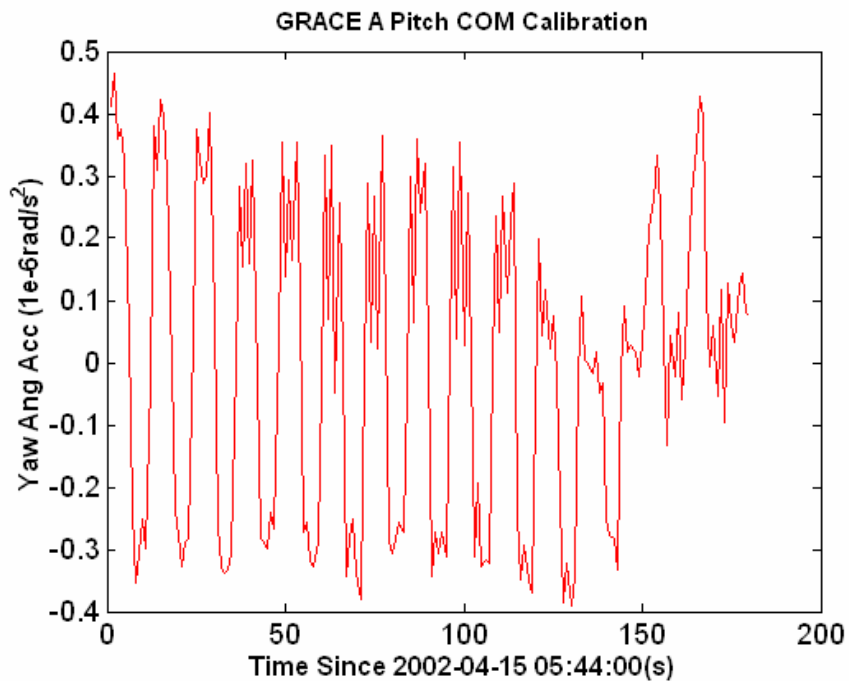
Then on Day 39 and Day 43, calibration maneuvers were executed for GRACE B and GRACE A, respectively. The anomaly was removed, as expected.

These calibration data were analyzed independently by the JPL and the UTCSR. Initially, the estimated proof mass offset of each GRACE satellite is about 0.3 mm in magnitude. The results from each center are consistent. On Day

188

50, the proof mass offset trim was performed to cancel the proof mass offset. Then on next day, Day 51, follow-up calibrations were conducted for both GRACE A and GRACE B. The post-trimmed calibration analysis shows that the proof mass offset of GRACE B is well within 0.1 mm along each axis, and proof mass offset of GRACE A along pitch and yaw axes are within 0.1 mm, proof mass offset along roll axis is a little bit larger than 0.1 mm.

In a second calibration nine months later on February 4, 2003, it was determined that the GRACE B satellite had a set of COM calibration maneuvers. The proof mass offset values were quite close to these from the first calibration. This is exciting because it shows that the proof mass offset is fairly stable. On February 27, 2003, the calibrations were also applied to GRACE A. Within expectation, the offsets were also close to the last calibrated values, which had a relatively large offset along the roll axis. On March 7, 2003, the center of mass trim was performed for GRACE A and follow-up calibrations were executed on the same day. Analysis shows that the trim was quite successful, and now, the center of mass offsets of both GRACE satellites are far within tolerance of 0.1 mm.

The roll maneuver of GRACE B on April 3, 2002 at 08:03:30 is used as an example. The linear and angular acceleration of the accelerometer measurements and their amplitude, with respect to the signal periods, are shown in Figure 6.3. The linear acceleration sub-figure clearly shows that some huge spikes along the yaw axis occurred. The maneuver type, which can be seen from the angular acceleration sub-figure, is the roll maneuver with the large component along the

roll axis. In addition, strong signals of linear acceleration along the pitch axis and angular acceleration along the roll axis, at magnetic torque input period of 12 seconds, indicate that the proof mass offset along the yaw axis is large on this day. A rough calculation of 5e-9/2e-5, gives 0.25 mm, which is close to the estimation value of 0.2 mm.
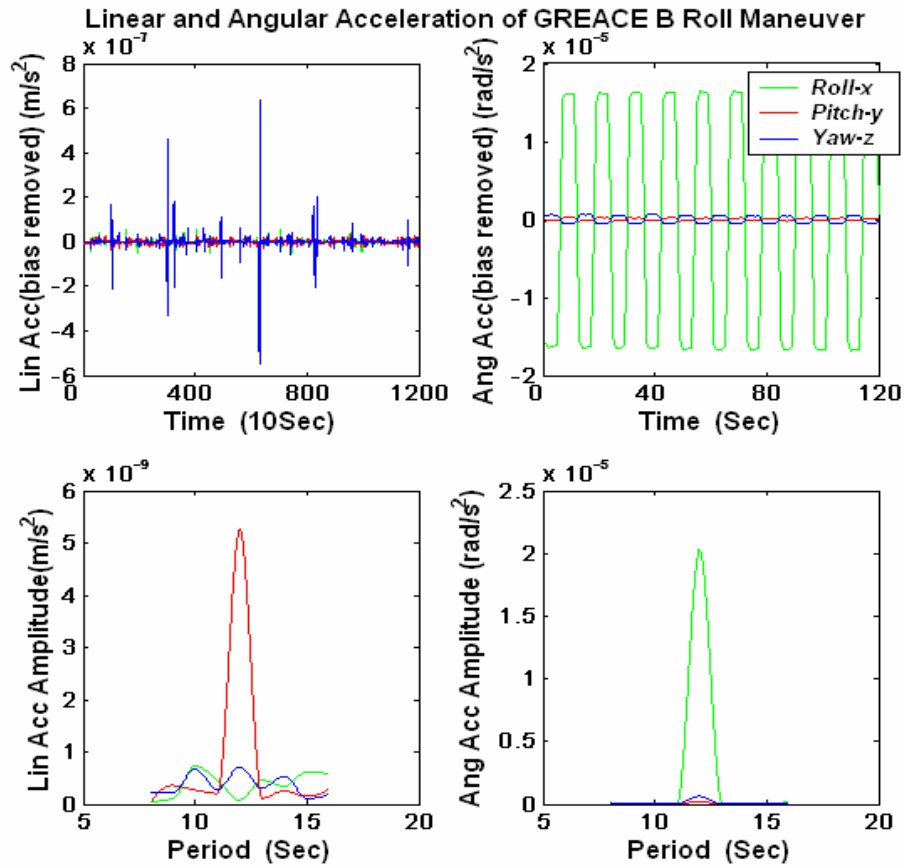
Figure 6.3   Linear and Angular Acceleration of GRACE B Roll Maneuver

In this study, the angular acceleration used in the analysis is predicted by algorithms in Section 4.2 from the star camera quaternion data and the maneuver

type. Figure 6.4 shows that the predicted angular acceleration along each axis is quite close to the observed angular acceleration, especially along the largest component axis, which is the roll axis in this case.
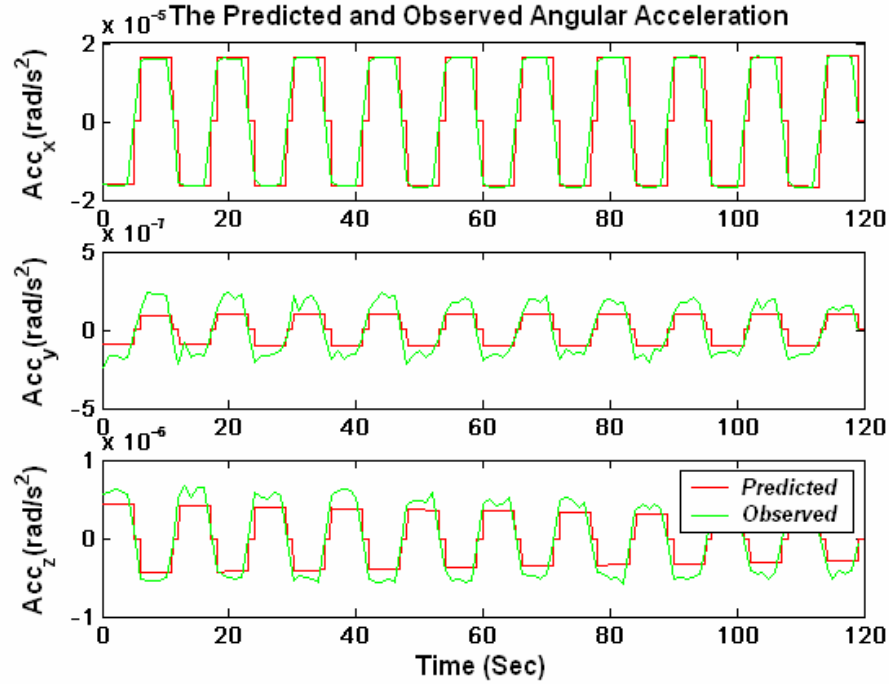
Figure 6.4   Comparison of Predicted and Observed Angular Acceleration

If the proof mass offset is large, it is expected that a periodic signal in the linear acceleration at the same frequency as the angular acceleration will be seen. In the early mission time, this did occur. The following figure, Figure 6.5, clearly shows the nice match of the linear and angular acceleration. In the calibrations after the trim, such a match no longer exists. By removing the angular motion induced disturbance acceleration, it has been found that the post-fit linear acceleration residual gets much smaller.
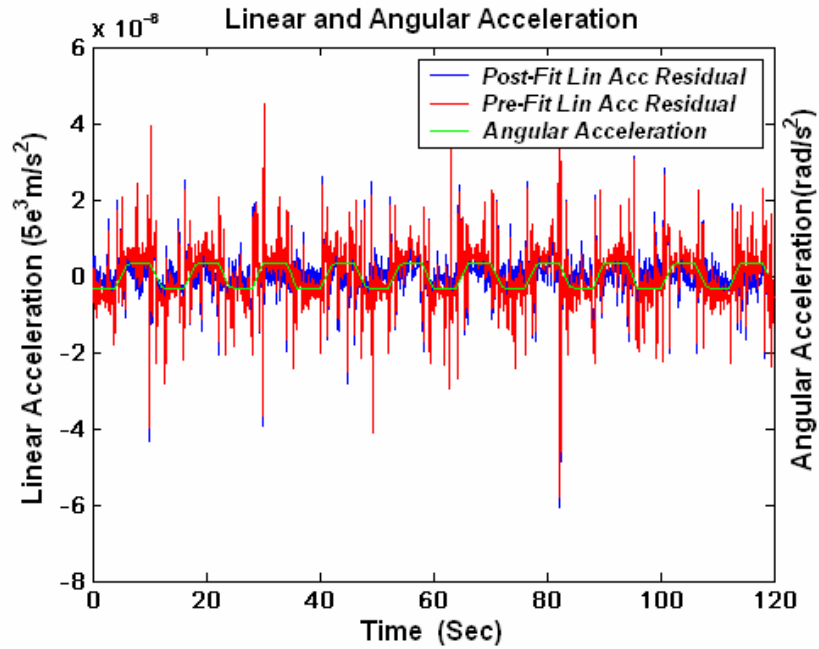
Figure 6.5 Match of the Linear Acceleration and Angular Acceleration

Overall, the center of mass calibrations are quite successful. It confirms that the maneuver design for center of mass calibration is viable, and the data processing algorithms are effective.

The sequence of events for the calibration maneuvers and mass trim are summarized in Table 6.1.

6.2.2 Data Analysis Approach

As listed in Table 6.1, three or four center of mass calibration maneuvers were carried out for every GRACE satellite on each calibration day. Since the proof mass offset is quite stable in a short time period, the calibration data for each satellite on that calibration day can be combined together to do the optimal

fitting. Processing of calibration maneuver data together allows the proof mass offset to be determined accurately along all three satellite body-fixed axes.

Table 6.1   GRACE Center of Mass Calibration Events

Day	GRACE A	GRACE B
Day17	---	Pitch_P Roll_P Yaw_P
Day18	Pitch_P Roll_P Yaw_P	---
Day29	Pitch_E Yaw_E Roll_P	Pitch_E Yaw_E Roll_P
Day39	---	Pitch_E Roll_P Yaw_E Pitch_P
Day43	Pitch_E Roll_P Yaw_E Pitch_P	---
Day50	Proof Mass Offset Trim	
Day51	Pitch_E Yaw_E Roll_P Pitch_P	Pitch_P Yaw_E Pitch_E Roll_P
02/04 2003	---	Yaw_E Pitch_P Roll_P Pitch_E
02/27 2003	Yaw_E Pitch_P Roll_P Pitch_E	---
03/07 2003	Proof Mass Offset Trim Yaw_E Pitch_P Roll_P Pitch_E	---

Note: _P means the center of mass calibration is done near the Earth's North Pole, and _E means the calibration is done near the Equator. The order of the event represents the calibration order on that day.

On each calibration day, the attitude data from star camera, linear acceleration and angular acceleration data from accelerometer, the Earth's magnetic field measurements from the magnetometer and the satellite orbit information are available. Due to the interaction between magnetometer and magnetorquer system, the magnetometer data was not used during the calibration period. Therefore, the magnetic field model (Equation (2.29)) is used to generate the Earth's magnetic field data based on the orbit and attitude information. The observation data from the star camera and accelerometer, and the Earth's

magnetic field data are complete for the data processing algorithms developed in Section 4.2.

Overall, the observation data are quite consistent with the simulation data. The major difference is that the linear acceleration data from the accelerometer have large spikes and twangs. These anomalies have to be removed before the data can be used in the data processing algorithms. Therefore, careful selection of calibration periods is desired. This step is beyond the model used in the simulation. A typical example of the data anomalies is shown in Figure 6.6.
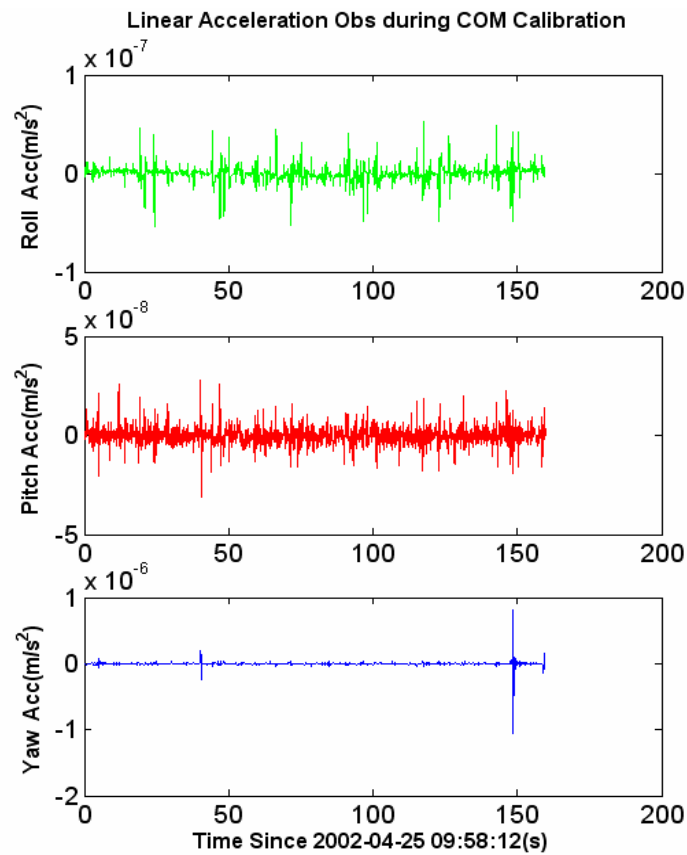
Figure 6.6   Accelerometer Observations during a COM Pitch Maneuver

194

Figure 6.6 is a typical representation of the linear acceleration observations. The spikes along the yaw axis are particularly large, while the accelerations along the other two axes are free from huge jumps. As a matter of fact, the spikes exist not only during the center of mass calibration, but also during the satellite nominal flight mode. The factors that cause the spikes are still under investigation and beyond the scope of this research.

In this research, the calibration data spans in which spikes happen are eliminated. Taken the above figure as an example, the calibration data during periods (0-40) seconds and (50-140) seconds are to be fitted into the estimation system. The data beyond these spans are ignored because large spikes occur.

After selecting the calibration data spans, each small piece of data, including Earth's magnetic field data, star camera observation data and linear acceleration observation data, are ready to be processed. Before putting this data into the algorithms described in Section 4.2, the linear acceleration data are smoothed by CRN filter, denoted as

$$A'_{out} = CRN(A_{out})$$
(6.1)

The CRN filter parameters are designed as: f_{si}=10 Hz, f_{so}=10Hz, B_w=1Hz, T_f=10.1, N_c=7, f_{sel}=0.083Hz.

Then bias and linear drift are removed from the linear acceleration data. To do so, the accelerometer's observation model in Equation (4.40) can be further simplified as follows

$$A'_{out} = \alpha t + \beta + A_n$$
(6.2)

195

Let the estimated parameter vector be $X = [\alpha, \beta]^T$, then the observation-state mapping matrix is given by

$$H(t_k) = [t_k I \quad I]_{3\times 6} \tag{6.3}$$

Thus given the accelerometer's acceleration observation data $y = \{A'_{out}(t_1), A'_{out}(t_2),...A'_{out}(t_m)\}$ and observation weight matrix R^{-1}, combined with the observation-state mapping matrix, the normal equation matrices, $\sum_i H_i^T R_i^{-1} H_i, \sum_i H_i^T R_i^{-1} y_i$, can be accumulated at given observation data epoch. After all the observation data have been accumulated, the estimate of linear drift parameter and bias can be obtained as

$$X = (\sum_{i=1}^{m} H_i^T R_i^{-1} H_i)^{-1} \sum_{i=1}^{m} H_i^T R_i^{-1} y_i \tag{6.4}$$

After that, the linear acceleration observation data at each epoch can be reconstructed as

$$y'_i = y_i - \alpha t_i - \beta \tag{6.5}$$

Then, the star camera observation data, the Earth's magnetic field data and the reconstructed linear acceleration observation data can be processed through the algorithm pipes proposed in the Section 4.2.1 and 4.2.5.1. The only difference is that, since the linear accelerations have already been linearly fitted, the estimated parameter and observation-state mapping matrix are redefined as $X = [d]$ and $H(t_k) = \widetilde{A}$, respectively. After going through this step, the

196

accumulation matrices $\sum_i H_i^T R_i^{-1} H_i, \sum_i H_i^T R_i^{-1} y_i$, which contain the proof mass

offset information, are recorded.

The estimate from each small piece of data may not have adequate information for an accurate estimate. However, after all of the short segments are combined, the final proof mass offset can be obtained as

$$X = (\sum_{j=1}^{p}(\sum_{i=1}^{m} H_i^T R_i^{-1} H))^{-1} \sum_{j=1}^{p}(\sum_{i=1}^{m} H_i^T R_i^{-1} y_i) \qquad (6.6)$$

where X is the proof mass offset vector, $X = [d]$, j is an index of a segment of data, p is the total number of pieces of all calibration data on that day, i is the index of number of observations in each piece, m is the total number of observations in each piece, H_i, R_i, y_i are the observation-state mapping matrix, observation weight matrix and observation residue.

Consider Figure 6.6 as an example, and assume that only one maneuver happens on that day, otherwise, similar figures for all other maneuvers have to be included here to illustrate, the index p is equal to 2, and m is equal to 400 and 900.

6.2.3 Proof Mass Offset Estimates

Using the data processing approach described in Section 6.2.2, the proof mass offset for each GRACE satellite can be determined. The results are listed in Table 6.2. Based on the analysis, the accuracy should lie between the optimistic accuracy, represented in analysis in (Wang, 2000b), and the worst case analysis, represented by the simulations in Section 5.2.3. It is believed that the estimation

confidence for offset along the roll axis is better than $(40\mu m, 3\sigma)$, and offset along pitch and yaw axes is better than $(30\mu m, 3\sigma)$.

Table 6.2   Proof Mass Offset Estimates

Day	GRACE A (mm)			GRACE B (mm)		
Day17	---			0.021	0.018	-0.202
Day18	0.256	-0.127	0.118	---		
Day29	0.268	-0.133	0.117	-0.011	0.012	-0.195
Day39	---			0.017	-0.004	-0.210
Day43	0.236	-0.138	0.121	---		
Day50	Proof Mass Offset Trim					
Day51	0.150	0.002	0.015	0.038	0.015	0.035
02/04/2003	---			-0.020	-0.013	-0.046
02/27/2003	0.170	-0.033	0.052	---		
03/07/2003	Proof Mass Offset Trim -0.047 0.005 -0.036			---		

From the above table, it can be seen that the proof mass offset estimates are consistent for the calibration periods before each proof mass offset trim. This is a good indication of the accurate proof mass offset determination since the proof mass offset is believed to be stable during that period.

Another observation is that the GRACE A's proof mass offset along the roll axis is poorly determined compared to the other five parameters during the period before March 7, 2003. The covariance analysis in Section 4.2.6 indicates given a larger angular acceleration along one axis than the other two, the better proof mass offset along the other two axes is determined with this larger angular acceleration. This is the effect observed here. Since the moment of inertia along the roll axis is much smaller than along the pitch and yaw axes, the corresponding angular acceleration along the roll axis is larger than along the other two axes.

Therefore, it is expected that the proof mass offset along the roll axis cannot be determined as well as along the other two axes. This effect is observed in Table 5.3. The results for GRACE B are optimistic since, prior to trim, the proof mass offset along the roll axis is very small. This situation does not occur for GRACE A.

From this table, it can be seen that, in the year 2002, the proof mass offset for GRACE B and the offset along the two axes of GRACE A are satisfied with the specified requirements of the error being less than 0.1 mm, and the offset along the roll axis of GRACE A being just a little bit larger than the requirement. This offset was corrected during the 2003 calendar year. During this period, the proof mass offsets for both GRACE A and GRACE B are far less the requirement of 0.1 mm.

6.3 K-BAND RANGING SYSTEM CALIBRATION

The real GRACE K-band ranging system calibration maneuvers have been successfully completed. The calibration maneuvers for GRACE B were executed during the period of February 10, 2003 and February 11, 2003, and on February 20, 2003. Calibration maneuvers for GRACE A were carried out on March 12, 2003, March 19, 2003, and March 21, 2003. Prior to the KBR calibration on each satellite, the center of mass calibrations were performed to make sure that the proof mass offset is within the requirement.

As designed, each satellite has four sub-maneuvers, positive pitch maneuver, negative pitch maneuver, positive yaw maneuver, negative yaw maneuver. The attitude deviation of the calibrated GRACE satellite from the

nominal flight attitude in each sub-maneuver roughly followed the designed maneuver, which is two degrees biased along pitch or yaw axis with a periodic oscillation of one degree amplitude. Each sub-maneuver is comprised of 15 wiggles, instead of the 4 wiggles used in the simulations, to collect a more robust data set.

In the data analysis discussed here, it has been found that the estimates of the phase centers are very stable with respect to the different data spans. Four wiggles in each sub-maneuver are enough to obtain good results. Therefore, in each sub-maneuver, four of the best-quality continuous wiggles are selected for data processing. The section criteria are based on the attitude derivation performance and data quality. The dual star cameras quaternion observations, precise satellite orbits, and K-band ranging system range data of GRACE satellites are used in the estimation system. The orbits and KBR range data are quite smooth, while the attitude observations have some jumps during a short period. Calibration periods without large attitude observation jumps and smooth KBR range data have been selected.

A typical example of the attitude derivation of GRACE B is shown in Figure 6.7. The red line in first sub-plot shows the difference between the KBR range data and the position differences of the twin satellites. This difference is called the derived range change in Section 5.4.1, and the similar simulated data plots are shown in Figure 5.19. The following three sub-plots show the attitude derivation with respect to the nominal flight attitude. As indicated, this figure shows a minus pitch sub-maneuver. The green line in first sub-plot is also the

attitude deviation, which is the same as the pitch angle motions. It can be clearly seen that the derived attitude change matches the attitude variation well. The GRACE A satellite has a similar performance.
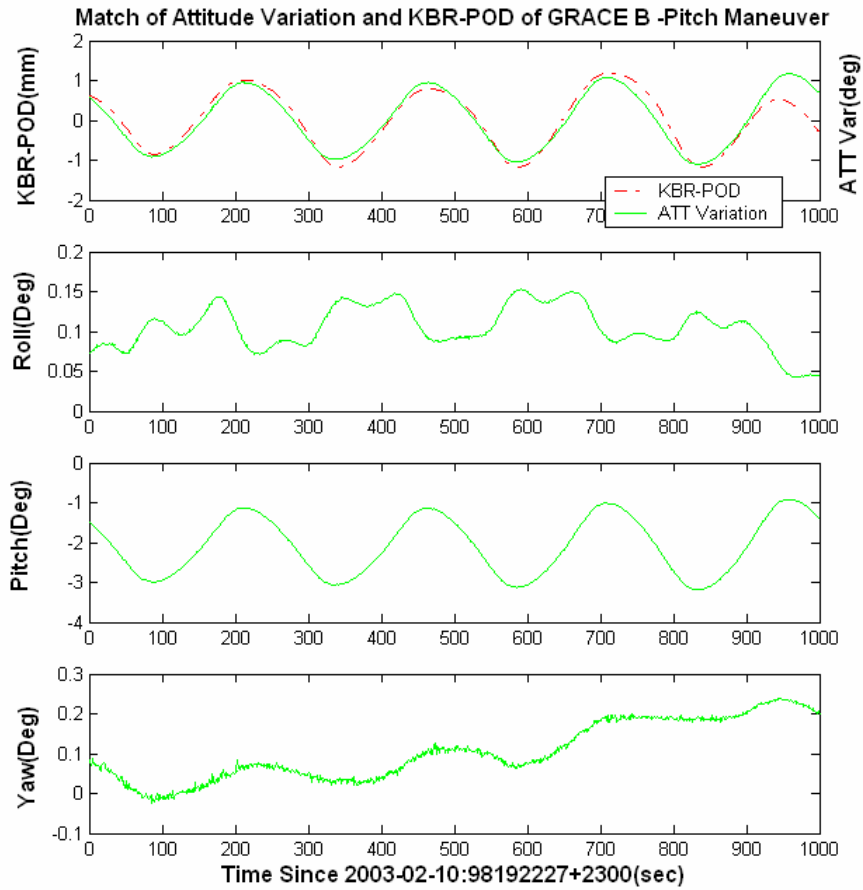
Figure 6.7   GRACE B Minus Pitch KBR Calibration Maneuver

In the analysis, since the x-component of the phase centers of both satellites, where the center of mass is the origin of the satellite body fixed frame, are believed to be well-calibrated to be 1.472584 meter, and also for good stable

solutions, the estimation algorithm used is slightly different from the algorithm presented in Section 4.4. The x-component is fixed at the permission value instead of estimated. Several best-quality precise orbits, generated from GPS observations only and using SCA attitude observations and ACC linear accelerations, are tested in the phase center determinations. It has been found that the solutions are quite stable.

In fact, the results obtained from this algorithm are dependent upon the nominal rotation matrix between SCA frame and SF. However, when representing the results in the SCA frame, they are independent of which frame the attitude quaternion data are described in. In other words, the results in the SCA frame, obtained from the estimations in the satellite frame and the SCA frame, are the same. In addition, there exists a misalignment between these two frames, as analyzed in Section 6.4. Using the misalignment parameters in Table 6.4, the phase centers can be updated. Ideally, the phase centers from both SCA observations should be same in the SF, after applying the misalignment corrections. It has been found that small difference between them exists. Finally, the phase center estimates from different star camera sensors are averaged to produce the KBR phase center value in SF, which will be used in the misalignment correction in the KBR data processing. A simple average is adequate since the results from both sensors have almost the same statistical errors. The KBR phase centers in SF are shown in Table 6.3. Based on the analysis, the estimation confidence of the boresight of the phase center is about $(0.3 mrad, 1\sigma)$.

Table 6.3   GRACE KBR Phase center in Satellite Frame

GRACE KBR Phase Center in Satellite Frame		
Sensor No	Phase Centers along X/Y/Z axis (meter)		
GA, From Sensor 1	1.472584	0.003081	-0.006250
GA, From Sensor 2	1.472584	0.003873	-0.007002
GA, Alignment Applied	1.472601	-0.000337	0.002529
GB, From Sensor 1	1.472584	0.002853	-0.006944
GB, From Sensor 2	1.472584	0.002587	-0.007360
GB, Alignment Applied	1.472599	-0.000047	0.003465

6.4 SCA-ACC ALIGNMENT CALIBRATION

During the KBR calibration, the magnitude of angular acceleration of the satellite can be as large as 10 $\mu rad/m^2$. The large angular motions can be precisely detected by both the star camera and the accelerometer. Therefore, it is the precious opportunity to determine the misalignment between SCA and ACC by comparing the angular acceleration observation data of the accelerometer and the derived angular acceleration data from the star camera's quaternion observations.

6.4.1 ACC Angular Acceleration Data Processing

The GRACE accelerometer precisely measures the angular acceleration of the spacecraft. It outputs the observation data roughly once every second. The time tag offset is believed to be -0.14 second.

The angular acceleration observation data in the KBR calibration timeslot can be expressed in the satellite frame, and linearly interpolated to be evenly distributed data with an appropriate time tag correction. The CRN filter is used to

remove high frequency noises with the filtering parameters designed as, $f_{si}=1$ Hz, $f_{so}=1$Hz, $B_w=0.01$Hz, $T_f=140.7$, $N_c=7$, $f_{sel}=0.004$Hz.

With this effort, the angular acceleration data in the satellite frame from the accelerometer are ready for further processing.

6.4.2 SCA Derived Angular Acceleration Data Processing

In the KBR calibration periods, the dual star cameras work simultaneously to record the attitude motion in each individual SCA frame. Based on Section 4.7, the observation data from the two sensors can be used to determine the relative misalignment between the two SCA frames. With the same notations, the relative misalignment parameters can be obtained by applying the real data.

In deriving the relative misalignment in Section 4.7, it is assumed that the boresight of the star camera frame is mounted exactly $45°$ relative to the radial upward direction of the satellite frame. However, the nominal rotation matrix between these frames, determined by pre-launch measurements and post-launch instrument validations, is slightly different from this ideal situation. This can be accommodated by introducing some small values in Equation (4.165) as follows

$$R_{BS}^1 (R_{BS}^2)^{-1} = \begin{bmatrix} 1 & \eta_2 & -\eta_1 \\ \eta_1 & \eta_3 & 1 \\ \eta_2 & -1 & \eta_3 \end{bmatrix} \tag{6.7}$$

The values (η_1, η_2, η_3) for each GRACE satellite can be calculated once the nominal rotation matrices are known. With the same definition of $\overline{B}$ matrix as in Equation (4.168), the relative misalignment parameters are given by

$$\theta_2 - \beta_3 = \overline{B}_{12} - \eta_2 \tag{6.8}$$

$$\beta_2 + \theta_3 = \overline{B}_{13} + \eta_1 \tag{6.9}$$

$$\beta_1 - \theta_1 = \overline{B}_{22} - \eta_3 \tag{6.10}$$

Inserting real data into the above equation, the results for GRACE A are

$$\theta_2 - \beta_3 = -0.000778 \tag{6.11}$$

$$\theta_3 + \beta_2 = 0.000057 \tag{6.12}$$

$$\beta_1 - \theta_1 = -0.002320 \tag{6.13}$$

The results for GRACE B are

$$\theta_2 - \beta_3 = -0.000169 \tag{6.14}$$

$$\theta_3 + \beta_2 = 0.000363 \tag{6.15}$$

$$\beta_1 - \theta_1 = -0.00159 \tag{6.16}$$

The dual GRACE star cameras output the observation data once every second. The time tag offset is estimated to be 0.234 second. Adding the time corrections, the quaternion observation data, in each star sensor's frame, can be linearly interpolated to obtain evenly distributed data without data gaps.

Based on the relative misalignment information and the star camera's nominal noise characteristics, the dual star cameras quaternion observation data can be optimally combined in each star camera's frame to reduce the observation noise.

Suppose at any observation time t, the quaternion data from sensor one of either GRACE satellite is $q^{s1}(q_1^{s1}, q_2^{s1}, q_3^{s1}, q_4^{s1})$, and from sensor two is

$q^{s2}(q_1^{s2}, q_2^{s2}, q_3^{s2}, q_4^{s2})$. Then, considering the misalignment transformation, the observation of sensor two in sensor one's frame can be obtained as

$$\Re(q^{s1-s2}) = R_{mis}^1 R_{BS}^1 (R_{BS}^2)^{-1} (R_{mis}^2)^{-1} \Re(q^{s2}) \tag{6.17}$$

Using the $\overline{B}$ matrix in Equation (4.168), the above equation can be expressed as

$$\Re(q^{s1-s2}) = \overline{B}\Re(q^{s2}) \tag{6.18}$$

Likewise, the observation of sensor one in sensor two's frame can be expressed by

$$\Re(q^{s2-s1}) = \overline{B}^{-1}\Re(q^{s1}) \tag{6.19}$$

With a simple derivation, it can be shown that the derived quaternion q^{s1-s2} and q^{s2-s1} have the following relationship with q^{s1} and q^{s2}

$$\Re(q^{s1-s2}) = \overline{B}R_n^2\overline{B}^{-1}(R_n^1)^{-1}\Re(q^{s1}) \tag{6.20}$$

$$\Re(q^{s2-s1}) = \overline{B}^{-1}R_n^1\overline{B}(R_n^2)^{-1}\Re(q^{s2}) \tag{6.21}$$

In the actual application, the quaternion data are noisy, and satisfy with the following equation

$$\Re(q^{s1}) = \Xi(\varepsilon_1, \varepsilon_2, \varepsilon_3)\Re(q^1) \tag{6.22}$$

$$\Re(q^{s1-s2}) = \Xi(\alpha_1, \alpha_3, -\alpha_2)\Re(q^1) \tag{6.23}$$

$$\Re(q^{s2}) = \Xi(\alpha_1, \alpha_2, \alpha_3)\Re(q^2) \tag{6.24}$$

$$\Re(q^{s2-s1}) = \Xi(\varepsilon_1, -\varepsilon_3, \varepsilon_2)\Re(q^2) \tag{6.25}$$

where

$$\Re(q^1) = R^1_{mis} R^1_{BS} \Re(q) \qquad (6.26)$$

$$\Re(q^2) = R^2_{mis} R^2_{BS} \Re(q) \qquad (6.27)$$

At any epoch, the difference can be obtained from the quaternion data, q^{s1_s2}, q^{s2_s1}, q^{s1} and q^{s2}, as

$$\Delta^{s1} = \Re(q^{s1\_s2}) \Re(q^{s1})^{-1} \qquad (6.28)$$

$$\Delta^{s2} = \Re(q^{s2\_s1}) \Re(q^{s2})^{-1} \qquad (6.29)$$

The small rotation angles $\delta^{si}(\delta_1, \delta_2, \delta_3)$ can be obtained from Δ^{si} as follows

$$\Xi(\delta^{si}) = \Delta^{si} \qquad (i = 1,2) \qquad (6.30)$$

The GRACE star cameras, sensor one and sensor two, are assumed to have the nominal noise characteristics

$$\Lambda^{s1} = \Lambda^{s2} = \begin{bmatrix} 1 & 0 & 0 \\ 0 & 1 & 0 \\ 0 & 0 & k^2 \end{bmatrix} \sigma^2 \qquad (6.31)$$

where z is the camera boresight direction, the formal error in the perpendicular directions is about $\sigma \approx 6\,\text{arcsec}$, and the formal standard deviation for the rotations about the boresight is a factor of $k \approx 8$ greater (Romans, 2003).

The information matrix rotated into sensor one's frame from sensor two is given by

$$\Lambda^{s1\_s2} = \overline{B}\Lambda^{s2}\overline{B}^{-1} \tag{6.32}$$

And the information matrix rotated into the sensor two's frame from sensor one is given by

$$\Lambda^{s2\_s1} = \overline{B}^{-1}\Lambda^{s1}\overline{B} \tag{6.33}$$

Then optimal small rotation angles δ^{s1opt} can be obtained as

$$\delta^{s1opt} = -(\Lambda^{s1} + \Lambda^{s1\_s2})^{-1}\Lambda^{s1\_s2}\Delta^{s1} \tag{6.34}$$

$$\delta^{s2opt} = -(\Lambda^{s2} + \Lambda^{s2\_s1})^{-1}\Lambda^{s2\_s1}\Delta^{s2} \tag{6.35}$$

Finally, the optimally combined quaternion data in the star camera frame are given by

$$\Re(q^{s1opt}) = \Xi(\delta^{s1opt})^{-1}\Re(q^{s1}) \tag{6.36}$$

$$\Re(q^{s2opt}) = \Xi(\delta^{s2opt})^{-1}\Re(q^{s2}) \tag{6.37}$$

Using the algorithm in Kinematic Model Filtering of Section 4.2.5.1, the angular acceleration can be obtained from the above the optimally combined quaternion data series. However, the disadvantage of this algorithm is that the quaternion data must pass through the CRN filter twice. It has been demonstrated that this algorithm can be improved by using the CRN filter second directives computation as follows

$$\begin{aligned}
\dot{\omega}_x &= 2(q_4 \cdot \ddot{q}_1 + q_3 \cdot \ddot{q}_2 - q_2\ddot{q}_3 - q_1\ddot{q}_4) \\
\dot{\omega}_y &= 2(q_4 \cdot \ddot{q}_2 - q_3 \cdot \ddot{q}_1 - q_2\ddot{q}_4 + q_1\ddot{q}_3) \\
\dot{\omega}_z &= 2(q_4 \cdot \ddot{q}_3 - q_3 \cdot \ddot{q}_4 + q_2\ddot{q}_1 - q_1\ddot{q}_2)
\end{aligned} \tag{6.38}$$

where

$$\ddot{q} = CRN''(q^{opt})$$ 　　　　　　　　(6.39)

The second derivative CRN filter uses the following parameters in the real data processing: f_{si}=1 Hz, f_{so}=1Hz, B_w=0.01Hz, T_f=140.7, N_c=7, f_{sel}=0.004Hz. Basically, the parameters are the same as used in smoothing angular acceleration observation data from ACC.

6.4.3 Estimation Algorithm

Once the angular acceleration data from ACC and SCA data are available, these data can used in the estimation system to determine the misalignment parameters.

There are four calibration sub-maneuvers for each GRACE satellite, and the dual star cameras observation data are available in each sub-maneuver. In this study, the observation data from the positive pitch and positive yaw maneuvers are processed separately from the observation data of the corresponding minus maneuvers. One advantage of separately processing positive maneuvers and minus maneuvers is to check the consistency of the results. Since the alignments are constant, a set of stable solutions should be consistent when processing different maneuvers. In addition, the relative misalignment parameters of dual star cameras, as described by Equations (6.11) through (6.16), are quite stable. This set of equations can be used as a constraint when processing the dual star cameras data. Therefore, only the misalignment parameters of sensor one are determined.

In general, the estimation system can be written as follows

$$\dot{\omega}_{SCA} = \Xi(x)R_{BS}c(\dot{\omega}_{ACC} - b) \qquad (6.40)$$

where, $\dot{\omega}_{SCA}$ is the derived angular acceleration in star camera's frame, $\dot{\omega}_{ACC}$ is the angular acceleration observations from ACC, R_{BS} is the rotation matrix from satellite frame to star camera frame, which is dependent upon the sensor number. The parameters, b and c, are the bias and scale of the angular acceleration observation, and x is the misalignment parameters of sensor one. This model can be applied to either sub-maneuver and either star camera sensor for any GRACE satellite.

In the data analysis conducted here, it has been found that the bias can be fixed to the mean value of the observations during the calibration period, and the scale can be fixed to 0.96. It has been demonstrated that using the fixed values of b,c, instead of solving for them along with x, yields the same value of the estimate for x. For this reason, in the data processing described here, the bias and scale use the fixed values. Therefore, the above equation can be simplified to obtain

$$\dot{\omega}_{SCA} = \Xi(x)\bar{\dot{\omega}}_{ACC} \qquad (6.41)$$

or

$$\dot{\omega}_{SCA} - \bar{\dot{\omega}}_{ACC} = -\Pi(x)\bar{\dot{\omega}}_{ACC} \qquad (6.42)$$

where

$$\ddot{\omega}_{ACC} = R_{BS}c(\dot{\omega}_{ACC} - b) \qquad (6.43)$$

In this representation, the angular accelerations are all in the star camera frame.

For the pitch maneuver with observation data from star camera sensor one, the fit residual and the mapping matrix are given by

$$y_1 = \begin{bmatrix} \dot{\omega}_{SCA}(t_1) - \ddot{\omega}_{ACC}(t_1) \\ \dot{\omega}_{SCA}(t_2) - \ddot{\omega}_{ACC}(t_2) \\ \vdots \\ \dot{\omega}_{SCA}(t_{m_1}) - \ddot{\omega}_{ACC}(t_{m_1}) \end{bmatrix} \qquad (6.44)$$

$$H_1 = \begin{bmatrix} \Pi(\ddot{\omega}_{ACC}(t_1)) \\ \Pi(\ddot{\omega}_{ACC}(t_2)) \\ \vdots \\ \Pi(\ddot{\omega}_{ACC}(t_{m_1})) \end{bmatrix} \qquad (6.45)$$

where m_1 is the total number of the observations.

Likewise, one can get the fit residual and the mapping matrix, y_2 and H_2 for yaw maneuver with observation data from star camera sensor one.

For the pitch maneuver and the observation data from star camera sensor two, the fit residual and the mapping matrix are given by

$$y_3 = \begin{bmatrix} \dot{\omega}_{SCA}(t_1) - A \cdot \ddot{\omega}_{ACC}(t_1) \\ \dot{\omega}_{SCA}(t_2) - A \cdot \ddot{\omega}_{ACC}(t_2) \\ \vdots \\ \dot{\omega}_{SCA}(t_{m1}) - A \cdot \ddot{\omega}_{ACC}(t_{m1}) \end{bmatrix} \qquad (6.46)$$

$$H_3 = \begin{bmatrix} \Pi'(\dot{\bar{\omega}}_{ACC}(t_1)) \\ \Pi'(\dot{\bar{\omega}}_{ACC}(t_2)) \\ \vdots \\ \Pi'(\dot{\bar{\omega}}_{ACC}(t_{m_1})) \end{bmatrix} \tag{6.47}$$

where A is given by

$$A = \Xi(a_3, a_2, -a_1) \tag{6.48}$$

and

$$\theta_2 - \beta_3 = a_1 \tag{6.49}$$
$$\theta_3 + \beta_2 = a_2 \tag{6.50}$$
$$\beta_1 - \theta_1 = a_3 \tag{6.51}$$

The operator $\Pi'()$ on any vector $v(v_x, v_y, v_z)$ is given by

$$\Pi'(v) = \begin{bmatrix} 0 & v_y & v_z \\ v_z & -v_x & 0 \\ -v_y & 0 & -v_x \end{bmatrix} \tag{6.52}$$

Likewise, one can get the fit residual and the mapping matrix, y_4 and H_4 for the yaw maneuver with observation data from star camera sensor two.

Finally, the estimate of the misalignment parameters of star camera sensor one is given by

$$\hat{x} = (H^T \cdot H)^{-1} H^T y \tag{6.53}$$

where $H = \begin{bmatrix} H_1 & H_2 & H_3 & H_4 \end{bmatrix}^T$, and $y = \begin{bmatrix} y_1 & y_2 & y_3 & y_4 \end{bmatrix}^T$.

6.4.4 GRACE Calibration Data Processing

Following the previous sections on the SCA-ACC alignment calibration, the data from the GRACE calibration maneuvers have been processed.

Unfortunately, in all KBR calibration maneuvers, there exists a two and half seconds phase difference between angular acceleration observations from ACC and derived data from both SCA sensors observations. The real reason for that is still under investigation. In this study, the angular acceleration data from ACC is shifted two and half seconds forward to compensate this anomaly. Since the phase difference exists in the data, it has to be removed before any analysis is processed. Otherwise, one cannot obtain a stable solution.

The phase shifting technique really works no matter what causes the phase difference. In fact, even if the reason is found in the future, the alignment values based on this analysis should be still valid. More important, using this approach, the results are consistent with each other when different sub-maneuvers and different data span are used.

With two and half seconds shifting, the misalignment parameters of both star camera sensors, $(\theta_1, \theta_2, \theta_3)$ and $(\beta_1, \beta_2, \beta_3)$, on both GRACE satellites, have been recovered as shown in Table 6.4.

Table 6.4   GRACE SCA-SF Misalignment Parameters

GRACE Star Camera – Satellite Frame Misalignment Parameters		
Sensor No	Parameters (in Degs)	
Grace A, Sensor 1	-0.2110 0.3356 -0.1427	
Grace A, Sensor 2	-0.3439 0.1460 0.3802	
Grace B, Sensor 1	-0.1850 0.3668 -0.2075	
Grace B, Sensor 2	-0.2761 0.2283 0.3765	

Simulations show that with the noise characteristics of the GRACE star camera, $((80\mu rad, 1\sigma)$ in perpendicular directions to the boresight and $(240\mu rad, 1\sigma)$ about the boresight) the formal error of the derived angular accelerations is less than $0.1\mu rad/s^2$ along each axis. In addition, the angular acceleration response to the periodic angular motions has been the same frequency f_0, with the nominal value of 0.004, during the K-band ranging system calibration. Measuring at an interval of T, 1000 seconds used in the data analysis, allows one to select a band about f_0 of width $\Delta f = 1/T$. The random noise in the accelerometer angular acceleration measurement is, heuristically

$$\sigma^2 \approx \int_{f_0-(\Delta f)^2}^{f_0+(\Delta f)^2} PSD(f)df \approx \frac{1}{T}PSD(f_0) \tag{6.54}$$

The nominal performances for the accelerometer angular accelerations are $PSD(f) < 4 \cdot (1+\frac{0.005Hz}{f}) \times 10^{-14} rad^2 s^{-4} Hz^{-1}$ for the satellite frame pitch axis, and $PSD(f) < 3(1+\frac{0.1Hz}{f}) \times 10^{-11} rad^2 s^{-4} Hz^{-1}$ for the roll and yaw axes (Touboul, 2000). Substituting the above PSD values in Equation (6.54) results in

the formal error of the accelerometer's angular acceleration being less than $0.8 \mu rad / s^2$ for each axis.

The covariance of the estimate along each axis is about 1000 in the standard variable unit. No high correction between estimates has been found. Converting this covariance value to the estimation confidence of the misalignment parameter by multiplying $0.8 \mu rad / s^2$, gives $(0.04°, 1\sigma)$. In fact, this number is quite consistent with the estimate variation using different time span data and different sub-maneuver data. Overall, it is expected that the estimation confidence for each component of misalignment parameters is better than $(0.04°, 1\sigma)$.

Chapter 7: Conclusions

7.1 SUMMARY AND CONCLUSIONS

The objective of this research has been to investigate the center of mass calibration and K-band ranging system calibration for the GRACE satellites. Both calibrations are critically important for the GRACE mission, since they calibrate three of most important instruments on board GRACE twin satellites, i.e., the accelerometer, the K-band ranging systems, and the star camera.

The accelerometer is intended to measure all non-gravitational accelerations acting on the spacecraft. The accelerometer has a proof mass inside its cage, which is used as the sensing element. It is required that this proof mass should be positioned within a tolerance of 0.1 mm along each axis at the center of mass of the satellite. The objective of the center of mass calibration is to determine the proof mass offset during the nominal phase, and then, to use the center of Mass Trim assembly Mechanism to eliminate (or reduce) this offset. By carrying out this maneuver, the accelerometer's observation data can be used to represent the non-gravitational accelerations in the gravity recovery.

Besides the accelerometer, another important instrument on board GRACE satellite is the dual one way K-band ranging system, which is designed for precise inter-satellite phase measurements. The purpose of the K-band ranging system is to determine the phase center of the antenna on board each GRACE satellite, which ultimately allows the AOCS to adjust the attitude orientations of both satellites, and allows KBR post-processing to make the alignment

corrections. Hence, the K-band ranging system measures the biased range between the COMs of the twin satellites. This range observable can be used for the Earth's gravity recovery.

The star camera is vital to GRACE. It provides the information to allow the satellites to be pointed at each other, to allow accelerometer measurements to be transformed into the inertial frame of reference, and it allows the range observable between the phase centers of two K-band horns to be aligned along the COMs of the twin satellites. As a byproduct of the analysis of the K-band ranging system calibration, the misalignments between the star camera frame and the satellite frame can be also determined. This information can be used to produce better non-gravitational accelerations in the inertial frame and better KBR range data from the improved phase center positions.

The calibration maneuvers and the parameters for these calibrations have been carefully designed for the real mission. Complicated estimation algorithms to process the data have been developed. Complete simulations of these calibrations have been performed. Finally, the resulting approach has been used to process the mission data collected during the GREACE calibration maneuvers..

During the center of mass calibration, a periodic magnetic torque is applied to the satellite to create periodic angular motion related acceleration, superimposed upon the relatively flat non-gravitational accelerations. On each calibration day, multiple calibration maneuvers are executed. From the angular motion related accelerations of each maneuver (or all maneuvers), the proof mass offset was determined.

Important conclusions for the center of mass calibration are:

1.   A single center of mass calibration maneuver can determine the proof mass offset better than the system requirement as long as the maneuver satisfies the optimal location criterion.

2.   In the real calibration, multiple maneuvers are processed together. Based on the covariance analysis, it is expected that roll axis determination is the least accurate. Analysis of simulation data and real calibration data shows that offset along the roll axis can be determined better than $(40\mu m, 3\sigma)$, along the other axes offset can be determined better than $(30\mu m, 3\sigma)$.

3.   As of this writing, the center of mass offsets determined for GRACE A is [-0.047, 0.005, -0.036] mm, and for GRACE B is [-0.020 -0.013 -0.046] mm. Clearly, the center of mass offsets for both satellites are within the tolerance of 0.1 mm. Therefore goal of the center of mass calibration has been achieved.

There have been two different K-band ranging system calibration maneuvers investigated, e.g., the periodic oscillation maneuver and the linearly drifting maneuver. Both maneuvers are used to rotate the antenna along certain axis to find a reference point that produces minimum variation in the observed phase response. The periodic oscillation maneuver oscillates the satellite about a biased angle. In this case, the relative orbit determination error can be largely removed, since it is quite smooth compared to the periodic angular variation. However, the multipath error for the antenna will be the dominating error source. Alternatively, the linearly drifting maneuver is used to linearly rotate the satellite.

However, the relative orbit determination error could have a significant impact on the calibration accuracy. The accuracy can be improved when range rate is used in the estimation system, instead of range. Since the periodic oscillation maneuver may possibly dramatically improve the calibration accuracy by reducing the multipath errors through the mirror maneuvers and provide periodic angular variations to calibrate the misalignment of star camera frame and satellite frame, it is adopted in the real mission.

The K-band ranging system calibration data is used to determine the phase centers of the K-band horns and the misalignments between star camera frame and satellite frame. The important conclusions for the K-band ranging system calibration are summarized as follows:

4.   Since the phase centers of two GRACE antennas are highly correlated in the estimation process, four separate sub-maneuvers must be carried out. Their mirror sub-maneuvers are to back up maneuver observations and improve the phase center determination accuracy.

5.   Based on the analysis, the K-band ranging system calibration determines the K-band horn's phase center with an estimation confidence of boresight of $(0.3mrad, 1\sigma)$. This has been achieved by an acceptable filtering of the multipath error effects, which affects much less than in the simulation model. With this estimation accuracy, the KBR range and range rate alignment correction to compensate for the misalignment of COM's of the satellites and the phase centers can be better than $1\mu m$ and $1\mu m/s$, respectively.

6. Processing the angular acceleration observation data of the accelerometer and the derived angular acceleration data from the star camera's quaternion observations, the misalignment between the star camera frame and the satellite frame of each satellite was determined with an estimation confidence, for each alignment parameter, of $(0.04°, 1\sigma)$. This information has already been used to generate better acceleration and KBR range rate data. The goal of the K-band ranging system has also been achieved.

In summary and overall, executing the center of mass calibration and the K-band ranging system calibration and processing the calibration data have been proven to be quite successful.

7.2 RECOMMENDATIONS FOR FUTURE WORK

Although this research has involved the complete investigation of the center of mass calibration and K-band ranging system calibration for the GRACE mission, there are topics which remain open to further investigation for improvement of the GRACE calibrations.

Due to the realization constraint by the ground control station, the geophysical location of the COM calibration is not exactly the optimal location. A better short-time scale estimate of the satellite moment of inertia is certainly helpful in the data algorithms presented. In addition, the observed accelerometer acceleration data have the unexpected data anomaly. Efforts will be made in a future study to pursue the possible changes of the above limitations to improve the COM calibration estimates.

The antenna multipath errors seem to be much smaller than expected when analyzing the KBR calibration data. Nevertheless, a good realistic model should benefit the calibration accuracy. This may be achieved by analyzing the KBR range data and star camera attitude data. Better determination of the misalignment of the star camera frame and the satellite frame, as well as the time offset between the on board instruments, would allow for large improvements to the mission. Careful inspection of the KBR calibration data may allow for the derivation of more precise quantities. In addition, due to the relatively poor quality observation data for calibrating the frame alignment, the solution accuracy is less than expected and could be improved. This continuing work would certainly be helpful in accomplishing the GRACE mission targets.

Appendix A   CRN Filter

CRN filter is one of the finite-impulse-response low-pass digital filters, designed for extracting range, range rate and acceleration from the dual 1-way range values, by Thomas at JPL in May 1999 (Thomas, 1999). It can also be applied to other data filtering cases for reducing data rate and applying appropriate differentiation. Without loss of generality, range data filtering is taken as an example in the following appendix section.

The three time-domain filters, denoted by $F_n, \dot{F}_n, \ddot{F}_n$, operate in the time domain on the measured range values R_i' with an input sample rate of f_{si} (in Hz) to generate the observables of range, range rate, and range acceleration, respectively, at the nominal output rate of f_{so} (in Hz). In general, it is required that f_{si} is greater than or at least equal to f_{so}. Therefore

$$R_i = \sum_{n=-N_h}^{N_h} F_n R_{i-n}' \tag{A.1}$$

$$\dot{R}_i = \sum_{n=-N_h}^{N_h} \dot{F}_n R_{i-n}' \tag{A.2}$$

$$\ddot{R}_i = \sum_{n=-N_h}^{N_h} \ddot{F}_n R_{i-n}' \tag{A.3}$$

where $N_h = (N_f - 1)/2$. N_f is the total number of points spanned by the filter and is given by $N_f = f_{si} T_f$, where T_f is the selected filter input time window. For computational convenience, N_f will be set equal to an odd number. The index i denotes the ith output value computed as a weighted sum of the N_f input points symmetrically surrounding the ith output point in time. For each new

output point, the index i increments by the number of input time points equivalent to the desired output interval.

The digital filters must differentiate to the desired order and have a nearly rectangular response in the frequency domain with an appropriate low-pass cutoff. As is well known, a digital filter with a perfect rectangular response can be theoretically generated by convolving a signal with a sinx/x function in the time domain, provided the range of the sinx/x function is extended to infinity. Practical constraints, however, require the sinx/x function to be limited to a time window of tractable length.

In designing a CRN digital filter, one has to choose values for bandwidth, the number of convolutions N_c, and filter length T_f. To avoid aliasing out-of-band noise into the signal band, the bandwidth is set approximately equal to the Nyquist value, which is half of the output sample rate. Large values of N_c offer the advantage of making sidelobe magnitudes smaller in the window-function transform. However, as N_c increases for a fixed filter length, the width of the mainlobe of the window-function transform increases, which broadens the skirt of the low-pass cut-off of the digital filter so that it can reach back into the signal band and distort gain when the mainlobe becomes too wide. As filter length increases for fixed N_c, gain distortion at a given signal-band frequency tends to decrease as a result of the narrowing of the mainlobe of the window transform and the more rapid ripple drop-off caused by closer ripple spacing. Thus, increasing filter length is advantageous with respect to gain distortion, but has limits due to practical considerations such as computation time and exacerbation of data gaps.

223

In the design below, filter length is adjusted to a relatively low value consistent with signal-band-gain-distortion goals. Because of the sign flips of sidelobes found in odd-N_c CRN filters, a step up from even to odd N_c provides a much greater reduction in ripple than a step up from odd to even. For this reason, only odd N_c filters are considered.

To generate amplitude values for the selected CRN filter in the time domain, first create the required frequency response in the frequency domain and then transform with a Discrete Fourier Transform (DFT) to the time domain. Let the DFT of the digital filter have N_f frequency points with a spacing of $1/T_f$ and a frequency span of approximately $-f_{si}/2$ to $+f_{si}/2$. If B_w is the target single-sided bandwidth of the desired low-pass filter, let $N_B = B_w T_f$ be the number of frequency points spanned by B_w and for convenience let $2N_B + 1$ be an odd number. Note that the integer form of N_B means that B_w is approximated in quantized steps with a step size of $1/T_f$. Let N_R be equal to the number of points spanned by the basis rectangle of length T_R, where $T_R = N_R / f_{si}$. For computational simplicity, select N_R and N_f so that $N_f = N_c \cdot N_R$, where N_c is the number of convolutions of the basis rectangle.

The desired frequency-domain response is constructed as a convolution of a rectangular low-pass filter with the DFT of the selected time-domain window function. The rectangular low-pass filter has a quantized single-sided bandwidth equal to N_B / T_f and an amplitude equal to 1.0. Thus, with the quantization conventions specified above, the un-normalized frequency response can be computed according to

$$H_k = \sum_{k'=-N_B}^{N_B} \left(\frac{\sin[\pi(k-k')/N_c]}{\sin[\pi(k-k')/N_f]} \right)^{N_c} \qquad (A.4)$$

where the convolution sum over k' is carried out over points within the desired bandpass $(\pm N_B / T_f \approx \pm B_w)$, and H_k is the resulting frequency response at frequency point k/T_f, $|k| \le N_h$. The $(\sin x / \sin y)^N$ function in Equation (A.4) is the DFT of the selected CRN time-domain window function that is formed a N_c-fold self-convolution of a rectangular function of width $N_R = N_f / N_c$.

Once the frequency response has been computed according to Equation (A.4), the un-normalized time-domain filter for the range observable can be generated with a DFT

$$F_n' = \sum_{k=-N_h}^{N_h} H_k \cos(2\pi k n / N_f), \quad |n| \le N_h \qquad (A.5)$$

An overall gain normalization must be applied to the filter. This gain normalization is determined by applying (as in Equation (A.1)) the time-domain filter to a range input, R'_{i-n}, formed by a cosine function with $i = 0$ and with unit amplitude

$$R_n^t = \cos[2\pi f_{sel} n / f_{si}], \quad |n| \le N_h \qquad (A.6)$$

in which the frequency f_{sel} is set approximately equal to 0.37mHz. Gain normalization is adjusted so that the amplitude of this particular cosine function is still 1.0 after being passed through the filter. The scale to normalized the F_n' is given as

225

$$Sca = \sum_{n=-N_h}^{N_h} R_n^t \cdot F_n' \tag{A.7}$$

Thus

$$F_n = F_n' / Sca \tag{A.8}$$

The un-normalized range-rate and acceleration filters for use in Equations (A.2) and (A.3) are generated with the following DFTs

$$\dot{F}_n' = \sum_{k=-N_h}^{N_h} -(2\pi k / N_f) H_k \sin(2\pi k n / N_f), \quad |n| \le N_h \tag{A.9}$$

for the range-rate filter and

$$\ddot{F}_n' = \sum_{k=-N_h}^{N_h} -(2\pi k / N_f)^2 H_k \cos(2\pi k n / N_f), \quad |n| \le N_h \tag{A.10}$$

for the acceleration filter.

To normalize $\dot{F}_n'$ and $\ddot{F}_n'$, the scale is given by

$$Sca' = \sum_{n=-N_h}^{N_h} \sin(2\pi f_{sel} n / f_{si}) \cdot \dot{F}_n' \tag{A.11}$$

$$Sca'' = \sum_{n=-N_h}^{N_h} \cos(2\pi f_{sel} n / f_{si}) \cdot \ddot{F}_n' \tag{A.12}$$

Finally

$$\dot{F}_n = -\dot{F}_n' / (Sca' \cdot 2\pi f_{sel}) \tag{A.13}$$

and

226

$$\ddot{F}_n = \ddot{F}'_n / (Sca'' \cdot (2\pi f_{sel})^2) \qquad\qquad (A.14)$$

Given the design parameters f_{si}, f_{so}, B_w, T_f, N_c and f_{sel}, the digital filtering of any time-series observations can be performed.

Appendix B   Quaternion Operation

The two star cameras on board each GRACE satellite output the quaternion observations, which describe the attitude rotation relationship between inertial space and the star camera fixed frame. The four components of the quaternion are dependent, and defined in Equation (2.18) based on the Euler axis $a(a_x, a_y, a_z)^T$ and Euler angle ϕ

$$q(t) = \begin{bmatrix} q_1 & q_2 & q_3 & q_4 \end{bmatrix}^T = \begin{bmatrix} \varepsilon \\ \eta \end{bmatrix} = \begin{bmatrix} a \sin(\phi/2) \\ \cos(\phi/2) \end{bmatrix} \qquad (B.1)$$

which is subject to

$$|q(t)| = \varepsilon^T \cdot \varepsilon + \eta^2 = q_1^2 + q_2^2 + q_3^2 + q_4^2 = 1 \qquad (B.2)$$

The rotation matrix corresponding to the quaternion is given by

$$C = (\eta^2 - \varepsilon^T \cdot \varepsilon)I + 2\varepsilon \cdot \varepsilon^T - 2\eta \cdot \Pi(\varepsilon) \qquad (B.3)$$

where I is a three by three unit matrix and $\Pi(\varepsilon)$ is defined by Equation (4.39).

The rotation matrix in Equation (B.3) is nothing but the rotation operator $\Re()$ defined in Equation (2.19). Given the rotation matrix, the four components of quaternion can be obtained reversely as solved in Equations (4.2) through (4.4) from the rotation matrix $ROTIB$.

Quaternion $q(\varepsilon, \eta)^T$ can also be parameterized in terms of the Euler angles. Note it is different from the Euler angle ϕ used in Equation (B.1). There always exists a set of Euler angles $\theta(\theta_1, \theta_2, \theta_3)$ such that

$$\Re(q) = C(\theta) = C_1(\theta_1) \cdot C_2(\theta_2) \cdot C_3(\theta_3) \qquad \text{(B.4)}$$

where

$$C_1(\theta_1) = \begin{bmatrix} 1 & 0 & 0 \\ 0 & \cos\theta_1 & \sin\theta_1 \\ 0 & -\sin\theta_1 & \cos\theta_1 \end{bmatrix} \qquad \text{(B.5)}$$

$$C_2(\theta_2) = \begin{bmatrix} \cos\theta_2 & 0 & -\sin\theta_2 \\ 0 & 1 & 0 \\ \sin\theta_2 & 0 & \cos\theta_2 \end{bmatrix} \qquad \text{(B.6)}$$

$$C_3(\theta_3) = \begin{bmatrix} \cos\theta_3 & \sin\theta_3 & 0 \\ -\sin\theta_3 & \cos\theta_3 & 0 \\ 0 & 0 & 1 \end{bmatrix} \qquad \text{(B.7)}$$

which is often referred to as 3-2-1 Euler angles rotation.

There are some beautiful properties of the quaternion representation used in this research.

First, in the case of a small rotation, for example, small angles $\theta(\theta_1, \theta_2, \theta_3)$ for Euler angles representation, or small values ε and $\eta \approx 1$ for the quaternion representation, the rotation matrix can be simplified as

$$C(\theta) = I - \Pi(\theta) \qquad \text{(B.8)}$$

for the Euler angles representation. In fact, this is exactly what the anti-symmetric matrix operator $\Xi()$, defined in Equation (3.10), yields given the small Euler angles θ.

For the quaternion representation, it has the form

$$\Re(q) = I - 2\Pi(\varepsilon) \qquad \text{(B.9)}$$

In this case, the relationship between Euler angles and the quaternion is very simple. More specifically

$$\varepsilon = \frac{\theta}{2\sqrt{1+|\theta|^2/4}}, \eta = \frac{1}{\sqrt{1+|\theta|^2/4}} \tag{B.10}$$

Secondly, two sequential rotations, $q'(\varepsilon', \eta')$ and $q''(\varepsilon'', \eta'')$ can be elegantly combined to an equivalent single rotation $q(\varepsilon, \eta)$ as

$$\varepsilon = \eta'' \cdot \varepsilon' + \eta' \cdot \varepsilon'' + \Pi(\varepsilon') \cdot \varepsilon'' \tag{B.11}$$

$$\eta = \eta' \cdot \eta'' - \varepsilon'^T \cdot \varepsilon'' \tag{B.12}$$

The matrix representation of this property is, of course

$$\Re(q) = \Re(q'') \cdot \Re(q') \tag{B.13}$$

Furthermore, if the two sequential rotations are small angular rotations, the order of the rotations are no longer important, and the resultant rotation matrix can be reduced as

$$\Re(q) = I - 2\Pi(\varepsilon' + \varepsilon'') \tag{B.14}$$

For the sequential small Euler angles rotations θ', θ'', it has the form

$$C(\theta) = I - \Pi(\theta' + \theta'') \tag{B.15}$$

In fact, Equations (4.163) and (4.164) are exactly based upon this nice property.

In this case, the quaternion relationship can be derived, based upon the definition of the operator $\otimes$ defined in Equation (4.67), as

$$q = q'' \otimes q' = \frac{1}{\sqrt{1 + |\varepsilon' + \varepsilon''|^2}} \begin{bmatrix} \varepsilon' + \varepsilon'' \\ 1 \end{bmatrix} \qquad \text{(B.16)}$$

As a matter of fact, the nice development of reduced dimension estimation in Section 4.2.5.1 uses most of the properties presented above.

Appendix C   Operators

Θ is an operator to transform a vector in column matrix form.

When operating on a vector $\vec{v} = v_x \hat{i} + v_y \hat{j} + v_z \hat{k}$, it has the form

$$\Theta(\vec{v}) = \begin{bmatrix} v_x \\ v_y \\ v_z \end{bmatrix} \tag{C.1}$$

$\Xi()$ is an operator mapping small angles into a rotation matrix.

When operating on a set of small angles $(\varepsilon_1, \varepsilon_2, \varepsilon_3)$, it has the form

$$\Xi(\varepsilon_1, \varepsilon_2, \varepsilon_3) = \begin{bmatrix} 1 & \varepsilon_3 & -\varepsilon_2 \\ -\varepsilon_3 & 1 & \varepsilon_1 \\ \varepsilon_2 & -\varepsilon_1 & 1 \end{bmatrix} \tag{C.2}$$

$\Re()$ is an operator mapping the attitude quaternion to the rotation matrix.

When operating on an attitude quaternion q , it has the form

$$\Re(q) = \begin{bmatrix} 1 - 2(q_2^2 + q_3^2) & 2(q_1 q_2 + q_3 q_4) & 2(q_1 q_3 - q_2 q_4) \\ 2(q_1 q_2 - q_3 q_4) & 1 - 2(q_1^2 + q_3^2) & 2(q_3 q_2 + q_1 q_4) \\ 2(q_1 q_3 + q_2 q_4) & 2(q_2 q_3 - q_1 q_4) & 1 - 2(q_2^2 + q_1^2) \end{bmatrix} \tag{C.3}$$

$\bar{\Re}()$ is an operator mapping the rotation matrix to the attitude quaternion.

It is an inverse operator of $\Re()$. If $\Re(q) = M$, then it has the form $q = \bar{\Re}(M)$.

$\Pi()$ is an anti-symmetric matrix operator.

When operating on a vector $v = [v_x, v_y, v_z]^T$, it has the form

$$\Pi(v) = \begin{bmatrix} 0 & -v_z & v_y \\ v_z & 0 & -v_x \\ -v_y & v_x & 0 \end{bmatrix} \tag{C.4}$$

$\Pi'()$ is a operator similar to $\Pi()$.

When operating on a vector $v = [v_x, v_y, v_z]^T$, it has the form

$$\Pi'(v) = \begin{bmatrix} 0 & v_y & v_z \\ v_z & -v_x & 0 \\ -v_y & 0 & -v_x \end{bmatrix} \tag{C.5}$$

$\otimes$ is an operator mapping two quaternions into one equivalent quaternion.

When operating on quaternions q'', q', it yields a new quaternion q such that

$$q = q'' \otimes q' \tag{C.6}$$

which has the same meaning as

$$\Re(q) = \Re(q'') \cdot \Re(q') \tag{C.7}$$

$\aleph()$ is an operator mapping quaternion into a four by four matrix.

When operating on an attitude quaternion q'', it has the form

$$\aleph(q'') = \begin{bmatrix} q_4'' & q_3'' & -q_2'' & q_1'' \\ -q_3'' & q_4'' & q_1'' & q_2'' \\ q_2'' & -q_1'' & q_4'' & q_3'' \\ -q_1'' & -q_2'' & -q_3'' & q_4'' \end{bmatrix} \tag{C.8}$$

$CRN'()$ is a first order CRN digital filtering differential operator .

When operating on a set of data x, it has the form

$$\dot{x} = CRN'(x) \qquad\qquad (C.9)$$

$CRN''()$ is a second order CRN digital filtering differential operator .

When operating on a set of data x, it has the form

$$\ddot{x} = CRN''(x) \qquad\qquad (C.10)$$

Abbreviations

ACC	Accelerometer
AMA	Analytic Mechanics Associates
AOCS	Attitude and Orbit Control System
ASCFEST	Accelerometer and Star camera data Combined Full-dimensioned ESTimation
ASCREST	Accelerometer and Star camera data Combined Reduced-dimensioned ESTimation
ASSEST	Accelerometer and Star camera data Separate ESTimation
BD	Boresight Direction
CCD	Charged-Coupled-Device
CHAMP	CHAllenging Micro-satellite Payload
COM	Center Of Mass
CG	Center of Gravity
DFT	Discrete Fourier Transform
DLR	Deutsches Zentrum Fur Luft und Raumfahrt
DPU	Data Processing Unit
DSS	Dornier Satellitensysteme
DTM	Drag Temperature Model
EOS	Earth Observation System
ERP	Earth Radiation Pressure
ESA	European Space Agency
ESE	Earth Science Enterprise
ESSP	Earth System Science Pathfinder
FDE	Full Dimension Estimation
FIR	Finite Impulse Response

FOV	Filed Of View
GFZ	GeoForschungsZentrum
GPS	Global Positioning System
GRACE	Gravity Recovery And Climate Experiment
GSOC	German Space Operation Center
IGRF	International Geomagnetic Field
IPU	Instrument Processing Unit
JPL	Jet Propulsion Laboratory
KBR	K-Band Ranging system
KMF	Kinematic Model Filtering
KSCFEST	KBR and Star camera data Combined Full-dimensioned ESTimation
KSSEST	KBR and Star camera data Separate ESTimation
LaRC	Langley Research Center
MAG	Magnetometer
MSODP	Multi-Satellite Orbit Determination Program
MTM	center of Mass Trim assembly Mechanism
MTQ	MagneTorQuers
NASA	National Aeronautics and Space Administration
OBDH	On Board Data Handling
ONERA	Office National d'Etudes et de Recherches Aerospatiales
PC	Phase Center
PMC	Proof Mass Center
POD	Precise Orbit Determination
PSD	Power Spectrum Density
RDE	Reduced Dimension Estimation
SCA	Star Camera
SF	Satellite Frame

SNR	Signal-to-Noise Ratio
SRP	Solar Radiation Pressure
SS/L	Space System/Loral
TRSR	Turbo-Rogue Space Receiver
USO	Ultra Stable Oscillator
UTCSR	Center for Space Research, The University of Texas at Austin

Reference

Bae, S., GLAS Spacecraft Attitude Determination using CCD Star Tracker and 3-axis Gyros, Ph.D. Dissertation, Department of Aerospace Engineering and Engineering Mechanics, The University of Texas at Austin, December 1998

Balanis, C. A., Antenna Theory Analysis and Design, John Wiley &Sons, Inc., New York, 1997

Barlier, F. et al, A Thermosperic model Based on Satellite Drag data, Aeronomica Acta, Vol. 185, 1977

Bettadpur, S. V., Class notes of Statistical Estimation Theory, The University of Texas at Austin, Spring 1998

Bettadpur, S.V., Private Communication, 1999

Bettadpur, S.V., Private Communication, 2000

Bettadpur, S. V., Private Communication, 2001

Campbell, W. H., Introduction to Geomagnetic Fields, Cambridge university press, Cambridge, 1997

Carpenter, A. S., and S. N. Carroll, Low-g Payload Placement Constraints for Space Station, NASA Conference Publication 3088, Measurement and characterization of the Acceleration Environment on board the Space Station, Proceedings of a conference held at Lake Guntersville State Lodge, Guntersville, Alabama, August 11-14, 1986

Committee on Earth Gravity from Space, et al, Satellite Gravity and the Geosphere, National Academy Press, Washington, D. C., 1997

Cully, S., Private Communication, 2002

Davis, E. et al, The GRACE Mission: Meeting the Technical Challenges, 50th International Astronautical Congress, IAF-99-B.2.05, Amsterdam, Netherlands, October 1999

European Space Agency, The Hipparcos and Tycho Catalogues, ESA Publications Division, 1997

Evans, G. E., Antenna measurement Techniques, Artech House, Inc., London, 1990

Fehlberg, E., Classical Fifth-, Sixth-, Seventh- and Eighth- Order Runge-Kutta Formula with Step Size Control, NASA TR T287, October, 1968

Fisher, H. L. et al, Attitude Determination for the Star Tracker Mission, Proceedings of the AAS/AIAA Astrodynamics Conference, AAS 89-365, 1989

GRACE Error Budgets, SuperSTAR accelerometer, ONERA, 1999

GRACE Meeting, Gravity Recovery And Climate Experiment Mission Plan Document, GRACE 327-210, February 1999

GRACE Mission Briefing, University of Texas Engineers Launch NASA Climate Study from Russia, March 2002

GRACE Team, Attitude and Orbit Control System (AOCS) Specification and Description, GRACE 327-440, Draft V. 4.0, July 1999a

GRACE Team, GRACE Center of Mass Trim Assembly Qualification Model Specification, GR-OHB-SP-002, February 1998a

GRACE Team, GRACE Design and Interface Document AOCS, GR-DSS-DID-0004, July 1999b

GRACE Team, GRACE Magnetic Torquer MT30-2-GRC, GRC-MT30-IF-01-ZA, November 1999c

GRACE Team, GRACE Magnetic Torque Rods Specification, GR-DSS-SP-2220, January 1998b

GRACE Team, GRACE Magnetometer Specification, GRACE 327-40250, June 1999d

GRACE Team, GRACE Product Specification Document, GRACE 327-720, February 2002

GRACE Team, GRACE Thruster Specification, GRACE 327-40212, December 1998c

Greenberg, M. D., Foundations of Applied Mathematics, Englewood Cliffs, New Jersey, 1978

Greenwood, D.T., Principle of Dynamics, Prentice-Hall, Inc., New Jersey, 1988

Grunwaldt, L. et al, CHAMP Mission and System Requirements Specification, CH-GFZ-SP-0001, GeoForschungsZentrum, Germany, November 1996

Hamilton, W. R., Elements of Quaternions, Chelsea Pub. Co., New York, 1969

Heiskanen, W.A., and H. Moritz, Physical geodesy, W.H Freeman and Company, London, 1967

Hughes, P. C., Spacecraft Attitude Dynamics, John Wiley &Sons, Inc., New York, 1986

Hultquist, P. F., Gravitational Torque Impulse on a Stabilized Satellite, ARS Journal, Vol. 31, pp. 1506-1509, 1961

IEEE Std. 149-1979, Test Procedures for Antennas, 1979

Jacchia, L. G., Thermospheric Temperature Density, and Composition: New Models, Smith. Astrophys. Obs. Spec. Rep., 375, 1977

Junkins, J. L., Optimal Estimation of Dynamical Systems, Sijthoff-Ncordhoff International Publishers, The Netherlands, Chapter 5, 1978

Junkins, J. L. et al, Star Pattern Recognition for Real Time Attitude Determination, Journal of the Astronautical Sciences, Vol. XXV, Nc. 3, September, 1977

Kang, Z., Private Communication, 2001

Kaula, W. M., Theory of Satellite Geodesy, Blaisdell Publishing Company, Waltham, Massachusetts, 1966

Kim, J. R., Simulation Study of a Low-Low Satellite-to-Satellite Tracking Mission, Ph.D. Dissertation, Department of Aerospace Engineering and Engineering Mechanics, The University of Texas at Austin, May 2000

Knocke, P. C. and Ries, J. C., Earth Radiation Pressure Effects on Satellites, Center for Space Research, The University of Texas at Austin, Technical Memorandum, CSR-TM-87-01, September, 1987

Kruizinga, G., Private Communication, 2003

Lee, K. F., Principles of Antenna Theory, John Wiley & Sons, Inc., New York, 1984

Lerner, G. M., Three Axis Attitude Determination, In J. R. Wertz, editor, Spacecraft Attitude Determination and Control, D. Reidel, Dordrecht, the Netherlands, 1978

Milligan, T., Modern Antenna Design, McGraw-Hill, Inc., New York, 1985

Myers, J. R. et al, SKY 2000 master star catalog, AAS-97-164, 1997

NASA Facts, The Earth System Science Pathfinder Series: The Gravity Recovery And Climate Experiment, FS-2002-1-029-GSFC, February 2002

Nidey, R. A., Gravitational Torque on a satellite of Arbitrary Shape, ARS Journal, Vol. 30, pp. 203-204, 1960

Riede, M. et al, Grace Satellite Distortion Analysis, GR-DSS-TN-0010, Jet Propulsion Laboratory, March 1999

Rieger, R. et al, Procurement Specification Amendment D&C Magnetometer Sensor, GLOB-PS-1320-41-01, May 1996

Rim, H. J., TOPEX Orbit Determination using GPS Tracking System, Ph.D. Dissertation, Department of Aerospace Engineering and Engineering Mechanics, The University of Texas at Austin, December 1992

Rimrott, F.P.J., Introductory Attitude Dynamics, Springer-Verlag, New York, 1989

Roberson, R. E., Alternate Form of a Result by Nidey, ARS Journal, Vol. 31, pp. 1292, 1961

Roberson, R. E., Gravitational Torque on a Satellite Vehicle, Journal of Franklin Institute, Vol. 265, pp. 13-22, 1958

Romans, L., A note on GRACE CG offset determination with magnetic torquers, Technical Memorandum, Jet Propulsion Laboratory, Pasadena, California, 1997

Romans, L., Example of an experiment to calibrate the GRACE K-band boresight, Technical Memorandum, Jet Propulsion Laboratory, Pasadena, California, 1998

Romans, L., Optimal Determination Quaternion from Multiple Star Camera Sensors, Technical Memorandum, Jet Propulsion Laboratory, Pasadena, California, 2003

Schelkle, M., GRACE Input for the Cold Gas Assembly, Peer Review, March 1999

Schutz, B. E., and Tapley, B. D., "Orbit Accuracy Assessment for Seasat", The Journal of the Astronautical Science, Vol. XXVII, No. 4, pp. 371-390, October-December, 1980

Shuster, M. D. et al, Three-axis Attitude Determination from Vector Observations, Journal of Guidance, Control, and Dynamics, 4(1), 1981

Stauffer, J., Creation of a Guide Star Catalog for the BASG CT-601 Star Tracker, 1999

Stevens, H. D., Private Communication, 2003

Strikwerda, T. E., and Fisher, H. L., A CCD Star Camera Used for Satellite Attitude Determination, Proceedings of Summer Computer Simulation Conference, Seattle, Washington, 1988

Tapley, B.D. et al, GRACE Mission Proposal to the ESSP Program, 1997

Tapley, B. D., Shcutz, B. E., Ries, J.C., and C.K. Shum, Precise Orbit Determination for Topex, Advanced Space Res. Vol 10, No. 3-4, pp. (3) 239-(3)247, 1990

Thomas, J.B., An Analysis of Gravity-Field Estimation Based on Inter-satellite Dual-1-Way Biased Ranging, JPL Publication 98-15, Jet Propulsion Laboratory, Pasadena, California, May 1999

Touboul, P. et al, SuperSTAR accelerometer for the Gravity Recovery And Climate Experiment Design Description Document, Technical Reports n° 27/3805 DMPH/Y, Issue 2, Physics and Instrumentation Department, ONERA, September, 2000

Vetter, J.R. et al, A Historical Survey of Earth Gravitational Models Used in Astrodynamics from Sputnik and TRANSIT to GPS and TOPEX, Proceedings of the AAS/AIAA Astrodynamics Conference, AAS 93-620, Victoria, British Columbia, Canada, August 16-19, 1993

Wahba, G., A least squares estimate of satellite attitude, SIAM Review, 8(3), July, 1996

Wang, F., Grace Accelerometer Proof Mass Determination, Center for Space Research, The University of Texas at Austin, Technical Memorandum, CSR-TM-00-01, January 2000a

Wang, F. et al, GRACE CG Offset Determination by Magnetic Torquers during the In Flight Phase, 2000 AIAA Region IV Student Paper Conference, Houston, Texas, April 2000b

Wang, F. et al, Antenna Phase Center Determination of Inter-Communicating Satellites, Proceedings of the AAS/AIAA Astrodynamics Conference, AAS-02-218, San Antonio, Texas, January 2002a

Wang, F. et al, Precise Determination of Accelerometer Proof mass, Proceedings of the AAS/AIAA Astrodynamics Conference, AAS-02-159, San Antonio, Texas, January 2002b

Wang, F. et al, The Accelerometer Proof Mass Offset Calibration of GRACE, Proceedings of the AAS/AIAA Astrodynamics Conference, AAS-01-220, California, February 2001

Wertz, J.R., Spacecraft Attitude Determination and Control, D. Reidel Publishing Company, Boston, 1978

Whittaker, E. T., A Treatise on the Analytical Dynamics of Particles and Rigid Bodies, Cambridge University Press, Cambridge, 1961

Vita

Furun Wang was born in Shuozhou, Shanxi Province, P.R. China on November 7, 1973, the youngest son of Yaoshan Wang and Fang Lu. After receiving the degree of Bachelor of Science from Harbin Institute of Technology, P.R. China, in 1994, by completing his study at the Department of Aerospace Engineering, he entered the Beijing Institute of Control Engineering, a prominent research institute of the China Aerospace Corporation. He received the degree of Master of Science, in May 1997. In the same year he entered the Graduate School of the University of Texas at Austin and joined the Center for Space Research, where he works presently.

Permanent address: 2501 Lake Austin Blvd., #F107, Austin, Texas 78703
This dissertation was typed by the author.